UNIVERSITÀ DEGLI STUDI DI PADOVA

Dipartimento di Fisica e Astronomia "Galileo Galilei"

Master Degree in Physics

Final Dissertation

Pearling Instability in Mass-Conserving Pattern-Forming Systems: from Reaction-Diffusion to Active-Matter Models

Thesis supervisor
Prof. Gianmaria Falasco
Thesis co-supervisors
Prof. Erwin Frey
Dr. Davide Toffenetti
Dr. Beatrice Nettuno

Candidate
Giorgio Benvegnù

Academic Year 2025/2026

Abstract

The Min system is a protein complex involved in cell division in Escherichia coli. Its dynamics arise from the interplay between biochemical reactions and diffusion, which can drive the system out of its homogeneous state and lead to self-organized pattern formation via a diffusion-driven instability mechanism. While in vivo the Min proteins typically exhibit pole-to-pole oscillations that ensure symmetric cell division, in vitro reconstituted systems display a rich variety of stationary patterns, including stripes, dots, and foam-like structures.

These patterns have been successfully and quantitatively reproduced using theoretical models based on reaction-diffusion equations. We study a minimal three-component mass-conserving reaction-diffusion model inspired by the Min system. The model consists of an inactive cytosolic species corresponding to MinD-ADP, an active cytosolic species corresponding to MinD-ATP, and a membrane-bound density representing all membrane associated protein, including both bound MinD and transient MinD-MinE complex involved in detachment. The dynamics conserve total mass and incorporate nucleotide exchange together with membrane attachment and detachment processes.

The resulting phase diagram, controlled by the total protein mass and the nucleotide exchange rate, reproduces the stationary patterns observed in vitro. In particular, variations of the total mass can induce a transition from stripe-like to dot-like structures.

The main goal of the project is to characterize the stability of localized stripe solutions and to understand the pearling instability, through which an extended stripe becomes unstable and breaks up into a sequence of aligned dots. This mechanism provides insight into the selection and robustness of localized patterns in mass-conserving reaction-diffusion systems.

Finally, we discuss how the theoretical framework developed can be extended to other pattern-forming systems with conserved dynamics exhibiting localized structures, in particular Active Model B^-.

Contents

Chapter 1

Introduction and motivations

The spontaneous formation of spatiotemporal patterns is one of the most fascinating phenomena in the physics of biological systems and plays a central role in a wide range of cellular processes, including cell division, polarity establishment, and intracellular transport. These patterns emerge from the collective dynamics of large numbers of interacting molecules and provide cells with a robust mechanism for organizing biochemical activity in space and time. Over the past decades, advances in fluorescence microscopy and in vitro reconstitution experiments have made it possible to directly observe intracellular protein patterns, revealing that self-organization is a widespread strategy employed by living cells. Two paradigmatic examples are the Min protein system in Escherichia coli and the Cdc42 GTPase polarity system in budding yeast (S. cerevisiae).

Cell division in E. coli requires a mechanism that reliably positions the Z-ring, formed by the protein FtsZ, at midcell. This task is achieved through one of the most striking examples of intracellular pattern formation: the pole-to-pole oscillations of Min proteins [7, 10].
The core components of the protein complex, MinD and MinE, continuously cycle between membrane-bound and cytosolic states through an ATP-driven reaction network (Fig. 1.1). Cytosolic MinD-ADP is first converted into its active ATP-bound form through nucleotide exchange. Activated MinD-ATP can then bind to the cell membrane, where it recruits additional MinD molecules. Membrane-bound MinD forms a complex with MinC, namely MinCD, that inhibits Z-ring assembly; since MinC does not itself take part in the ATP-driven redistribution but merely follows the MinD pattern, it is not included explicitly in the reaction network shown below. Membrane-bound MinD further recruits the ATPase-activating protein MinE. The resulting MinDE complex stimulates ATP hydrolysis, causing MinD to detach from the membrane as inactive MinD-ADP while MinE is simultaneously released back into the cytosol. The continuous consumption of ATP maintains the system far from thermodynamic equilibrium and sustains this cyclic redistribution of proteins between the membrane and the cytosol.

The coupling between these local biochemical reactions and protein diffusion both on the cell membrane and in the cytosol gives rise to robust pole-to-pole oscillations of the membrane-bound Min proteins. As a consequence, the time-averaged concentration of MinCD complexes is lowest at the cell center, providing a positional cue that allows the Z-ring to assemble precisely at midcell and ensuring symmetric cell division.

Remarkably, these dynamics have been reconstituted in vitro on supported lipid bi-layers [9], subsequently revealing a rich variety of patterns, including dynamic pattens (e.g. traveling waves and spiral waves) and stationary ones (such as dots, stripes, and foam-like structures) [5].

A conceptually similar mechanism operates in the Cdc42 GTPase system, a Rho-family GTPase responsible for polarity establishment in budding yeast. Unlike rod-shaped E. coli, budding yeast cells are approximately spherical and divide asymmetrically by growing a daughter cell from a localized bud. This process requires the formation of a highly localized polarity site, which is achieved through the self-organized accumulation of the Cdc42 into a single membrane cluster [8].
Like all GTPases, Cdc42 switches between an active GTP-bound state and an inactive GDP-bound

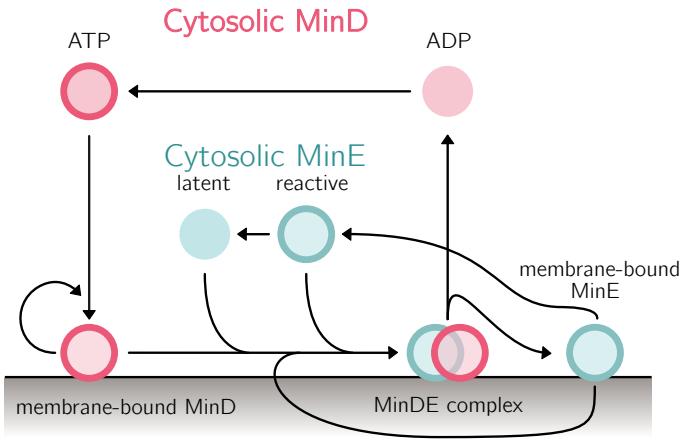

Figure 1.1: Reaction network underlying the Min protein oscillations in E. coli. Cytosolic MinD-ADP is activated by nucleotide exchange to MinD-ATP, which can bind to the membrane. Membrane-bound MinD recruits additional MinD molecules together with the ATPase-activating protein MinE, forming MinD–MinE complexes. MinE stimulates ATP hydrolysis, causing MinD-ADP and MinE to detach into the cytosol, thereby completing the ATP-driven cycle. The interplay between this reaction network and protein diffusion gives rise to the characteristic pole-to-pole oscillations in vivo cell and a rich variety of patterns in vitro experiments.
This detailed biochemical network serves as the biological reference for the coarse-grained models introduced in the following chapters.

state, with both forms able to associate with the membrane, although Cdc42-GTP has a higher membrane affinity (Fig. 1.2). Inactive Cdc42-GDP is preferentially extracted from the membrane into the cytosol by its guanine nucleotide dissociation inhibitor (GDI), whereas membrane-bound Cdc42-GTP promotes its own recruitment and activation through a positive feedback loop. Switching between the two nucleotide-bound states is catalyzed by two classes of regulatory proteins: guanine nucleotide exchange factors (GEFs), which activate Cdc42 by replacing GDP with GTP, and GTPase-activating proteins (GAPs), which stimulate the intrinsic GTP hydrolysis activity of Cdc42, restoring the inactive GDP-bound state. Budding yeast Cdc42 has a single known GEF, Cdc24, and several GAPs.
The interplay between membrane attachment and detachment, Cdc42 activation and inactivation, positive feedback, and diffusion can therefore lead to spontaneous symmetry breaking and the formation of a stable, localized cluster of active Cdc42 on the membrane, defining the site where the daughter bud will emerge.

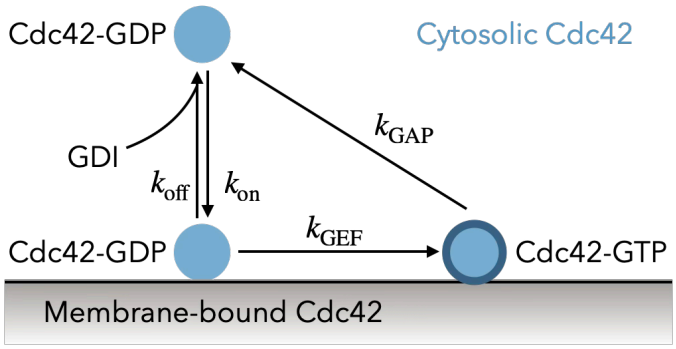

Figure 1.2: Simplified reaction network of the Cdc42 GTPase polarity system in budding yeast. Inactive Cdc42-GDP can reversibly bind to the membrane, where it is converted into the active Cdc42-GTP state through GEF-mediated activation, reinforced by a positive feedback. Active Rho-GTP exhibits a stronger membrane affinity, whereas GTP hydrolysis converts it into Cdc42-GDP, which preferentially detaches into the cytosol: the combined process of inactivation and detachment is represented by the effective rate k_{GAP}. Together with diffusion, these reactions can lead to spontaneous symmetry breaking and the formation of a localized cluster of active Cdc42 at the membrane, defining the budding site. Coupled with diffusion, these reactions generate a stable localized cluster of active Cdc42 proteins on the membrane, defining the budding site.

The examples above differ in molecular detail and biological function, but they share a number of fundamental features that are central from a physics perspective.
First, in both systems the functionally relevant pattern is encoded in the spatial distribution of membrane-bound proteins. In other words, an important and widely realized class of intracellular patterns are membrane-bound patterns, in which cellular function is determined by the organization of proteins on the membrane.
Second, the key unifying feature of the biochemical interaction networks is conformational switching between different protein states, each characterized by distinct interaction properties and membrane affinities. Protein conformations (or states) change as a consequence of local biochemical reactions with other bio-molecules (lipids, nucleotides, or other proteins).
Finally, spatial transport and redistribution of proteins occurs through diffusion in the cytosol and along the membrane. In general, in the absence of active transport, molecular diffusion is the only available transport mechanism. Although the transport mechanism is identical in both compartments, diffusion is typically much faster in the cytosol than on the membrane, such that $D_c \gg D_m$.

A further important property of these systems is the conservation of protein mass. Protein synthesis and degradation typically occur on timescales much longer than those associated with intracellular pattern formation. Consequently, the total copy number of each protein species can be regarded as conserved, and proteins are neither created nor destroyed during the dynamics but merely redistributed among different biochemical states and cellular compartments.

The interplay between local biochemical reactions, diffusive transport, and mass conservation can destabilize an initially homogeneous protein distribution, leading to spontaneous pattern formation through a diffusion-driven instability mechanism. While conceptually related to the classical models introduced by Alan Turing [15], intracellular protein patterns differ fundamentally because the reacting species are globally conserved. This additional conservation law profoundly modifies both the linear instability and the nonlinear dynamics, giving rise to new classes of instabilities and patterns.

These common features are naturally captured by mass-conserving reaction–diffusion (McRD) systems [4]. This framework describes protein dynamics by coupling spatial redistribution via diffusion with local reactions, under the constraint of mass conservation. At the continuum level, the spatiotemporal dynamics is governed by

$$\begin{cases} \partial_t \mathbf{m}(\boldsymbol{\sigma}, t) = -\nabla_{\mathbb{S}} \cdot \mathbf{J}_{\mathrm{mem}} + \mathbf{R}_{\mathrm{mem}}(\mathbf{m}, \mathbf{c}|_{\mathbb{S}}) \\ \partial_t \mathbf{c}(\mathbf{x}, t) = -\nabla \cdot \mathbf{J}_{\mathrm{cyt}} + \mathbf{R}_{\mathrm{cyt}}(\mathbf{c}) \end{cases}, \tag{1.1}$$

where $\mathbf{c}(\mathbf{x}, t)$ and $\mathbf{m}(\boldsymbol{\sigma}, t)$ are a vectors of protein densities defined respectively in the three-dimensional cytosolic volume and in the two-dimensional membrane surface; $\mathbf{J}_{\mathrm{mem}} = -D_m \nabla_{\mathbb{S}} \mathbf{m}$ and $\mathbf{J}_{\mathrm{cyt}} = -D_c \nabla \mathbf{c}$ denote the membrane and cytosolic fluxes; $\mathbf{R}_{\mathrm{mem}}(\mathbf{m}, \mathbf{c}|_{\mathbb{S}})$ and $\mathbf{R}_{\mathrm{cyt}}(\mathbf{c})$ are the local biochemical reactions respectively on the membrane and in the cytosol. At the interface, we have to impose reactive boundary conditions to guarantee local mass conservation by equating the net reactive flux of proteins between membrane and cytosol to the diffusive flux of the respective cytosolic species normal to the membrane, meaning

$$-D_c \left[\nabla_{\perp} \mathbf{c}\right]_{\mathbb{S}} = \mathbf{R}_{\mathrm{bound}}(\mathbf{m}, \mathbf{c}|_{\mathbb{S}}). \tag{1.2}$$

The reaction term $\mathbf{R}_{\mathrm{bound}}(\mathbf{m}, \mathbf{c}|_{\mathbb{S}})$ contains all the attachment and detachment reactions included in $\mathbf{R}_{\mathrm{mem}}(\mathbf{m}, \mathbf{c}|_{\mathbb{S}})$, but $\mathbf{R}_{\mathrm{mem}}(\mathbf{m}, \mathbf{c}|_{\mathbb{S}})$ additionally contains reactions solely involving membrane-bound components.
Equations 1.1 and 1.2 provide a generic description of intracellular protein dynamics that is largely independent of the specific molecular details of a particular biological system.

While reaction–diffusion models have successfully and quantitatively reproduced the patterns observed experimentally [1, 6, 11, 17, 18], a comprehensive theoretical understanding of the transitions between different pattern types is still lacking. The complexity of realistic biochemical networks, involving many interacting molecular species and nonlinear feedback loops, makes analytical progress extremely challenging.

For this reason, productive strategy is the reduction of biological complexity to minimal, tractable subsystems both experimentally and theoretically. In particular on the theoretical side, it is useful to introduce minimal coarse-grained models that retain the essential physical ingredients responsible for self-organization while remaining analytically tractable.

Since nontrivial mass-conserving dynamics require at least two states, the simplest possible McDR model consists of a two-component model with a single protein cycling between two possible states, i.e membrane-bound and cytosolic state. Two-component McRD models have been studied extensively and successfully capture many generic properties of intracellular protein patterns. However, their long-time dynamics are typically characterized by coarsening without boundaries, analogous to phase separation in standard Cahn-Hilliard (Model B) flows [16].

There are several ways to overcome this limitation and allow finite wavelength pattern: two prominent mechanisms are, for example, weakly breaking mass-conservation or the addition of a third component to the model. In this thesis, we pursue the latter approach and investigate a minimal three-component McRD model.

Chapter 2

Three-component McRD model

Our three-component model is a minimal coarse-grained version of the Min protein system introduced in Fig. 1.1. Rather than resolving every molecular species involved in the biochemical network, the model retains only the essential protein states required for intracellular pattern formation. Each dynamical variable therefore represents a coarse-grained protein density. In particular, the inactive cytosolic component c_i represents proteins in the cytosol that are not able to bind with the membrane, thus there is a one-to-one correspondence between c_i and MinD-ADP. The active cytosolic component c_a is the local density of cytosolic state proteins that are allowed to bind, i.e. MinD-ATP in the real model. Finally, the membrane component m is a course-grained variable and represents the local total density of membrane-bound proteins, without distinguishing between membrane-bound MinD-ATP and the transient MinD-MinE complex responsible for MinD detachment.

The coarse-grained model retains only three elementary processes: nucleotide exchange, membrane attachment, and membrane detachment. The first is an ATP-driven, non-equilibrium reaction through which inactive cytosolic proteins become activated with rate λ. Whereas attachment and detachment, respectively with rates $\gamma(m)$ and $\alpha(m)$, are treated as undriven chemical reactions with negligible backward rates. The resulting reaction scheme is illustrated in Fig. 2.1.

The model therefore preserves the physical ingredients identified in the introduction, meaning membrane attachment and detachment, conformational switching, diffusion, and mass conservation, while discarding molecular details that are not expected to affect the generic pattern-forming mechanisms.

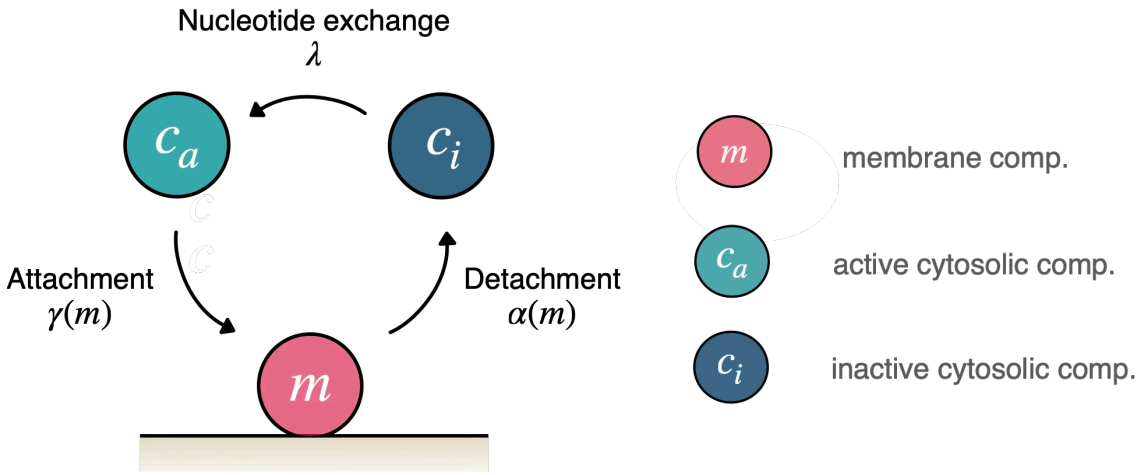

Figure 2.1: Reaction network of the coarse-grained three-component McRD. The model consists of an inactive cytosolic species corresponding to MinD–ADP, an active cytosolic species corresponding to MinD–ATP, and a membrane-bound density representing all membrane-associated protein, including both bound MinD and transient MinD–MinE complex involved in detachment. Reaction terms conserve total mass and incorporate non-equilibrium nucleotide exchange and undriven attachment and detachment processes.

Since the objective of this work is to investigate the fundamental mechanisms of pattern formation rather than the effects of cellular geometry, we consider all three species to evolve in a simple two-dimensional rectangular domain with no-flux boundary conditions. This setup closely resembles in vitro reconstituted experiments, in which a supported lipid membrane is coupled to a very thin cytosolic layer.

2.1 Model

The dynamics of the system is governed by the following system of reaction-diffusion equations

$$\begin{cases} \partial_t m = D_m \nabla^2 m + R_1(m, c_a, c_i) \\ \partial_t c_a = D_c \nabla^2 c_a + R_2(m, c_a, c_i) \\ \partial_t c_i = D_c \nabla^2 c_i + R_3(m, c_a, c_i) \end{cases}, \tag{2.1}$$

with $m = m(\mathbf{x}, t)$, $c_a = c_a(\mathbf{x}, t)$, $c_i = c_i(\mathbf{x}, t)$, and the physical constraint $D_c \gg D_m$.

Since all three species are defined on the same spatial domain, the reactive boundary conditions introduced in the general framework in Eq. (1.2) reduce to the requirement of local mass conservation. Consequently, the reaction terms satisfy

$$R_3(m, c_a, c_i) = -R_1(m, c_a, c_i) - R_2(m, c_a, c_i). \tag{2.2}$$

Combining notation of Eq. (2.1) and the three elementary reactions, we get

$$\begin{aligned} R_1(m, c_a, c_i) &= \gamma(m) c_a - \alpha(m), \\ R_2(m, c_a, c_i) &= \lambda c_i - \gamma(m) c_a. \end{aligned} \tag{2.3}$$

Here, R_1 denotes the net production of membrane-bound molecules and consists of a gain term (attachment) proportional to $\gamma(m)$ together with a loss term (detachment) proportional to $\alpha(m)$. Similarly, R_2 describes the net production of active cytosolic molecules through nucleotide exchange at rate λ and their depletion through membrane attachment $\gamma(m)$. The dependence of the attachment rate γ on the membrane density m accounts for the positive-feedback mechanism observed in the real biological system.

It is useful to note that, in the fast-reactivation limit ($\lambda \to \infty$), inactive proteins are instantaneously converted into the active state, such that c_i vanishes and the model reduces to an effective two-component McRD system.

Throughout this thesis we focus on the simplest reaction network capable of reproducing the essential features of intracellular protein pattern formation. Specifically, nucleotide exchange and membrane detachment are assumed to occur spontaneously, whereas membrane attachment consists of a spontaneous contribution supplemented by a cooperative feedback mechanism. This choice introduces a single nonlinear reaction term that captures the experimentally observed self-recruitment of Min proteins while keeping the model analytically tractable. The corresponding molecular reactions are:

- Spontaneous nucleotide exchange

$$C_i \xrightarrow{\lambda} C_a, \tag{2.4}$$

- Spontaneous detachment

$$M \xrightarrow{\alpha_0} C_i, \tag{2.5}$$

- Spontaneous attachment plus feedback mechanism

$$C_a \xrightarrow{\gamma_1} M, \quad C_a + 2M \xrightarrow{\gamma_2} 3M, \tag{2.6}$$

where the capital letters denote the chemical species corresponding to the density fields represented by the lowercase variables.
Under the law of mass action, these reactions correspond to

$$\begin{aligned} R_1(m, c_a, c_i) &= \left(\gamma_1 + \gamma_2 m^2(\mathbf{x}, t)\right) c_a(\mathbf{x}, t) - \alpha_0 m(\mathbf{x}, t), \\ R_2(m, c_a, c_i) &= \lambda c_i(\mathbf{x}, t) - \left(\gamma_1 + \gamma_2 m^2(\mathbf{x}, t)\right) c_a(\mathbf{x}, t). \end{aligned} \tag{2.7}$$

Comparing the mass-action kinetics with the generic notation introduced earlier, immediately yields

$$\gamma(m) = \gamma_1 + \gamma_2\, m^2, \quad \alpha(m) = \alpha_0\, m. \tag{2.8}$$

2.2 Change of variables

While the variables (m, c_a, c_i) directly describe the biochemical state of the system, they are not the most convenient choice for understanding the underlying transport mechanisms. It is therefore useful to reformulate the dynamics in terms of variables that explicitly separate the conserved degree of freedom from the reactive ones.

To this end, we introduce the total local mass density

$$\rho(\mathbf{x}, t) \equiv m(\mathbf{x}, t) + c_a(\mathbf{x}, t) + c_i(\mathbf{x}, t), \tag{2.9}$$

and the local mass redistribution potential

$$\eta(\mathbf{x}, t) \equiv \frac{D_m}{D_c} m(\mathbf{x}, t) + c_a(\mathbf{x}, t) + c_i(\mathbf{x}, t). \tag{2.10}$$

The first variable simply represents the total concentration of protein locally present in the system, independently of its biochemical state. The second variable naturally emerges from the reaction-diffusion equations and will be shown to govern the redistribution of the conserved protein mass.

As previously mentioned, the system is by construction mass conserving because the reaction terms of the three equations sum up to zero. Consequently, the average total mass density of the system, meaning the integral of the local total mass field over the entire domain divided by the system size, $\bar{\rho} = \frac{1}{\mathcal{V}} \int_{\mathcal{V}} d\mathbf{x} \rho(\mathbf{x}, t)$, must remain constant throughout the dynamics.

This property can be verified explicitly by differentiating the definition of the average density with respect to time,

$$\begin{aligned} \frac{d}{dt}\bar{\rho} &= \frac{1}{\mathcal{V}} \frac{d}{dt} \int_{\mathcal{V}} d\mathbf{x}\ \left[m(\mathbf{x}, t) + c_a(\mathbf{x}, t) + c_i(\mathbf{x}, t)\right] \\ &= \frac{1}{\mathcal{V}} \int_{\mathcal{V}} d\mathbf{x}\ \left[\partial_t m(\mathbf{x}, t) + \partial_t c_a(\mathbf{x}, t) + \partial_t c_i(\mathbf{x}, t)\right] \\ &\overset{(2.1)}{=} \frac{1}{\mathcal{V}} \int_{\mathcal{V}} d\mathbf{x}\ \left[D_m \nabla^2 m + \cancel{R_1} + D_c \nabla^2 c_a + \cancel{R_2} + D_c \nabla^2 c_i - \cancel{(R_1 + R_2)}\right] = 0, \end{aligned} \tag{2.11}$$

where in the last step we apply divergence theorem together with no-flux boundary conditions, i.e.

$$\partial_{\mathbf{n}} m\big|_{\partial\Omega} = 0, \quad \partial_{\mathbf{n}} c_i\big|_{\partial\Omega} = 0, \quad \partial_{\mathbf{n}} c_a\big|_{\partial\Omega} = 0, \tag{2.12}$$

with $\mathbf{n}$ the unit vector normal to the border of the system $\partial\Omega$.
The same result is obtained for periodic boundary conditions. Therefore, proteins are neither created nor destroyed during the dynamics, but are continuously redistributed between different biochemical states and spatial locations.

Using the new variables ρ and η, the reaction-diffusion equations can be rewritten as

$$\begin{cases} \partial_t \rho = D_c \nabla^2 \eta \\ \partial_t \eta = (D_c + D_m)\nabla^2 \eta - D_m \nabla^2 \rho - R(\rho, \eta, c_i)\ , \\ \partial_t c_i = D_c \nabla^2 c_i - R_1(\rho, \eta, c_i) - R_2(\rho, \eta, c_i) \end{cases} \tag{2.13}$$

where

$$R(\rho, \eta, c_i) \equiv \left(1 - \frac{D_m}{D_c}\right) R_1(\rho, \eta, c_i). \tag{2.14}$$

Strictly speaking, all reaction terms should be written as $R(\rho, \eta, c_i) = R\left(m(\rho, \eta, c_i), c_a(\rho, \eta, c_i), c_i\right)$ since the original variables are now expressed as functions of (ρ, η, c_i). For simplicity, however, this dependence will be left implicit throughout the remainder of the thesis.

Note that in general R could be written as a combination of R_1 and R_2; however, when the diffusion coefficients of the two cytosolic species are equal, R is simply proportional to R_1. Furthermore, since $D_m/D_c \ll 1$, we can physically interpret $R(\mathbf{x})$ as the net number of proteins that attach to the membrane in a specific position per unit of time.

The evolution equations of ρ and η in Eq. (2.13) follow directly from their definitions. Summing the three reaction–diffusion equations of Eq. (2.1) immediately gives

$$\begin{aligned}
\partial_t \rho &\overset{(2.9)}{=} \partial_t m + \partial_t c_a + \partial_t c_i \\
&\overset{(2.1)}{=} D_m \nabla^2 m + \cancel{R_1} + D_c \nabla^2 c_a + \cancel{R_2} + D_c \nabla^2 c_i - \cancel{(R_1 + R_2)} \\
&= D_c \nabla^2 \underbrace{\left(\frac{D_m}{D_c} m + c_a + c_i\right)}_{\eta} \\
&\overset{(2.10)}{=} D_c \nabla^2 \eta.
\end{aligned} \tag{2.15}$$

Similarly,

$$\begin{aligned}
\partial_t \eta &\overset{(2.10)}{=} \frac{D_m}{D_c} \partial_t m + \partial_t c_a + \partial_t c_i \\
&\overset{(2.1)}{=} \frac{D_m^2}{D_c} \nabla^2 m + \frac{D_m}{D_c} R_1 + D_c \nabla^2 c_a + R_2 + D_c \nabla^2 c_i - R_1 - R_2 \\
&= D_c \underbrace{\left(\frac{D_m}{D_c} \nabla^2 m + \nabla^2 c_a + \nabla^2 c_i\right)}_{\nabla^2 \eta} + D_m \underbrace{\left(\frac{D_m}{D_c} \nabla^2 m + \nabla^2 c_a + \nabla^2 c_i\right)}_{\nabla^2 \eta} - \\
&\quad - D_m \underbrace{\left(\nabla^2 m + \nabla^2 c_a + \nabla^2 c_i\right)}_{\nabla^2 \rho} - \underbrace{\left(1 - \frac{D_m}{D_c}\right) R_1}_{R} \\
&\overset{\substack{(2.9)\\(2.10)\\(2.14)}}{=} (D_c + D_m) \nabla^2 \eta - D_m \nabla^2 \rho - R.
\end{aligned} \tag{2.16}$$

Finally, the equation for the inactive cytosolic component remains unchanged apart from expressing the reaction terms in the new variables.

Equation (2.13) shows that the conserved field ρ evolves according to a continuity equation as a standard Model B dynamics:

$$\partial_t \rho = -\nabla \cdot \mathbf{J}_\rho, \quad \text{with } \mathbf{J}_\rho = -D_c \nabla \eta. \tag{2.17}$$

The variable η therefore acts as the driving force for mass redistribution: spatial gradients of η generate protein fluxes that redistribute the conserved mass throughout the system. In this sense, η plays a role analogous to a chemical potential in equilibrium thermodynamics. However, η should not be interpreted as a true thermodynamic potential, as it is not obtained as the functional derivative of a free-energy functional with respect to the conserved density. Instead, η is itself a dynamical field whose evolution is coupled to the reaction kinetics.

In contrast to the conserved mass field, the redistribution potential η is not conserved. Its evolution is governed by the interplay between diffusion, spatial variations of the total mass, and the local reaction term R. Since membrane attachment transfers proteins from the rapidly diffusing cytosolic to the slowly diffusing membrane-bound state, it tends to decrease the local value of η. Conversely, net detachment increases the concentration in the cytosol and tends to increase η.
This interpretation can also be understood directly from the evolution equation of η in Eq. (2.13). When the characteristic length scale of the system is sufficiently large, the Laplacian terms vary smoothly in space and mainly act to redistribute the perturbations generated by the reactions. In this limit, the reaction term provides the dominant local contribution to the dynamics of η: regions where $R > 0$ (net membrane attachment) tend to experience a decrease of the redistribution potential, while regions where $R < 0$ (net membrane detachment) tend to exhibit an increase of η.

At steady state, the absence of net mass transport requires the redistribution flux to vanish, i.e.

$$\nabla\eta^{\mathrm{sta}} = 0 \quad \Longrightarrow \quad \eta^{\mathrm{sta}}(\mathbf{x}) = \eta_0, \tag{2.18}$$

and consequently the total local mass profiles is determined by the following constraint

$$D_m\nabla^2\rho^{\mathrm{sta}} = -R(\rho^{\mathrm{sta}}, \eta^{\mathrm{sta}}, c_i^{\mathrm{sta}}). \tag{2.19}$$

This property can also be derived directly from the stationary equations. First, we impose all the time derivatives in Eq. (2.13) equal to zero,

$$\begin{cases} 0 = D_c\nabla^2\eta^{\mathrm{sta}} \\ 0 = (D_c + D_m)\nabla^2\eta^{\mathrm{sta}} - D_m\nabla^2\rho^{\mathrm{sta}} - R(\rho^{\mathrm{sta}}, \eta^{\mathrm{sta}}, c_i^{\mathrm{sta}}) \\ 0 = D_c\nabla^2 c_i^{\mathrm{sta}} - R_1(\rho^{\mathrm{sta}}, \eta^{\mathrm{sta}}, c_i^{\mathrm{sta}}) - R_2(\rho^{\mathrm{sta}}, \eta^{\mathrm{sta}}, c_i^{\mathrm{sta}}) \end{cases}. \tag{2.20}$$

Multiplying the first equation by η^{sta} and integrating over the domain using no-flux BCs, one gets

$$\begin{aligned} 0 &= \int_\Omega dV\ \eta^{\mathrm{sta}}\nabla^2\eta^{\mathrm{sta}} \\ &= \int_\Omega dV\ \nabla\cdot(\eta^{\mathrm{sta}}\nabla\eta^{\mathrm{sta}}) - \int_\Omega dV\ |\nabla\eta^{\mathrm{sta}}|^2 \\ &= \cancel{\oint_{\partial\Omega} dS\ (\eta^{\mathrm{sta}}\nabla\eta^{\mathrm{sta}})\cdot\mathbf{n}} - \int_\Omega dV\ |\nabla\eta^{\mathrm{sta}}|^2 \\ &= -\int_\Omega dV\ |\nabla\eta^{\mathrm{sta}}|^2. \end{aligned} \tag{2.21}$$

Since the integrand is non-negative everywhere, the integral can vanish only if $\nabla\eta^{\mathrm{sta}} = 0$ and consequently $\eta^{\mathrm{sta}}(\mathbf{x}) = \eta_0$, where η_0 is a constant.
Substituting this result into the stationary equation for η, immediately yields to Eq. (2.19).

The condition of constant redistribution potential has a simple physical interpretation: a stationary state requires the mass flux to vanish everywhere, i.e.

$$0 = \mathbf{J}_\rho = -D_c\nabla\eta^{\mathrm{sta}} = -D_m\nabla m^{\mathrm{sta}} - D_c\nabla c_a^{\mathrm{sta}} - D_c\nabla c_i^{\mathrm{sta}}. \tag{2.22}$$

Therefore, the stationary cytosolic mass flux $\mathbf{J}^{\mathrm{sta}}_{\rho,\mathrm{cyt}} = -D_c\nabla c_a^{\mathrm{sta}} - D_c\nabla c_i^{\mathrm{sta}}$ is equal in modulus and has opposite direction of the stationary membrane mass flux $\mathbf{J}^{\mathrm{sta}}_{\rho,\mathrm{mem}} = -D_m\nabla m^{\mathrm{sta}}$, showing that proteins continue to exchange between membrane and cytosol while the total protein mass remains locally balanced.

2.3 LSA and phase diagram

In Turing-like systems, the analysis typically begins with a linear stability analysis (LSA) around a homogeneous steady state to determine whether a spatially homogeneous steady state is stable against small perturbations. Since the analysis is performed around a spatially uniform equilibrium, it is often referred to as a zero-dimensional analysis.

Throughout the remainder of this work, we consider the average total mass $\bar{\rho}$ (which is directly related to the total protein mass of the system $M_{\text{tot}} = \bar{\rho}\,\mathcal{V}$) and the nucleotide exchange rate λ as the control parameters, while all other parameters are kept fixed. In the non-dimensional formulation, we choose

$$D_c = 100, \quad D_m = 1, \quad \gamma_1 = 1, \quad \gamma_2 = 1, \quad \alpha_0 = 1. \tag{2.23}$$

This choice is motivated by the underlying biological system. The diffusion coefficients are mainly determined by the physical properties of the cytosol and the membrane and satisfy the experimentally observed separation of time scales such that the diffusion in the cytosol is much faster than the one in the membrane ($D_c \gg D_m$).
The attachment and detachment rates are intrinsic biochemical properties of the proteins and are therefore assumed to remain fixed. In contrast, both the total protein concentration and the nucleotide rate can be controlled in vitro experiments simply by adding or removing proteins and nucleotides from the system, making $\bar{\rho}$ and λ the most natural experimentally accessible control parameters.

The homogeneous stationary state is obtained by solving the reaction kinetics in the absence of spatial gradients,

$$\begin{cases} 0 = R_1(m^*, c_a^*, c_i^*) \\ 0 = R_2(m^*, c_a^*, c_i^*) \end{cases}. \tag{2.24}$$

Note that only two equations are required, since the third condition follows from total mass conservation, i.e. $\bar{\rho} = m^* + c_a^* + c_i^*$.

To investigate its stability, we introduce small perturbations around the homogeneous state,

$$\delta\mathbf{u}(\mathbf{x}, t) = [m(\mathbf{x}, t) - m^*,\, c_a(\mathbf{x}, t) - c_a^*,\, c_i(\mathbf{x}, t) - c_i^*]^T. \tag{2.25}$$

and retain only terms linear in the perturbation amplitudes. Passing to Fourier space, each wave mode evolves independently according to

$$\partial_t \delta\tilde{\mathbf{u}} = J_q\, \delta\tilde{\mathbf{u}}, \tag{2.26}$$

where J_q is the Jacobian of the reaction-diffusion system evaluated at the homogeneous steady state, which depends on the Fourier mode q. Explicitly,

$$J_q = \begin{pmatrix} \frac{\partial R_1}{\partial m}\big|_{m^*, c_a^*, c_i^*} - D_m q^2 & \frac{\partial R_1}{\partial c_a}\big|_{m^*, c_a^*, c_i^*} & \frac{\partial R_1}{\partial c_i}\big|_{m^*, c_a^*, c_i^*} \\ \frac{\partial R_2}{\partial m}\big|_{m^*, c_a^*, c_i^*} & \frac{\partial R_2}{\partial c_a}\big|_{m^*, c_a^*, c_i^*} - D_c q^2 & \frac{\partial R_2}{\partial c_i}\big|_{m^*, c_a^*, c_i^*} \\ -\frac{\partial R_1 + R_2}{\partial m}\big|_{m^*, c_a^*, c_i^*} & -\frac{\partial R_1 + R_2}{\partial c_a}\big|_{m^*, c_a^*, c_i^*} & -\frac{\partial R_1 + R_2}{\partial c_i}\big|_{m^*, c_a^*, c_i^*} - D_c q^2 \end{pmatrix}. \tag{2.27}$$

The growth rates of infinitesimal perturbations are obtained by diagonalizing J_q. This yields three dispersion relations $\sigma_i(q)$, whose real parts determine whether perturbations with wavenumber q grow or decay. A non-zero imaginary part, on the other hand, is associated with oscillatory dynamics.

Depending on the values of $\bar{\rho}$ and λ, three qualitatively different behaviors are observed:

- Stable regime: All eigenvalues have negative real parts for all wavenumbers. Consequently any small perturbation decays exponentially and the homogeneous state is linearly stable.
- Conserved Type I instability (example in Fig. 2.2): One branch of the dispersion relation becomes positive over a finite band of unstable modes $q \in [q_{\min}, q_{\max}]$, while satisfying the characteristic constraint $\sigma(q = 0) = 0$, imposed by the conservation law. This type of instability selects a finite characteristic wavelength already at the linear level.

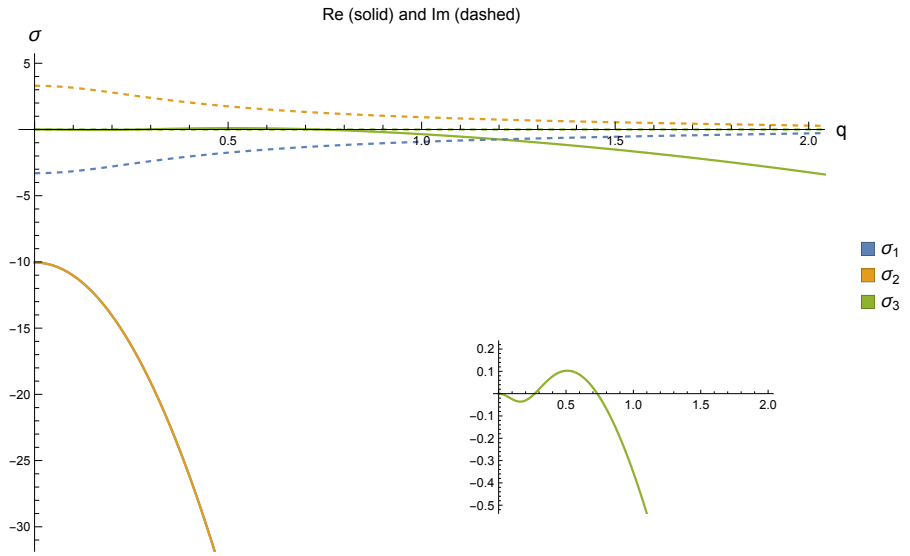

Figure 2.2: Example of conserved Type I instability, corresponding to the the green region in parameter space of Fig. 2.4. The dispersion relations are evaluated for $\lambda = 10$ and $\bar{\rho} = 3.75$. The instability of the unstable branch σ_3 occurs first at a nonzero wavenumber $q_{\min} > 0$. The dispersion relation is qualitatively different from a standard Type I instability because the graph always passes through the point $(q, \sigma) = (0, 0)$ reflecting the presence of a conserved quantity. The remaining two branches are complex conjugate eigenvalues with negative real parts.

- Type II instability (example in Fig. 2.3): Similarly to the previous case, one branch of the dispersion relation presents an unstable band. The instability first appears at zero wavenumber and extends continuously over the interval $q \in [0, q_{\max}]$. This long-wavelength instability is analogous to that governing phase separation in conserved systems such as the Cahn–Hilliard equation.

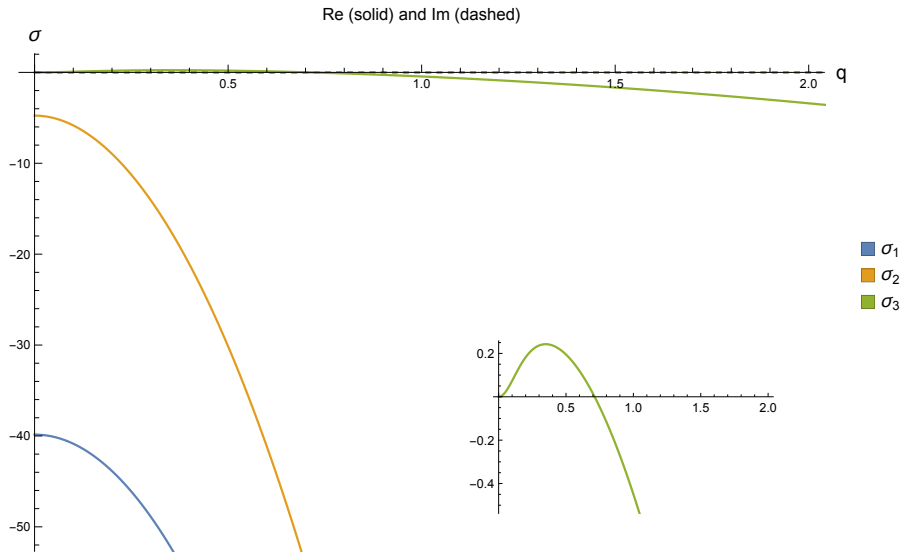

Figure 2.3: Example of Type II instability, corresponding to the pink region in parameter space of Fig. 2.4. The dispersion relations are evaluated for $\lambda = 45$ and $\bar{\rho} = 2.5$. The unstable branch of the dispersion relation σ_3 presents a long-wavelength instability typical of conserved systems as Cahn–Hilliard model. The other eigenvalues are real and always negative for all wavenumbers q.

An important feature of the present model is that the unstable eigenvalue is purely real over the parameter space. Consequently, the linear dynamics never undergo a Hopf bifurcation and cannot generate either oscillatory or traveling-wave patterns. Such behaviors require additional non-equilibrium mechanisms that are absent from the present minimal model, for example reversible reaction pathways such as those present in the Rho GTPase network discussed in Fig. 1.2.

Figure 2.4 shows the linear stability analyses around homogeneous steady states throughout the parameter space $(\lambda, \bar{\rho})$.

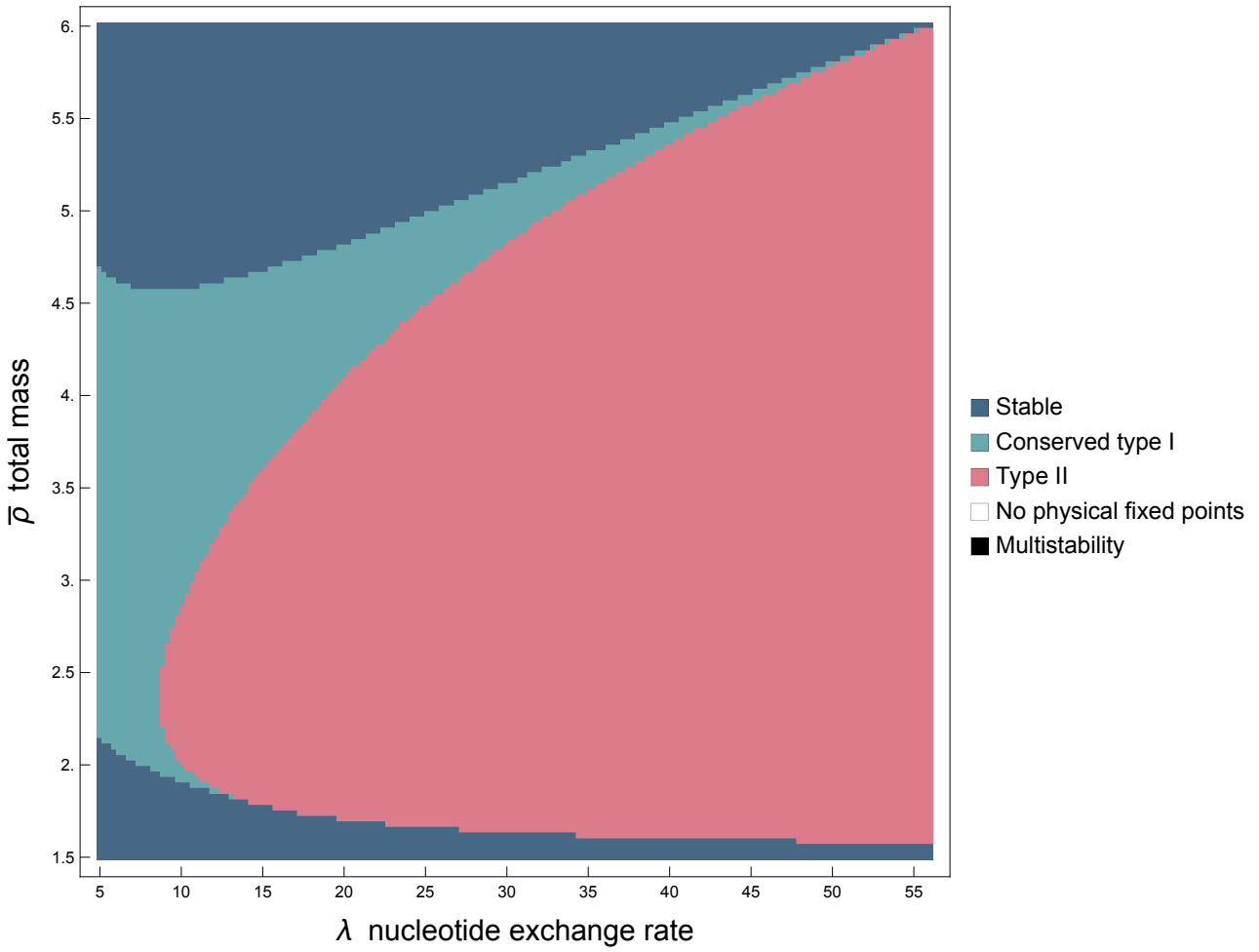

Figure 2.4: Linear stability diagram. The total protein mass density $\bar{\rho}$ and the nucleotide exchange rate λ are the control parameters, while all other parameters are kept fixed as specified in Eq.(2.23). In each point of the parameter space there is always a single physical homogeneous steady state with three positive concentrations (m^*, c_i^*, c_a^*). We can observe three different behaviors: in blue stable homogeneous regime, in green conserved Type I instability, and in pink Type II instability.

Although the LSA provides a useful starting point accurately predicts the onset of pattern formation, it seems that there isn't a good correlation between the type of instability and the expected pattern as described in literature. In fact, it provides only information about the growth of infinitesimal perturbations and does not determine the morphology of the fully developed nonlinear patterns. Characterizing these nonlinear states therefore requires direct numerical simulations of the complete reaction–diffusion system. The resulting phase diagram is shown in Fig. 2.5.

Remarkably, despite its minimal construction, the model exhibits a rich variety of stationary patterns that closely resemble those observed in vitro Min protein reconstitution experiments. Depending on the control parameters, the system supports homogeneous states, localized and extended stripes, dot-like structures, and foam-like morphologies.

A particularly interesting feature of the phase diagram emerges when the nucleotide exchange rate is kept fixed while varying the total protein mass. For example, along the cut corresponding to $\lambda = 34.5$, increasing $\bar{\rho}$ drives a sequence of transitions between stripe-like and dot-like patterns. These observations indicate that the total conserved mass plays a fundamental role in determining the selected pattern morphology.

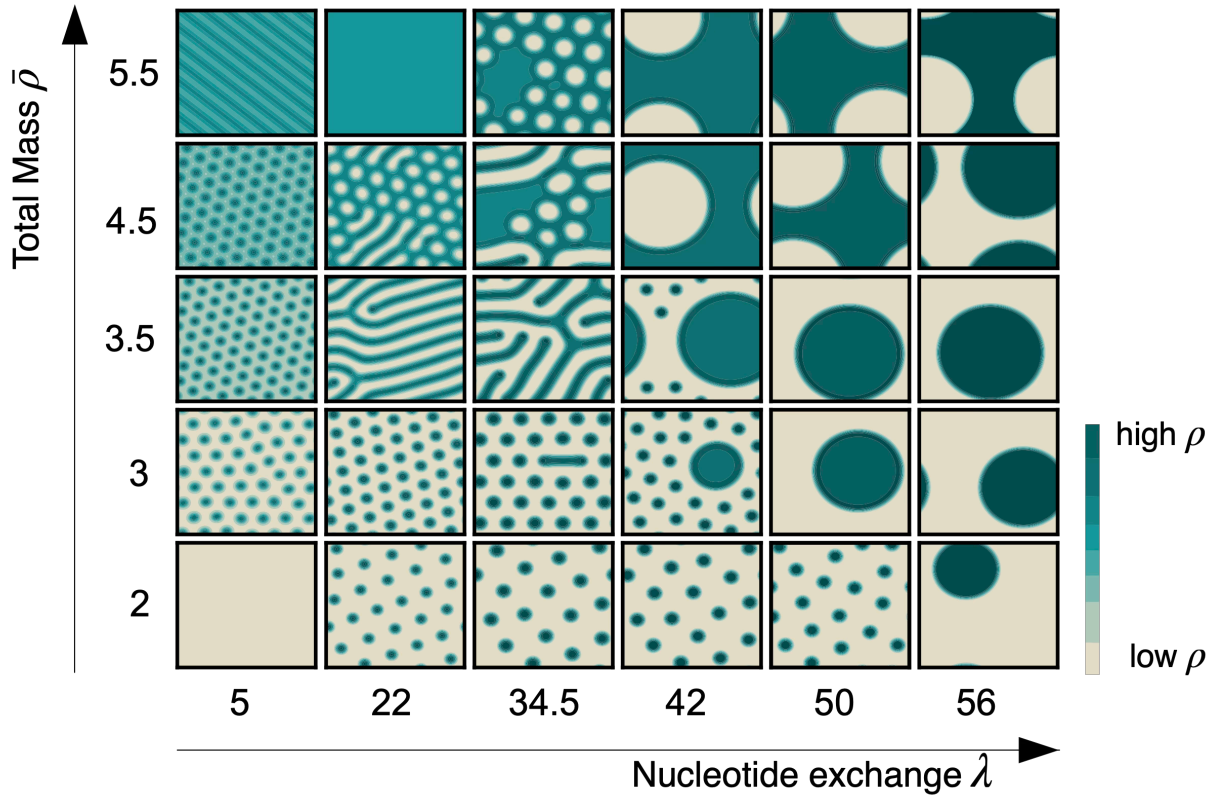

Figure 2.5: Phase diagram of the three-component McRD as a function of the average total mass density $\bar{\rho}$ and the nucleotide exchange rate λ. In the diagram are plotted the typical late time patterns of the local total mass density $\rho(\mathbf{x}, t)$. The model exhibits a rich variety of stationary patterns that are observed in vitro systems, including stripes, dots, and foam-like structures. In particular for fixed nucleotide exchange λ, for examples column $\lambda = 34.5$, variations of the total mass $\bar{\rho}$ can drive a transition from stripe-like to dot-like structures.

Chapter 3

Pearling instability

The main goal of the thesis work is to understand the mechanisms governing the pattern transitions described at the end of the previous chapter. In particular, we focus on the stability of localized stripe solutions and the onset of the pearling instability, through which an extended stripe loses stability and breaks up into a sequence of aligned dots. Characterizing this instability provides insight into the selection and robustness of localized patterns in mass-conserving reaction-diffusion systems.

Before introducing the formal mathematical framework, we briefly outline the physical phenomena and key structural definitions governing the pearling instability.

A "branch" is a straight stripe pattern formed in the total mass field $\rho(\mathbf{x}, t)$. In the fast-cytosolic-diffusion regime ($D_c \gg D_m$), this profile is mirrored directly in the membrane-bound protein density $m(\mathbf{x}, t)$, forming a high-density stripe flanked by two low-density plateaus. While the plateaus represent inert equilibria, the branch profile is a dynamic steady state sustained by a balance between reaction-driven cytosolic and membrane fluxes.
The pearling instability occurs when such a stripe, subjected to a transverse perturbation, fails to relax back to its unperturbed state and instead undergoes morphological transition into a periodic sequence of localized dots ("pearls").

Whether the system undergoes break-up or relaxation is dictated by mass redistribution along the stripe. A localized variation in branch width perturbs the local attachment-detachment balance, thereby driving mass exchange between wider and narrower regions. Depending on the sign of this response, the resulting redistribution either amplifies the initial width perturbation, triggering the pearling instability, or opposes it, restoring the unperturbed branch configuration.

Formalizing this physical mechanism and establishing a precise quantitative criterion is the central focus of the remainder of this chapter. First, we construct the unperturbed stationary branch solution (Sec. 3.1). Next, we introduce the key assumption that perturbations are confined to the attachment zone (Sec. 3.2). This framework allows us to clarify the physical principles driving the pearling mechanism (Sec. 3.3). Finally, we analytically derive a linear stability theory and the corresponding dispersion relation to provide the exact quantitative criteria for the onset of the instability (Sec. 3.4).

3.1 Stationary branches

The starting point of our analysis is a stationary, unperturbed branch pattern which is assumed to be a localized straight stripe, translationally invariant in the longitudinal direction (independent of the y-coordinate), whose profile along x is peaked, i.e. it rises from a low plateau to a high value and back.

The dynamics along x and along y occur on different timescales: along x the system equilibrates quickly to a stationary profile, while along y mass is redistributed slowly between slices. Each slice of the branch is therefore approximately at steady state, and the mass flow we are interested in occurs

mainly parallel to the direction of the branch axis. In particular, this observation allows us to base our analysis on slices rather than on the entire spatial concentration profiles.

We defined two different regions in space related to the local reaction term R and the curvature of the slice profile:

- Attachment zone: region of local positive protein flux onto the membrane, $R(\mathbf{x}) > 0$. Since Eq. (2.19) holds at stationarity, a positive reaction term corresponds to negative curvature, and, in general, to the high-density region.
- Detachment zone: region of local detachment from the membrane, $R(\mathbf{x}) < 0$, positive curvatures and low density.

In the case of monotonic interface profile (no change in sign of the profile derivative with respect to x-coordinate between the lower plateau and the upper peak), the attachment zone is the inner region between the two inflection points, while the detachment zone is the outer regions from the inflections to the boundaries. The branch width is defined as the distance between the inflection points.

The three-component McRD can present also non-monotonic interface profiles, usually characterized by small horn-like structures near the interface. In that case the local-sign definition above must be relaxed in favor of a net condition on each zone, which reads

$$\begin{aligned} \int_{\text{att}} dx\, R > 0 \quad &\Longrightarrow \quad \text{attachment zone}, \\ \int_{\text{det}} dx\, R < 0 \quad &\Longrightarrow \quad \text{detachment zone}. \end{aligned} \tag{3.1}$$

It means that in the attachment zone, which is delimited by the two "main" inflection points, the net amount of protein attaching to the membrane per unit of time is positive, even though local regions of negative R could be present; conversely, the detachment zone has a net detachment rate even though local attachment points may exist within it.

Unperturbed stationary branch solutions are extrusions along y of a one-dimensional stationary slice profile and are described by the following equations:

$$\begin{cases} \rho(x,y) = \rho_{r_0}(x) \\ \eta(x,y) = \eta_{r_0} = \text{const}\ , \\ c_i(x,y) = c_{i,r_0}(x) \end{cases} \tag{3.2}$$

where r_0 is the half-width of the branch, i.e. the distance from the center of the branch to the "main" inflection point of the density profile. When considering a symmetric domain centered at the origin along the x-axis in theoretical definitions and derivations, r_0 can denote both the half-width and the position of the inflection point. Thus r_0 is defined by

$$\partial_x^2 \rho_{r_0}(x)\big|_{x=r_0} = 0, \quad \int_{-r_0}^{+r_0} dx\, R > 0. \tag{3.3}$$

Determining a stationary solution analytically requires solving the one-dimensional reduction of Eq. (2.20) for the three fields $\rho_{r_0}(x)$, $\eta_{r_0}(x)$ and $c_{i\,r_0}(x)$. While imposing a constant η_{r_0} is straightforward, the remaining equations for $\rho_{r_0}(x)$ and $c_{i\,r_0}(x)$ cannot be solved analytically due to the non-linear reaction terms. Note that since all subsequent stability analyses depend exclusively on the profiles of η and ρ, the cytosolic component c_i will not be addressed further.
For this reason, we adopt a semi-analytical approach, meaning that we construct stationary profiles $\rho_{r_0}(x)$ from one-dimensional numerical simulations performed in *Mathematica*, by integrating the one-dimensional McRD equations with `NDSolve` until a stationary state is reached. The computational domain is fixed to $x \in [0, L]$, with $L = 100$, and no-flux boundary conditions are imposed, meaning

$$\begin{cases} \partial_x m(x,t)\big|_{x=0} = 0 = \partial_x m(x,t)\big|_{x=L} \\ \partial_x c_a(x,t)\big|_{x=0} = 0 = \partial_x c_a(x,t)\big|_{x=L}\ . \\ \partial_x c_i(x,t)\big|_{x=0} = 0 = \partial_x c_i(x,t)\big|_{x=L} \end{cases} \tag{3.4}$$

As initial condition we use the branch-like profile

$$\rho_a(x) = b - c\,\tanh\left(|x - L/2| - a\right) \quad \text{for } x \in [0; L], \tag{3.5}$$

where the constants b and c are chosen to fix the plateau values corresponding to the attachment and detachment zones densities, respectively $\rho_{\text{att}} = b + c$ and $\rho_{\text{det}} = b - c$. Thus physical constraint of positive local concentrations requires $b > c > 0$, consistent with $\rho_{\text{att}} > \rho_{\text{det}} > 0$. The parameter a controls the width of the initial branch. Indeed, the two inflection points are located at $x_1 = L/2 - a$ and $x_2 = L/2 + a$, so that the initial half-width is simply a. Once parameters b and c are fixed, the total mass of the system $\bar{\rho}\,\mathcal{V}$ is determined by a. Hereafter, assuming a constant volume $\mathcal{V}$, $\bar{\rho}$ will be referred to simply as the total mass.
The absolute value ensures that the branch is centered in the computational domain $x \in [0, L]$. Although this profile is not an exact stationary solution, it provides an excellent initial guess from which the numerical dynamics rapidly relaxes toward a stationary branch.

The corresponding guess profile is shown in the left side of Fig. 3.1. It is important to emphasize that it represents only a one-dimensional cross section of the full two-dimensional pattern. The corresponding localized branch in (x, y) plane is obtained by extruding the profile uniformly along the y-direction, as illustrated in right part of the picture.

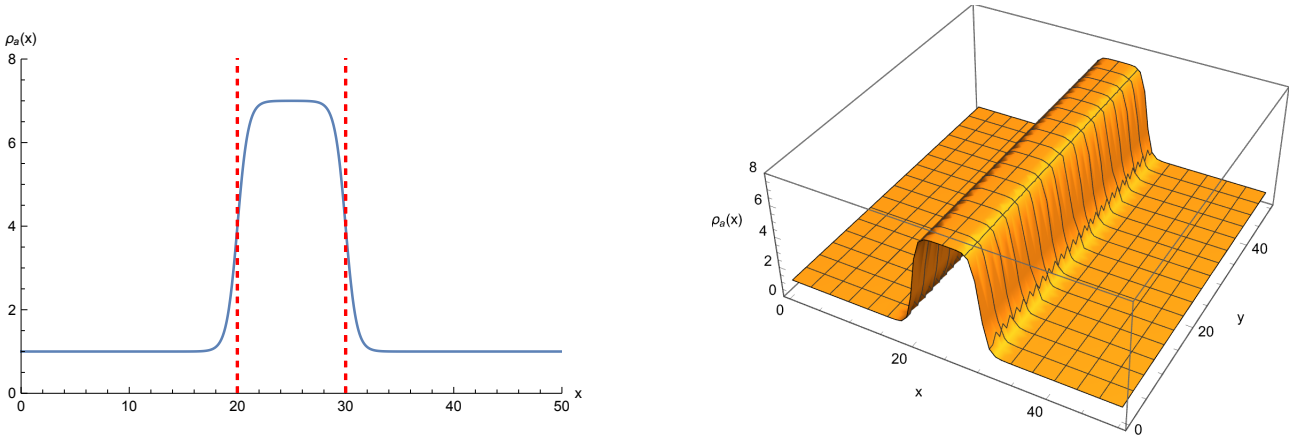

Figure 3.1: **Left**: Initial guess profile $\rho_a(x)$ on the domain $[0, 50]$ with $r_0 = a = 5$, $b = 4$, and $c = 3$. The initial attachment zone is located between the two inflection points highlighted in red ($x \in [20, 30]$) and its peak value is $\rho_{\text{att}} = 7$. The outer regions are the detachment zones with plateau value $\rho_{\text{det}} = 1$. Notice that analytical guess profiles typically have monotonic interfaces, so attachment and detachment are initially determined purely by the local profile curvature.
Right: Extrusion of profile $\rho_a(x)$, presented in the left panel, along y-direction. The resulting pattern is a localized straight branch profile in a two-dimensional square geometry with $L = 50$.

In the biologically relevant regime $D_c \gg D_m$, the rapid cytosolic diffusion implies that the total mass is well approximated by the membrane-bound, meaning $m \to \rho$. Consequently, the initial condition is set to $m(x, t = 0) = \rho_a(x)$, yielding

$$\begin{cases} m(x, t = 0; a) = \rho_a(x) \\ c_a(x, t = 0) = 0 \\ c_i(x, t = 0) = 0 \end{cases}. \tag{3.6}$$

Throughout this work, the parameters are fixed to $b = 4$ and $c = 3.2$, as these values provide robust convergence across a broad ranges of λ and a. Moreover, we fix the nucleotide exchange rate to $\lambda = 35$, corresponding to the lowest value for which localized stationary branches are observed. In this way the only free parameters left is a which is connected with the total mass of the system $\bar{\rho}$.

The same procedure applies to a branch with inverted zones, i.e. detachment in the inner region and attachment in the outer regions; the corresponding guess profile is obtained by flipping the sign in front of the tanh() term, meaning $\rho_a(x) = b + c\,\tanh\left(|x - L/2| - a\right)$ keeping $b > c > 0$.

Starting from these initial conditions, the numerical dynamics relaxes toward a stationary branch profile $\rho_{r_0}(x)$. A profile is accepted as stationary only if the redistribution potential becomes spatially uniform, in agreement with the stationarity condition derived in the previous section. More precisely, we require

$$\delta\eta \equiv \frac{\eta_{\max} - \eta_{\min}}{\bar{\eta}} < 10^{-6}, \tag{3.7}$$

where $\bar{\eta}$ denotes the spatial average of η over the computational domain.

Examples of the resulting stationary profiles are shown in Figs. 3.2 and 3.3. Compared with the initial guess, the relaxation slightly modifies both the branch width and the plateau densities while preserving the total mass. Narrow branches retain nearly monotonic interfaces, whereas wider branches progressively develop non-monotonic interfaces characterized by pronounced peaks at the boundaries of the attachment region.

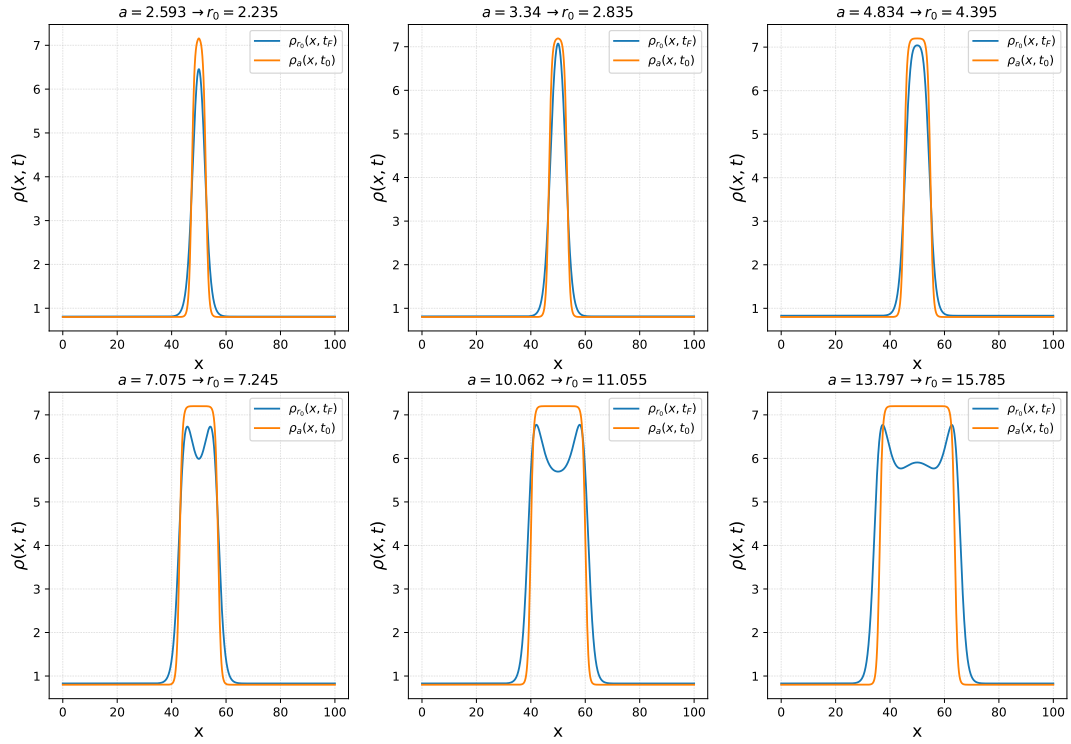

Figure 3.2: Comparison between analytical guess profiles given by Eq. (3.5) (orange) and the corresponding stationary branch profiles (blue). Stationary solutions $\rho_{r_0}(x)$ are calculated numerically relaxing the initial guess condition $\rho_a(x)$. The branch half-width change from a to r_0, with consequently small changes in the peak and plateau values that preserve total mass $\bar{\rho}$. Narrow branches have monotonic interfaces (upper row), while thinner branches develop non-monotonic interfaces (bottom row).

3.2 Reduced description

The one-dimensional stationary branch profiles of Sec. 3.1 are used as initial conditions for the pearling instability analysis, in which we study the branch's response to transverse perturbations of its width.

We describe such perturbations by allowing the branch half-width to depend on the transverse coordinate and on time, introducing a position-dependent interface location $r = r(y,t)$, with $r(y,t) = r_0$ recovering the unperturbed solution. As noted in Sec. 3.1, the main assumption taken into account for the derivation concerns a time-scale separation between the dynamics along x (fast relaxation to a locally stationary profile) and along y (slow mass redistribution). This separation is what allows us to perform a quasi-stationary (or adiabatic) approximation, which consists in treating each transverse cross-section of the branch, at fixed y, as a locally relaxed one-dimensional stationary profile parametrized by the instantaneous local width $r(y,t)$.

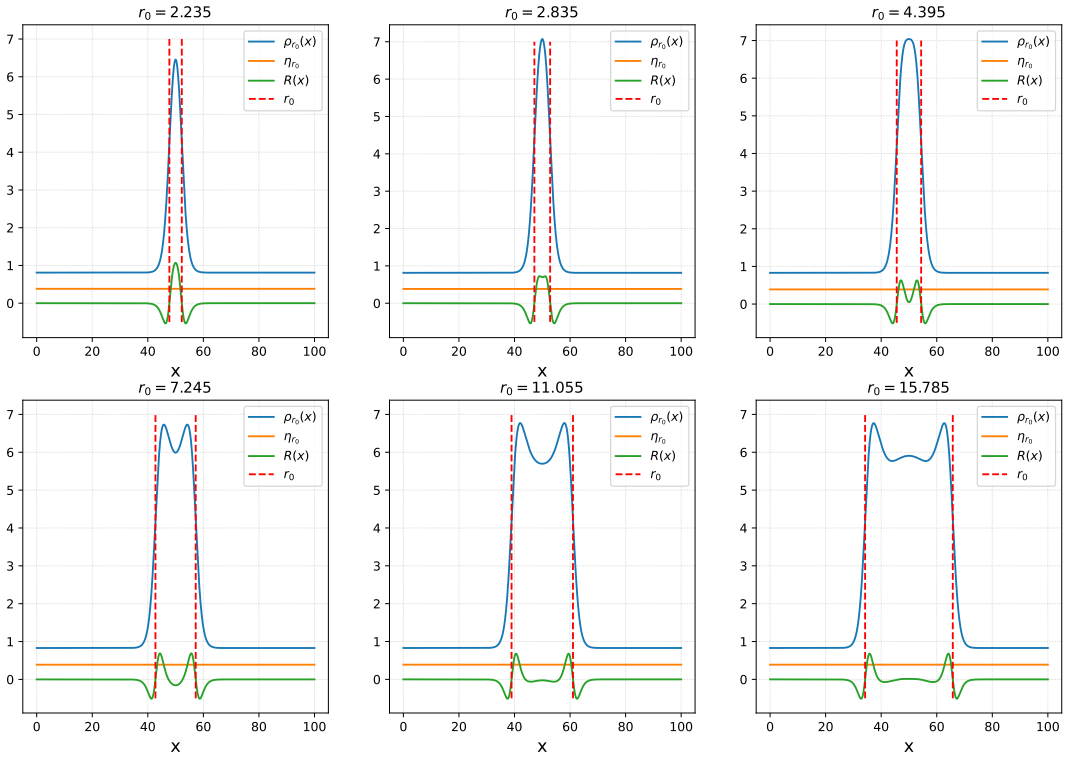

Figure 3.3: Stationary solutions for different total mass (or equivalently, half-branch width). Once we get the stationary branch profiles, we evaluate the mass redistribution potential η_{r_0} (orange) and the local reaction term $R(\rho_{r_0}, \eta_{r_0}, c_{i\,r_0})$ (green). The η potential must be constant while the sign of R is related to the local curvature of the density profile. In red are highlighted the "main" inflection points which enclose the attachment zone.

Within this approximation, we make one further simplification: only the attachment (inner) zone of the branch is taken to follow the local perturbation. Conversely, the detachment (outer) zone remains close to the unperturbed profile, ensuring that any perturbation decays to zero for large x. In equations, our ansatz reads:

- attachment zone (inner):

$$\rho_{\text{att}}(x, y, t) \approx \rho_{r(y,t)}(x), \quad \eta_{\text{att}}(x, y, t) \approx \eta_{r(y,t)}; \tag{3.8}$$

- detachment zone (outer):

$$\rho_{\text{det}}(x, y, t) \approx \rho_{r_0}(x), \quad \eta_{\text{det}}(x, y, t) \approx \eta_{r_0}. \tag{3.9}$$

Confining the leading-order perturbations strictly to the attachment zone is physically justified by the different roles of the two regions. Deep in the detachment zone, the profile sits at a linearly stable, homogeneous fixed point of the local reaction kinetics, $R(\rho_{\text{det}}, \eta_{\text{det}}, c_{i,\text{det}}) = 0$. Because this region is constrained at a stable fixed point, it resists reshaping. Moreover, since it occupies most of the domain outside the narrow attachment region, any finite mass flux exchanged with it is spread over a comparatively large capacity and produces only a vanishing change in its bulk state.
The detachment zone thus behaves as a quasi-stationary reservoir: it can absorb or supply mass without its own profile responding appreciably to a change of the interior width $2r$. Conversely, the attachment zone is a interfacial structure sustained by a balance between diffusion and reaction, and it is precisely there that R and η are sensitive to a change in r. A perturbation of the branch width therefore reshapes the interior while leaving the exterior essentially unperturbed.

This construction introduces a step-like discontinuity both in the η potential and in the density profile ρ at the matching points $x = \pm r(y, t)$, since it glues a profile from the $r(y, t)$-family to one drawn from the r_0-family. Figure 3.4 schematically illustrates the principle of this approximation.

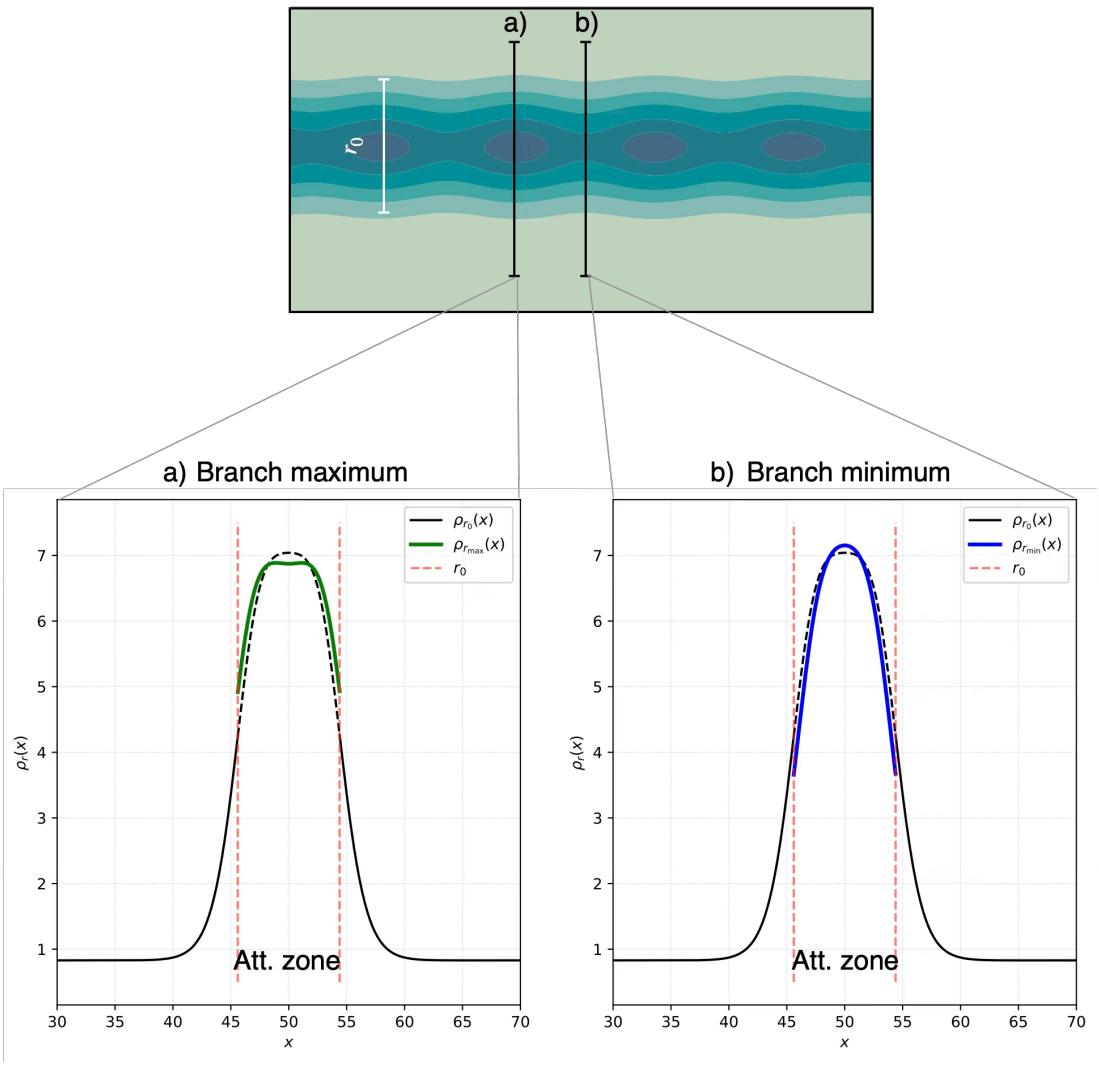

Figure 3.4: Example of a perturbed branch profile, where the branch width varies transversely across different local cross-sections. Specifically, slice a) is located at the maximum width, whereas slice b) corresponds to a minimum. In both cases, the detachment zone is approximated by the unperturbed profile $\rho_{r_0}(x)$. Conversely, the attachment zone is replaced by a stationary profile corresponding to the local width: a wider stationary profile is depicted in green, and a narrower one in blue. This approximation is valid only asymptotically for infinitesimal perturbations, as this formulation introduces a discontinuity in both the slice profile and on the mass redistribution potential, respectively $\rho_{r(y,t)}(x)$ and $\eta_{r(y,t)}$ for fixed y.

Before proceeding, it is important to emphasize that the ansatz introduced above is only an approximation and is not strictly physically consistent. In particular, the assumed perturbation makes the mass-redistribution potential η piecewise constant, with discontinuities at the interfaces $x = \pm r(y,t)$. As a consequence, the gradient of η vanishes everywhere except at these discontinuities, artificially suppressing mass transport along the x-direction throughout the bulk of the attachment and detachment regions. Likewise, the corresponding discontinuity in the total mass density ρ is also nonphysical, since ρ is a diffusive field and should remain continuous under the reaction-diffusion dynamics.

A more consistent ansatz therefore requires perturbing not only the attachment region but also the surrounding detachment zone, allowing the perturbed fields to connect smoothly to the unperturbed stationary profile far from the branch,

$$\rho_{\text{det}}(x,y,t) \approx \rho_{r_0}(x) + \delta\rho(x,y,t), \qquad \eta_{\text{det}}(x,y,t) \approx \eta_{r_0} + \delta\eta(x,y,t), \tag{3.10}$$

where the perturbations satisfy $\delta\rho(x \to \pm\infty, y, t) \to 0$ and $\delta\eta(x \to \pm\infty, y, t) \to 0$, ensuring that both fields remain continuous at $x = \pm r(y,t)$ and asymptotically recover the stationary branch profile.

The perturbation fields $\delta\rho$ and $\delta\eta$ can, in principle, be obtained analytically by solving the linearized

equations subject to continuity conditions at the interfaces and the asymptotic boundary conditions at infinity. The linear theory derived in Sec. 3.4 is then modified by boundary correction terms that account for the weak mass redistribution along the x-direction. The resulting stability problem is no longer a standard eigenvalue problem but instead leads to a self-consistent transcendental dispersion relation. Solving this problem lies beyond the scope of the present work and is left for future investigation.

It is useful, in view of the calculation of the next sections, to define the reactive turnover. At the unperturbed stationary branch it is

$$\begin{aligned} Tr_{r_0} &\equiv -\int_{-\infty}^{-r_0} dx\ R(\rho_{r_0}(x), \eta_{r_0}, c_{i\,r_0}(x)) \\ &\equiv -\int_{+r_0}^{+\infty} dx\ R(\rho_{r_0}(x), \eta_{r_0}, c_{i\,r_0}(x)) \quad . \\ &\equiv +\frac{1}{2}\int_{-r_0}^{+r_0} dx\ R(\rho_{r_0}(x), \eta_{r_0}, c_{i\,r_0}(x)) \end{aligned} \tag{3.11}$$

Physically, it represents half of the net number of proteins binding to the membrane within the attachment zone (inner region of the branch) per unit of time. Because of mass conservation, this quantity is equivalent to half the net number of proteins detaching from the membrane in the detachment zone, which explains the equivalence of the three definitions above. Indeed, at steady state with no-flux boundary conditions,

$$\begin{aligned} D_m\nabla^2\rho^{\mathrm{sta}} &= -R(\rho^{\mathrm{sta}}, \eta^{\mathrm{sta}}, c_i^{\mathrm{sta}}) \\ \int_\Omega dA\ D_m\nabla^2\rho^{\mathrm{sta}} &= -\int_\Omega dA\ R(\rho^{\mathrm{sta}}, \eta^{\mathrm{sta}}, c_i^{\mathrm{sta}}) \\ \oint_{\partial\Omega} dS\ D_m\nabla\rho^{\mathrm{sta}}\cdot\mathbf{n} &= -\int_\Omega dA\ R(\rho^{\mathrm{sta}}, \eta^{\mathrm{sta}}, c_i^{\mathrm{sta}}) \\ 0 &= \int_\Omega dxdy\ R(\rho^{\mathrm{sta}}, \eta^{\mathrm{sta}}, c_i^{\mathrm{sta}}). \end{aligned} \tag{3.12}$$

For a stationary branch solution (i.e. depending only on the x-coordinate), calculations reduces to

$$\begin{aligned} D_m\partial_x^2\rho_{r_0}(x) &= -R(\rho_{r_0}(x), \eta_{r_0}, c_{i\,r_0}(x)) \\ \int_{L_x} dx\ D_m\partial_x^2\rho_{r_0}(x) &= -\int_{L_x} dx\ R(\rho_{r_0}(x), \eta_{r_0}, c_{i\,r_0}(x)) \\ 0 &= \int_{L_x} dx\ R(\rho_{r_0}(x), \eta_{r_0}, c_{i\,r_0}(x)). \end{aligned} \tag{3.13}$$

Under the adiabatic approximation introduced above, each transverse slice is assumed to remain close to a one-dimensional stationary branch characterized by its local half-width $r(y,t)$. Consequently, the reactive turnover can be promoted to a local quantity,

$$\begin{aligned} Tr_{r(y,t)} &\equiv -\int_{-\infty}^{-r(y,t)} dx\ R(\rho_{r(y,t)}(x), \eta_{r(y,t)}, c_{i\,r(y,t)}(x)) \\ &\equiv -\int_{+r(y,t)}^{+\infty} dx\ R(\rho_{r(y,t)}(x), \eta_{r(y,t)}, c_{i\,r(y,t)}(x)) \quad . \\ &\equiv +\frac{1}{2}\int_{-r(y,t)}^{+r(y,t)} dx\ R(\rho_{r(y,t)}(x), \eta_{r(y,t)}, c_{i\,r(y,t)}(x)) \end{aligned} \tag{3.14}$$

where the three expressions remain equivalent because each slice is assumed to satisfy the one-dimensional steady-state condition $\int dx\, R(\rho_r(x), \eta_r, c_{i,r}(x)) = 0$.

In the simplified ansatz adopted in this chapter, however, only the attachment region is perturbed, while the detachment zone is kept fixed at the unperturbed stationary profile. As discussed above, this approximation does not preserve the local steady-state condition exactly. Consequently, the reactive turnover associated with the attachment region, $Tr_{r(y,t)}$, no longer matches the turnover in the detachment region, Tr_{r_0}, which is still determined by the unperturbed profile. This local turnover imbalance is the key ingredient of the approximate linear theory developed in the following sections.

3.3 Physical mechanism

Allowing the branch half-width to vary from slice to slice, $r = r(y,t)$ as introduced in Sec. 3.2, changes the local balance encoded by R, and consequently the local potential η_r differs from η_{r_0}. Two behaviors are then possible.

If a region becomes locally wider ($r(y,t) > r_0$) and its potential decreases accordingly ($\eta_{r(y,t)} < \eta_{r_0}$), or equivalently, if a thinner branch has a higher potential, then

$$\partial_r \eta_r \big|_{r=r_0} < 0. \tag{3.15}$$

This generates a mass flux $\mathbf{J}_\rho = -D_c \nabla \eta$ directed from high-η (narrow) to low-η (wide) regions. The flux amplifies the initial perturbation and the process self-reinforces, therefore the stationary branch is unstable. This mechanism is illustrated in Fig. 3.5.

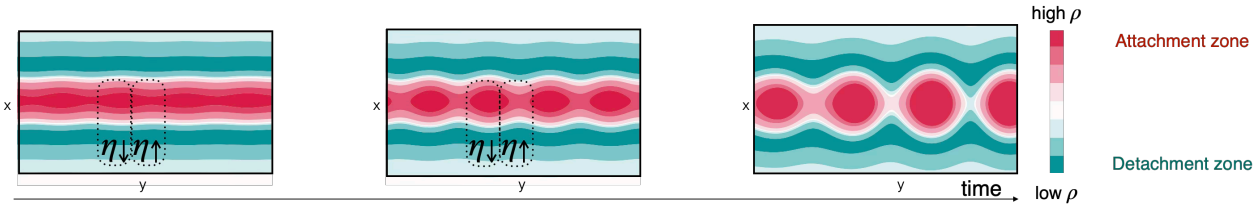

Figure 3.5: Cartoon of an unstable branch solution that breaks up through the Pearling instability mechanism. The local total mass density $\rho(\mathbf{x}, t)$ is represented with gradient colors, in particular high density regions (attachment zones) are in red while low density regions (detachment zones) are in green. In this case, wider regions correspond to a decrease in the mass redistribution potential η, and consequently, the mass flows from the narrower regions to the wider ones. The process is self-reinforcing and leads to the pearling instability.

In the opposite situation, a locally thinner branch corresponds to an increase of the local mass redistribution potential (and vice-versa),

$$\partial_r \eta_r \big|_{r=r_0} > 0. \tag{3.16}$$

The flux opposes the perturbation, the branch relaxes back to its unperturbed steady state and is therefore stable, as shown in Fig. 3.6.

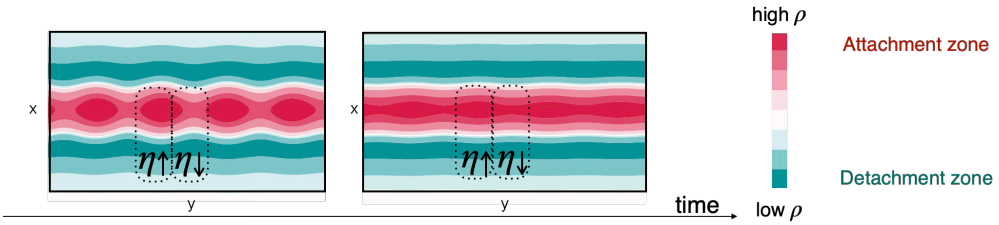

Figure 3.6: Cartoon of a stable branch solution. The local total mass density $\rho(\mathbf{x}, t)$ is represented with gradient colors, in particular high density regions (attachment zones) are in red while low density regions (detachment zones) are in green. Since the η potential increases in thinner regions, the perturbations are suppressed exponentially fast in time. From left to right, as the time evolves the system returns to the unperturbed stable branch profile.

3.4 Linear stability of a branch

The sign of $\partial_r \eta_r|_{r=r_0}$ should be the stability criterion for the pearling instability. Evaluating it explicitly, using the asymptotic matching framework of Sec. 3.2, is the object of the linear stability (dispersion relation) analysis carried out in the current section.

For notational simplicity, we denote $r = r(y,t)$, and explicitly indicate the case $r = r_0$ only when needed.

Integration in the inside region. First, we integrate the ρ's equation (Eq. (2.13)) over the attachment zone:

$$\int_{-r}^{+r} dx\ \partial_t \rho_r(x) = \int_{-r}^{+r} dx\ D_c \nabla^2 \eta_r. \tag{3.17}$$

We rewrite the left-hand side using the Leibniz rule

$$\frac{d}{dt}\int_{a(t)}^{b(t)} dc\ f(x,t) = \int_{a(t)}^{b(t)} dx\ \partial_t f(x,t) + f(x,t)\big|_{x=b(t)} b'(t) - f(x,t)\big|_{x=a(t)} a'(t), \tag{3.18}$$

that in our case means

$$\frac{d}{dt}\int_{-r}^{+r} dx\ \rho_r(x) = \int_{-r}^{+r} dx\ \partial_t \rho_r(x) + \rho_r(x)\big|_{x=r}\,\partial_t r - \rho_r(x)\big|_{x=-r}\partial_t(-r). \tag{3.19}$$

Assuming the branch is symmetrical, with a transverse axis of symmetry at the midpoint between the two inflection points, i.e. $\rho_r(x)|_{x=r} = \rho_r(x)|_{x=-r}$, and isolating the term of our interest, the expressions simplifies to

$$\int_{-r}^{+r} dx\ \partial_t \rho_r(x) = \frac{d}{dt}\int_{-r}^{+r} dx\ \rho_r(x) - 2\rho_r(x)\big|_{x=r}\partial_t r. \tag{3.20}$$

On the right-hand side, we exploit the fact that our ansatz for η_r (Eqs.(3.8)-(3.9)) is constant along x-direction, apart from the step-like discontinuity at the interfaces. Consequently, the Laplacian operator reduces to a second derivative in y, namely $\nabla^2 \eta_r \to \partial_y^2 \eta_r$.
The the integral in x can be easily evaluate, as the expression $\partial_y^2 \eta_r$ is x-independent, giving

$$\int_{-r}^{+r} dx\ \partial_y^2 \eta_r = 2r\,\partial_y^2 \eta_r. \tag{3.21}$$

Finally, we introduce a new variable representing the total mass within the attachment zone, defined as:

$$\phi_{r(y,t)} \equiv \int_{-r(y,t)}^{+r(y,t)} dx\ \rho_{r(y,t)}(x). \tag{3.22}$$

A graphical representation of this definition is illustrated in Fig. 3.7.

By combining the previous results, we obtain the governing equation for the spatiotemporal evolution of the ϕ_r field in the inside region

$$\boxed{\partial_t \phi_r - 2\rho_r(x)\big|_{x=r}\partial_t r\ = 2D_c r\,\partial_y^2 \eta_r \quad (\phi - \text{inside region})}. \tag{3.23}$$

Similarly, we integrate also the η's equation (Eq. (2.13)) in the attachment zone:

$$\int_{-r}^{+r} dx\ \partial_t \eta_r = \int_{-r}^{+r} dx\ \left[(D_c + D_m)\nabla^2 \eta_r - D_m \nabla^2 \rho_r(x) - R(\rho_r(x), \eta_r, c_{i\,r}(x))\right]. \tag{3.24}$$

On the left-hand side, the expression under the integral is again x-independent and the integral is easy to evaluate:

$$\int_{-r}^{+r} dx\ \partial_t \eta_r = 2r\,\partial_t \eta_r. \tag{3.25}$$

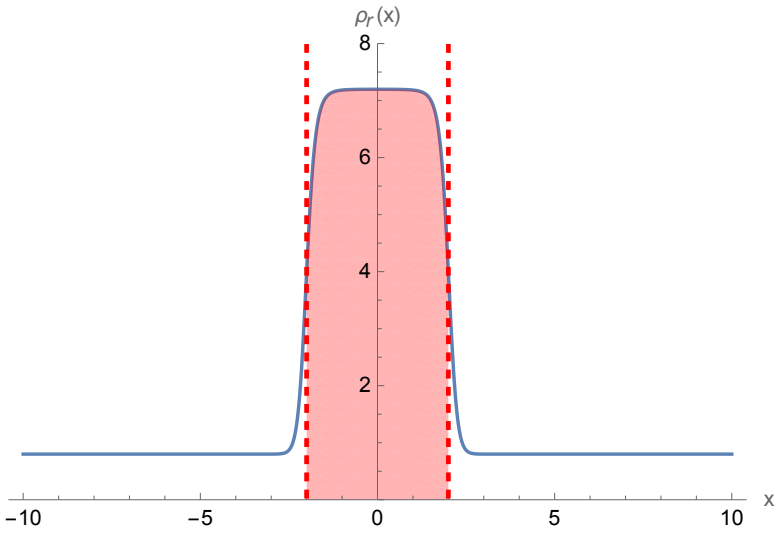

Figure 3.7: Graphical representation of the total mass within the attachment zone. Indeed, the red area is ϕ_r which is defined as the integral of the total local density $\rho_r(x)$ over the attachment zone, i.e over the interval $[-r, r]$. The dashed red lines indicate the inflection points of the $\rho_r(x)$ profile.

Regarding the right-hand side, we can decompose the calculations in three different parts.

i) Reaction term (direct application of reactive turnover definition given in Eq. (3.14)):

$$\int_{-r}^{+r} dx \; -R(\rho_r(x), \eta_r, c_{i\,r}(x)) = -2Tr_r. \tag{3.26}$$

ii) Diffusion of η_r (analogous calculations to those performed in Eq. (3.21) which allow us to bring $\partial_y^2\eta_r$ out of the integral):

$$\int_{-r}^{+r} dx \; (D_c + D_m)\nabla^2\eta_r = 2r\,(D_c + D_m)\,\partial_y^2\eta_r. \tag{3.27}$$

iii) Diffusion of ρ_r:

$$\begin{aligned}\int_{-r}^{+r} dx \; - D_m\nabla^2\rho_r(x) &= -D_m\left[\int_{-r}^{+r} dx\; \partial_x^2\rho_r(x) + \int_{-r}^{+r} dx\; \partial_y^2\rho_r(x)\right] \\ &\simeq -D_m\left[\cancel{\int_{-\infty}^{+\infty} dx\; \partial_x^2\rho_r(x)} - 2\int_{+r}^{+\infty} dx\; \partial_x^2\rho_{r_0}(x) + \int_{-r}^{+r} dx\; \partial_y^2\rho_r(x)\right] \\ &= \underbrace{2D_m\int_{+r}^{+\infty} dx\; \partial_x^2\rho_{r_0}(x)}_{B_1}\; \underbrace{-D_m\int_{-r}^{+r} dx\; \partial_y^2\rho_r(x)}_{B_2}.\end{aligned} \tag{3.28}$$

Note that, from first to second line, we switched from the inside profile ρ_r in the attachment zone, to the unperturbed profile ρ_{r_0} in the outside region, consistent with our ansatz of Eqs. (3.8)-(3.9), while from second to third line, we apply the no-flux boundary conditions.

The integration of the unperturbed profile $\partial_y^2\rho_{r_0}$ in the outside region can be evaluated using the stationary condition of Eq. (2.19), which implies

$$B_1 :\; 2D_m\int_{+r}^{+\infty} dx\; \partial_x^2\rho_{r_0}(x) = -\int_{+r}^{+\infty} dx\; R(\rho_{r_0}(x), \eta_{r_0}, c_{i\,r_0}(x)) = +2Tr_{r_0}. \tag{3.29}$$

Next, the integration of $\partial_y^2\rho_r$ in the attachment zone is decomposed by using the Leibniz rule Eq. (3.18) twice. This procedure extends the same differentiation rule first to the outer operator and then to the

inner derivative, yielding the following general formulation:

$$\begin{aligned}\frac{d^2}{dt^2}\int_{a(t)}^{b(t)} dx\ f(x,t) = &\int_{a(t)}^{b(t)} dx\ \partial_t^2 f(x,t)\\ &+ 2\partial_t f(x,t)\big|_{x=b(t)} b'(t) - 2\partial_t f(x,t)\big|_{x=a(t)} a'(t)\\ &+ \partial_x f(x,t)\big|_{x=b(t)} (b'(t))^2 - \partial_x f(x,t)\big|_{x=a(t)} (a'(t))^2\\ &+ f(x,t)\big|_{x=b(t)} b''(t) - f(x,t)\big|_{x=a(t)} a''(t)\end{aligned}. \tag{3.30}$$

By applying Eq. (3.30) to our case, we get

$$\begin{aligned}\frac{d^2}{dy^2}\int_{-r}^{+r} dx\ \rho_r(x) = &\int_{-r}^{+r} dx\ \partial_y^2\rho_r(x) + 2\partial_y\rho_r(x)\big|_{x=r}\partial_y r - 2\partial_y\rho_r(x)\big|_{x=-r}\partial_y(-r)\\ &+ \partial_x\rho_r(x)\big|_{x=r}(\partial_y r)^2 - \partial_x\rho_r(x)\big|_{x=-r}(\partial_y(-r))^2\\ &+ \rho_r(x)\big|_{x=r}\partial_y^2 r - \rho_r(x)\big|_{x=-r}\partial_y^2(-r)\\ = &\int_{-r}^{+r} dx\ \partial_y^2\rho_r(x) + 4\partial_y\rho_r(x)\big|_{x=r}\partial_y r + 2\partial_x\rho_r(x)\big|_{x=r}(\partial_y r)^2 + 2\rho_r(x)\big|_{x=r}\partial_y^2 r,\end{aligned} \tag{3.31}$$

where in the second step we simplified the expressions by exploiting the following symmetry assumptions

$$\rho_r(x)\big|_{x=r} = \rho_r(x)\big|_{x=-r}, \quad \partial_x\rho_r(x)\big|_{x=r} = -\partial_x\rho(x)\big|_{x=-r}, \quad \partial_y\rho_r(x)\big|_{x=r} = \partial_y\rho_r(x)\big|_{x=-r}. \tag{3.32}$$

Making the term $\int_{-r}^{+r} dx\ \partial_y^2\rho_r(x)$ explicit and incorporating the definition of ϕ_r given in Eq. (3.23) leads to

$$B_2:\ -D_m\int_{-r}^{+r} dx\ \partial_y^2\rho_r(x) = -D_m\left[\partial_y^2\phi_r - 2\rho_r(x)\big|_{x=r}\partial_y^2 r - 4\partial_y\rho_r(x)\big|_{x=r}\partial_y r - 2\partial_x\rho_r(x)\big|_{x=r}(\partial_y r)^2\right]. \tag{3.33}$$

where we color in gray the term which will contribute to order $\mathcal{O}(\epsilon^2)$ when the harmonic ansatz Eqs. (3.37)-(3.38) is made, and so we will neglect them.

Finally, combining all these terms allows us to formulate the governing equation for the η potential in the attachment zone as

$$\boxed{\begin{aligned}2r\,\partial_t\eta_r = &- D_m\left[\partial_y^2\phi_r - 2\rho_r(x)\big|_{x=r}\partial_y^2 r - 4\partial_y\rho_r(x)\big|_{x=r}\partial_y r - 2\partial_x\rho_r(x)\big|_{x=r}(\partial_y r)^2\right]\\ &+ 2r\,(D_c + D_m)\,\partial_y^2\eta_r + 2(Tr_{r_0} - Tr_r) \quad (\eta - \text{inside region})\end{aligned}}. \tag{3.34}$$

Harmonic ansatz. To investigate the stability of the stationary branch, we perform a linear stability analysis of weak, slowly varying modulations of its width. We therefore consider perturbations of the form

$$r(y,t) = r_0 + \varepsilon\tilde{r}(y,t), \quad \varepsilon \ll 1 \tag{3.35}$$

and assume that the modulation varies on length scales much larger than the branch width, so that

$$\partial_y r = \mathcal{O}(\varepsilon), \qquad \partial_y^2 r = \mathcal{O}(\varepsilon). \tag{3.36}$$

Within linear theory it is sufficient to study individual Fourier modes, since any sufficiently small perturbation can be decomposed into a superposition of harmonic modes that evolve independently at linear order. We therefore adopt the sinusoidal ansatz

$$\begin{cases} r(y,t) = r_0 + \epsilon_1(t)\,\sin(qy) \\ \eta_{r(y,t)} = \eta_0 + \epsilon_2(t)\,\sin(qy) \end{cases}, \tag{3.37}$$

where r_0 and η_0 are constants related to the steady state unperturbed branch, $\epsilon_1(t)$ and $\epsilon_2(t)$ are small time-dependent amplitudes, and q is the wavenumber of the perturbation in the y-direction (corresponding to a wavelength $\lambda = 2\pi/q$).

The two perturbation amplitudes are treated as independent variables because the branch width (related to the total mass inside the attachment zone ϕ_r) and the mass redistribution potential obey different dynamical equations and generally evolve on different timescales. While the branch width reflects the slow redistribution of the conserved mass occurring via diffusion, the mass redistribution potential responds on a much faster timescale through the local reaction dynamics. Allowing the two amplitudes to evolve independently therefore provides a self-consistent description of the coupled dynamics. As discussed in Sec. 5, constraining both fields to share a single amplitude leads to a less accurate approximation and fails to capture the full dynamics of the instability.

The remaining quantities are obtained by Taylor expanding around the unperturbed branch half-width $r(y,t) = r_0$:

$$\begin{aligned} Tr_{r(y,t)} &= Tr_{r_0} + \epsilon_1(t)\,\sin(qy)\,\partial_r Tr_r\big|_{r=r_0}, \\ \phi_{r(y,t)} &= \phi_{r_0} + \epsilon_1(t)\,\sin(qy)\,\partial_r \phi_r\big|_{r=r_0}, \\ \rho_{r(y,t)}(x) &= \rho_{r_0}(x) + \epsilon_1(t)\,\sin(qy)\,\partial_r \rho_r(x)\big|_{r=r_0}. \end{aligned} \tag{3.38}$$

where the derivative in ∂_r are taken into the space of stationary solution.

We substitute the harmonic ansatz, Eqs. (3.37) and (3.38), into Eqs. (3.23) and (3.34). Expanding all quantities to first order in the perturbation amplitudes and neglecting higher-order terms yields

$$\left(\partial_r \phi_r\big|_{r=r_0} - 2\rho_{r_0}(x)\big|_{x=r_0}\right)\partial_t \epsilon_1(t) = -2r_0\, D_c\, q^2 \epsilon_2(t) \tag{3.39}$$

and

$$2r_0\,\partial_t \epsilon_2(t) = \left[D_m q^2 \left(\partial_r \phi_r\big|_{r=r_0} - 2\rho_{r_0}(x)\big|_{x=r_0}\right) - 2\partial_r Tr_r\big|_{r=r_0}\right]\epsilon_1(t) - 2r_0\,(D_c + D_m)\,q^2 \epsilon_2(t). \tag{3.40}$$

Notice that the term $\rho_{r_0}(x)|_{x=r_0}$ results from a double Taylor expansion: first expanding the profile $\rho_r(x)$ around the unperturbed branch width $r = r_0$, and then expanding the resulting function around $x = r_0$. The first-order corrections in ϵ_1 can be neglected because $\rho_r(x)|_{x=r}$ always appears multiplied by already first-order perturbation terms. Therefore, only the zeroth-order contribution of this quantity is required in the linear approximation.

Positive constant A. Before analyzing the dispersion relation of the linearized system, it is useful to define

$$A \equiv \partial_r \phi_r\big|_{r=r_0} - 2\rho_{r_0}(x)\big|_{x=r_0}, \tag{3.41}$$

which enters in both Eqs. (3.39) and (3.40). The sign of this quantity will determine the coupling between variations of the branch width and variations of the redistribution potential.

We now show that $A > 0$ for the class of stationary branches considered. To this end, we first rewrite $\partial_r \phi_r$ using the Leibniz rule (Eq. (3.18)):

$$\begin{aligned} \partial_r \phi_r &= \frac{d}{dr}\int_{-r}^{+r} dx\ \rho_r(x) \\ &= \int_{-r}^{+r} dx\ \partial_r \rho_r(x) + \rho_r(x)\big|_{x=r}\partial_r r - \rho_r(x)\big|_{x=-r}\partial_r(-r) \\ &= \int_{-r}^{+r} dx\ \partial_r \rho_r(x) + 2\rho_r(x)\big|_{x=r}, \end{aligned} \tag{3.42}$$

where the symmetry of the branch profile, $\rho_r(x)|_{x=r} = \rho_r(x)|_{x=-r}$, has been used in the last step. Consequently, it follows that $A = \int_{-r_0}^{+r_0} dx\ \partial_{r_0}\rho_{r_0}(x)$ and therefore, the positivity of A is equivalent to requiring

$$\int_{-r_0}^{+r_0} dx\ \partial_{r_0}\rho_{r_0}(x) > 0. \tag{3.43}$$

The physical interpretation of this condition is straightforward. The branch half-width r_0 controls the extension of the attachment region. Increasing r_0 mainly affects the profile close to the interfaces, shifting them outward, while the bulk regions of both attachment and detachment remain approximately unchanged.
Consequently, $\partial_{r_0}\rho_{r_0}(x)$ is expected to be localized around the interfaces $x = \pm r_0$ and to be predominantly positive.

To illustrate this argument, we first consider a simple monotonic analytical profile,

$$\rho_{r_0}(x) = b - c\,\tanh\big(x^2 - r_0^2\big), \tag{3.44}$$

which is not an exact stationary solution but provides a useful qualitative description of a branch profile. In that case,

$$\partial_{r_0}\rho_{r_0}(x) = \frac{2cr_0}{\cosh^2(x^2 - r_0^2)} > 0. \tag{3.45}$$

As illustrated in the left part of Fig. 3.8, variations of r_0 primarily affect the profile in a neighborhood of the interface, while the bulk of both the attachment and detachment regions remains essentially unchanged. Consequently, $\partial_{r_0}\rho_{r_0}(x)$ is positive in a finite region around $x = \pm r_0$, and approximately zero elsewhere. The analytical derivative for a fixed r_0 is shown in the right panel of Fig. 3.8. Since the derivative $\partial_{r_0}\rho_{r_0}(x)$ is positive over the whole domain, Eq. (3.43) is satisfied and consequently $A > 0$.

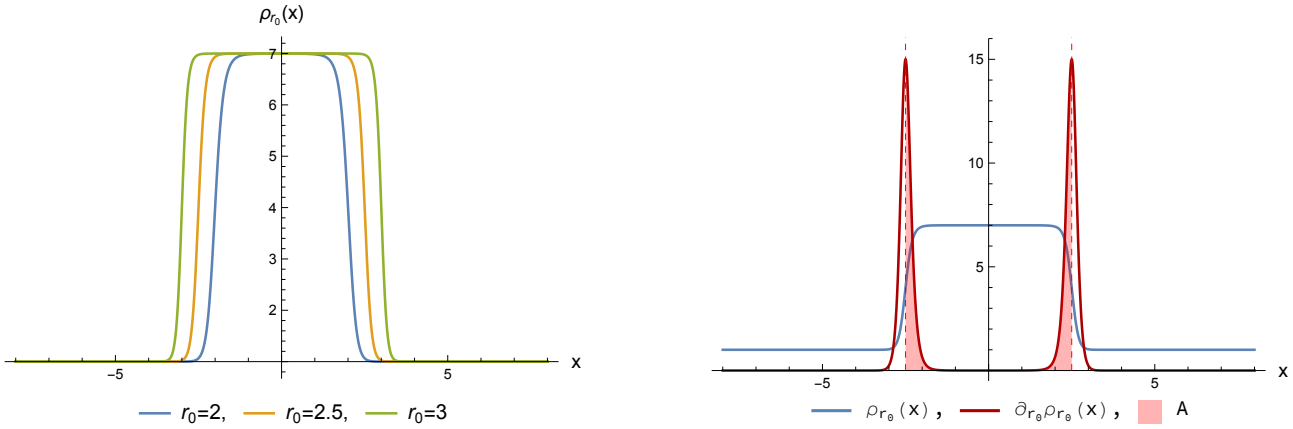

Figure 3.8: Effect of increasing the branch half-width r_0 on a monotonic analytical profile $\rho_{r_0}(x) = b - c\,\tanh\big(x^2 - r_0^2\big)$ for fixed $b = 4$ and $c = 3$ (left). Analytical derivative $\partial_{r_0}\rho_{r_0}(x)$ compared with the density profile (right). Increasing r_0 shifts the interface outward, converting regions near the interface from low to high density, while the bulk of both attachment and detachment zones remains approximately unchanged. As a result, for the monotonic analytical profile, $\partial_{r_0}\rho_{r_0}(x)$ is localized near the interface $x = \pm r_0$ and predominantly positive, leading to a positive A. The geometric interpretation of $A = \int_{-r_0}^{+r_0} dx\,\partial_{r_0}\rho_{r_0}(x)$ is the area under the curve of the derivative's graph, highlighted in red.

However, stationary solutions of the three-component McRD model are generally more complex and do not always display monotonic interfaces. In particular, for some profiles the local density inside the attachment region can slightly decrease when the branch width is increased (some examples in Fig. 3.9). Therefore, $\partial_{r_0}\rho_{r_0}(x)$ can become locally negative, and the previous argument cannot be considered a rigorous proof for arbitrary stationary branches.

Although a fully analytical proof is not available, numerical evidence consistently confirms that the dominant contribution to the integral in Eq. 3.43 arises from the positive regions generated by the displacement of the interfaces, while any negative contributions remain negligible. The reason is that the magnitude of $\partial_{r_0}\rho_{r_0}$ near the interfaces is typically much larger than the small negative variations occurring inside the attachment region. Therefore, all stationary branches investigated satisfy $A > 0$.

To further support this conclusion, Fig. 3.10 reports the numerical values of ϕ_{r_0}, $\rho_{r_0}(x)|_{x=r_0}$, and A computed for different stationary profiles, including both monotonic and non-monotonic solutions. In

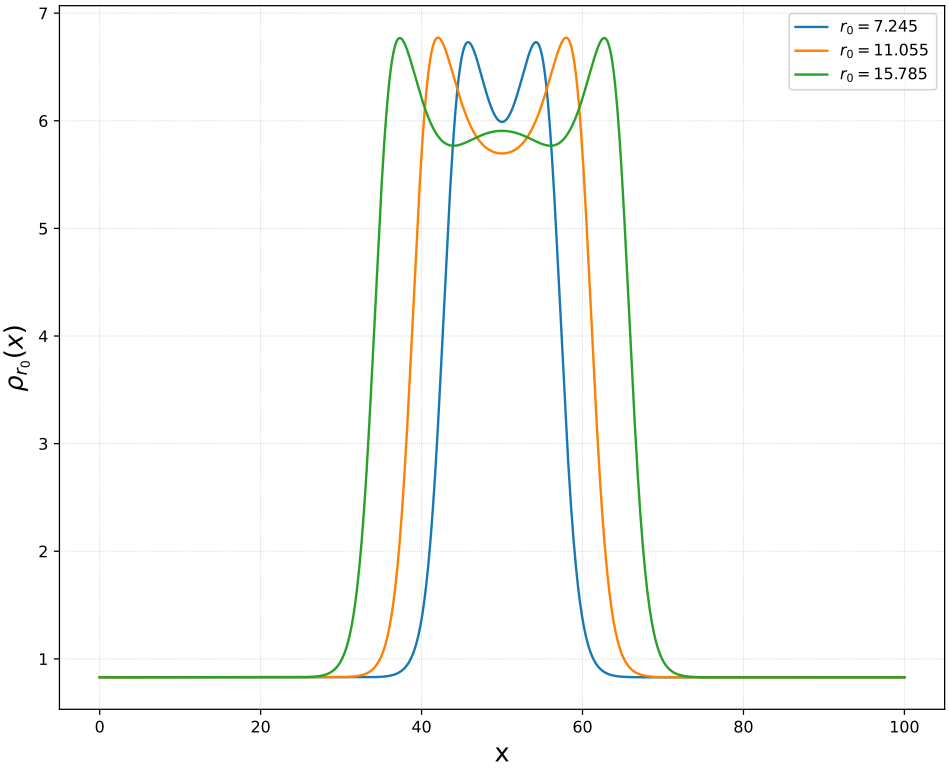

Figure 3.9: Examples of steady state profiles with non-monotonic interfaces for different half-width r_0, obtained from one-dimensional *Mathematica* simulations. In that case, when we increase r_0 the total local density can slightly decrease in some positions in the attachment zone, especially near the "peaks" at the boundaries.

all cases considered, A remains strictly positive. The positivity of A ensures that an increase of branch width corresponds to an increase of the total mass stored in the branch, which determines the sign of the coupling between width perturbations and redistribution potential perturbations.

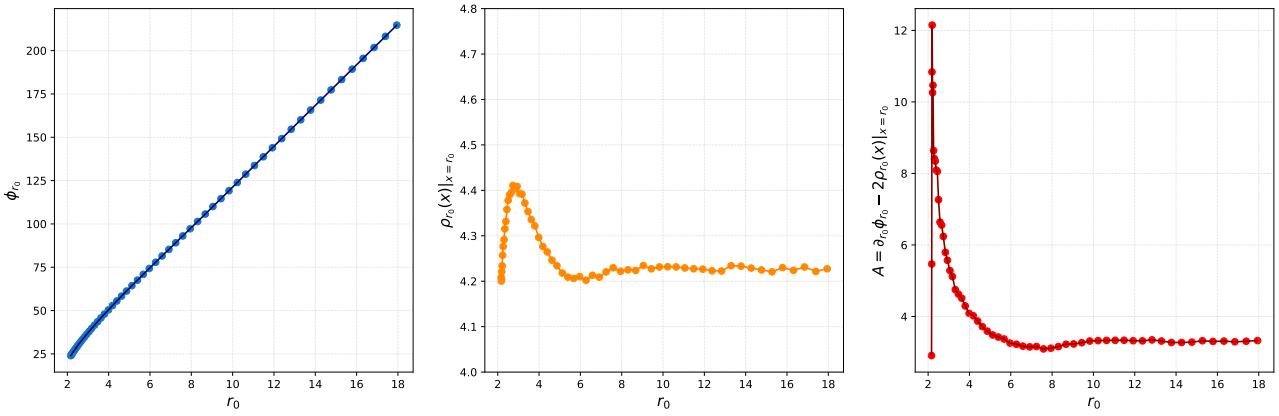

Figure 3.10: Numerical evidence for the positivity of A, obtained from 60 stationary profiles (both monotonic and non-monotonic). **i)** The quantity ϕ_{r_0} increases approximately linearly with the unperturbed branch half-width r_0. For monotonic profiles, this is consistent with the crude estimate $\phi_{r_0} = \int_{-r_0}^{+r_0} dx\, \rho_{r_0}(x) \approx 2r_0\, \rho_{\text{att}}$, corresponding to the area under the attachment plateau. **ii)** The interface value $\rho_{r_0}(x)|_{x=r_0}$ remains approximately constant as r_0 varies. In the monotonic case, it is roughly captured by the estimate of the midpoint between the attachment and detachment plateaus, i.e. $\rho_{r_0}(x)|_{x=r_0} \approx \frac{1}{2}(\rho_{\text{att}} + \rho_{\text{det}})$. **iii)** The resulting quantity $A = \partial_{r_0}\phi_{r_0} - 2\rho_{r_0}(x)|_{x=r_0}$ is strictly positive for all profiles considered. For monotonic interfaces, combining the previous approximations suggests the heuristic estimate $A \approx \rho_{\text{att}} - \rho_{\text{det}} > 0$. Although this approximation is not expected to hold quantitatively for non-monotonic profiles, the numerical results confirm that the positivity of A persists in the general case. Further details on the numerical procedure are provided in the following section.

Dispersion relation. The linearized system defined by Eqs. (3.39) and (3.40) can be written in compact matrix form as

$$\begin{pmatrix} \dot{\epsilon}_1 \\ \dot{\epsilon}_2 \end{pmatrix} = \begin{pmatrix} 0 & -\dfrac{2r_0\, D_c\, q^2}{A} \\ -\dfrac{\partial_r Tr_r\big|_{r=r_0}}{r_0} + \dfrac{D_m q^2 A}{2r_0} & -(D_c + D_m)\, q^2 \end{pmatrix} \begin{pmatrix} \epsilon_1 \\ \epsilon_2 \end{pmatrix}. \tag{3.46}$$

The stability of the unperturbed stationary branch $\rho_{r_0}(x)$ is determined by the eigenvalues of the linear operator appearing in Eq. (3.46). For a 2×2 matrix, the eigenvalues are fully characterized by the trace τ and the determinant δ, which are given by

$$\tau = -(D_c + D_m)\, q^2 < 0, \quad \delta = -\frac{D_c}{A} \left(2\, \partial_r Tr_r\big|_{r=r_0} - D_m\, q^2 A \right) q^2. \tag{3.47}$$

The corresponding eigenvalues are

$$\sigma_{1,2} = \frac{\tau \pm \sqrt{\tau^2 - 4\delta}}{2}. \tag{3.48}$$

Since the trace is negative for all wavenumbers, $\tau < 0$, the sum of the two eigenvalues is necessarily negative. Consequently, the stationary state can be unstable only if one eigenvalue becomes positive while the other remains negative (saddle point). This situation occurs when the determinant is negative, namely

$$\exists q: \quad \delta < 0 \quad \Longrightarrow \quad \exists q: \quad 2\, \partial_r Tr_r\big|_{r=r_0} > D_m\, q^2 A \tag{3.49}$$

Since instability only requires the existence of at least one wavenumber with a positive growth rate, it is sufficient to determine whether the condition $\delta < 0$ can be satisfied for any q. Recalling that $D_m > 0$ and $A > 0$, the right-hand side of Eq. (3.49) is minimized in the long-wavelength limit $q \to 0$. Therefore, if the instability criterion is fulfilled in this limit, there always exists a band of unstable wavenumbers $q \in [0, q_{\max}]$. The onset of the instability is thus determined by the long-wavelength limit, yielding

$$\partial_r Tr\big|_{r=r_0} > 0. \tag{3.50}$$

An important observation is that neither the trace nor the determinant depends explicitly on the steady-state half-width r_0, so it does not directly affect the dispersion relation. Instead, its influence is contained implicitly through the reactive turnover $\partial_r Tr_r|_{r=r_0}$ and the positive constant A which act as the effective control parameters governing the instability.

For the sake of completeness, the two branches of the dispersion relation can be written explicitly as

$$\begin{aligned} \sigma_1(q) &= \frac{-A\,(D_c + D_m)\, q^2 + q \sqrt{A \left(A\, q^2 (D_c - D_m)^2 + 8 D_c\, \partial_r Tr_r\big|_{r=r_0} \right)}}{2A}, \\ \sigma_2(q) &= \frac{-A\,(D_c + D_m)\, q^2 - q \sqrt{A \left(A\, q^2 (D_c - D_m)^2 + 8 D_c\, \partial_r Tr_r\big|_{r=r_0} \right)}}{2A}. \end{aligned} \tag{3.51}$$

In Fig. 3.11 is shown the dispersion relation of the system, namely the dependence of the growth rates $\sigma_{1,2}(q)$ on the wavenumber q. As already specified, the diffusion coefficients are fixed to $D_c = 100$ and $D_m = 1$, while A and $\partial_r Tr_r\big|_{r=r_0}$ are treated as independent control parameters. Strictly speaking, these quantities are not independent, since both are determined by the steady-state half-width r_0. Therefore, not all parameter combinations shown in the figure necessarily correspond to physically realizable stationary states of the model. Nevertheless, treating A and $\partial_r Tr_r|_{r=r_0}$ independently provides a convenient way to explore the mathematical properties of the dispersion relation and to illustrate the generic characteristics of the instability. In particular, this approach clearly highlights that the instability is of Type II, with the unstable modes emerging first in the long-wavelength limit.

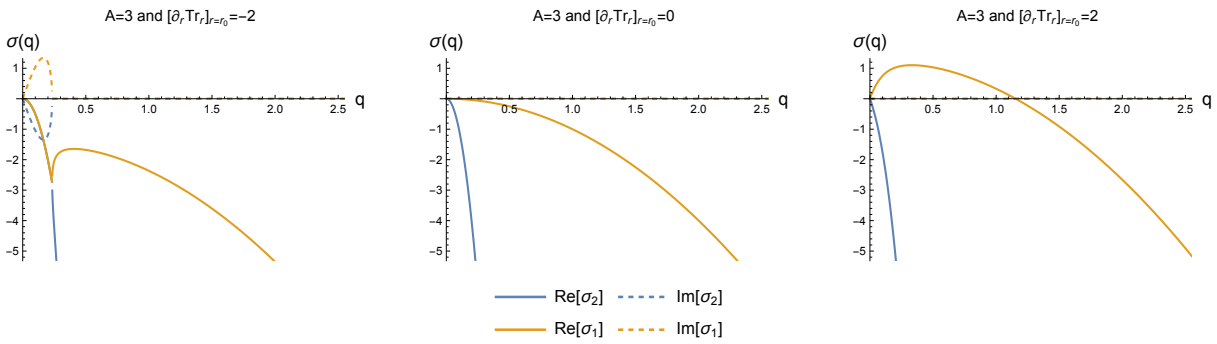

Figure 3.11: Dispersion relation $\sigma_{1,2}(q)$ of the linearized system for different values of the reactive turnover derivative, $\partial_r Tr_r\big|_{r=r_0} = -2,\ 0,\ 2$ (from left to right), at fixed $A = 3$. The solid curves denote the real part of the eigenvalues, which determines the stability of the unperturbed branch $\rho_{r_0}(x)$, while the dashed curves represent the imaginary part, associated with oscillatory dynamics. The critical value $\partial_r Tr_r|r = r_0 = 0$ separates the stable regime from the onset of a long-wavelength instability. Changing $A > 0$ affects the width of the unstable band (i.e. the interval of unstable wavenumbers $[0, q_{max}]$) and the magnitude of the growth rates, while preserving the qualitative nature of the instability, which remains of Type II.

The instability criterion derived in Eq. (3.50) is closely connected to the physical mechanism discussed in Sec. 3.3. A positive value of $\partial_r Tr_r|_{r=r_0}$ implies that locally wider attachment regions exhibit a larger reactive turnover. In other words, a wider attachment region recruits particles from the cytosol at a higher rate. This enhanced attachment locally depletes the cytosolic concentration, thereby reducing the local mass redistribution potential η_r. Physically, one expects the gradients of the reactive turnover and the mass redistribution potential to have opposite signs, meaning

$$\operatorname{sgn}\left(\partial_r Tr_r\big|_{r=r_0}\right) \approx -\operatorname{sgn}\left(\partial_r \eta_r\big|_{r=r_0}\right). \tag{3.52}$$

However, a self-consistent analytical relation between Tr_r and η_r is not yet available within the present framework. An approximate expression relating these quantities is derived in Sec. 5, providing further support for this physical interpretation.

Chapter 4

Numerical validation

4.1 Semi-analytical calculus

Once we obtained the one-dimensional stationary concentration profiles $m_{r0}(x)$, $c_{a\,r0}(x)$, and $c_{i\,r0}(x)$ as described in Sec. 3.1 we can evaluate all the relevant quantities for the theoretical analysis starting from

$$\begin{aligned} R_{r_0}(x) &= \left(1 - \frac{D_m}{D_c}\right)\left[(\gamma_1 + \gamma_2 m_{r_0}^2(x))\, c_{a\,r_0}(x) - \alpha_0\, m_{r_0}(x)\right], \\ \eta_{r_0} &= \frac{D_m}{D_c}\, m_{r_0}(x) + c_{a\,r_0}(x) + c_{i\,r_0}(x), \\ Tr_{r_0} &= \frac{1}{2}\int_{-r_0}^{+r_0} dx\; R_{r_0}(x). \end{aligned} \tag{4.1}$$

The reactive turnover Tr_{r_0} and the mass redistribution potential η_{r_0}, which are constants for a given unperturbed steady-state profile $\rho_{r_0}(x)$, are shown as functions of r_0 in Fig. 4.1.

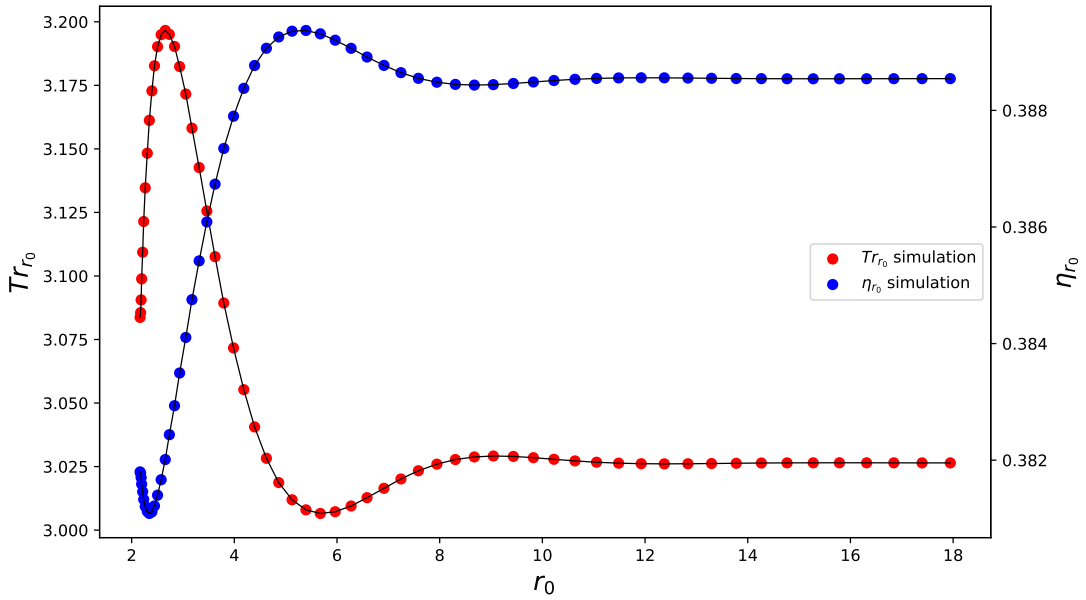

Figure 4.1: Numerically evaluated Tr_{r_0} and η_{r_0} as function of the unperturbed branch half-width r_0. These quantities provide the input for the semi-analytic linear stability analysis developed in the previous sections. Notice that the reactive turnover and the mass redistribution potential have approximately opposite monotonicity, as explained in Eq. (3.52).

Since the most interesting branch behavior occurs for small values of r_0, the sampling of the parameter a, which controls the total mass of the system and consequently the unperturbed half-width r_0, is

chosen to be non-uniform in order to achieve higher resolution in this regime. Moreover, the resulting values of r_0 are not a linear function of a, so the sampled points are therefore not equally spaced.

For this reason, numerical derivatives are evaluated using the `numpy` function `np.gradient`, which implements finite differences adapted to non-uniform grids. For a generic function $f(r)$ sampled at points r_i, the derivative at r_i is approximated as

$$\left.\frac{df}{dr}\right|_{r=r_i} \approx \frac{(r_i - r_{i-1})^2(f_{i+1} - f_i) + (r_{i+1} - r_i)^2(f_i - f_{i-1})}{(r_{i+1} - r_i)(r_i - r_{i-1})(r_{i+1} - r_{i-1})}, \tag{4.2}$$

which reduces to the standard centered finite-difference scheme when the grid spacing is uniform.

At this point, we can determine the dispersion relations of the system as a function of the wavenumber q for all the unperturbed stationary profiles. For example, Fig. 4.2 shows the dispersion relations for the six stationary profiles displayed in Fig. 3.2.

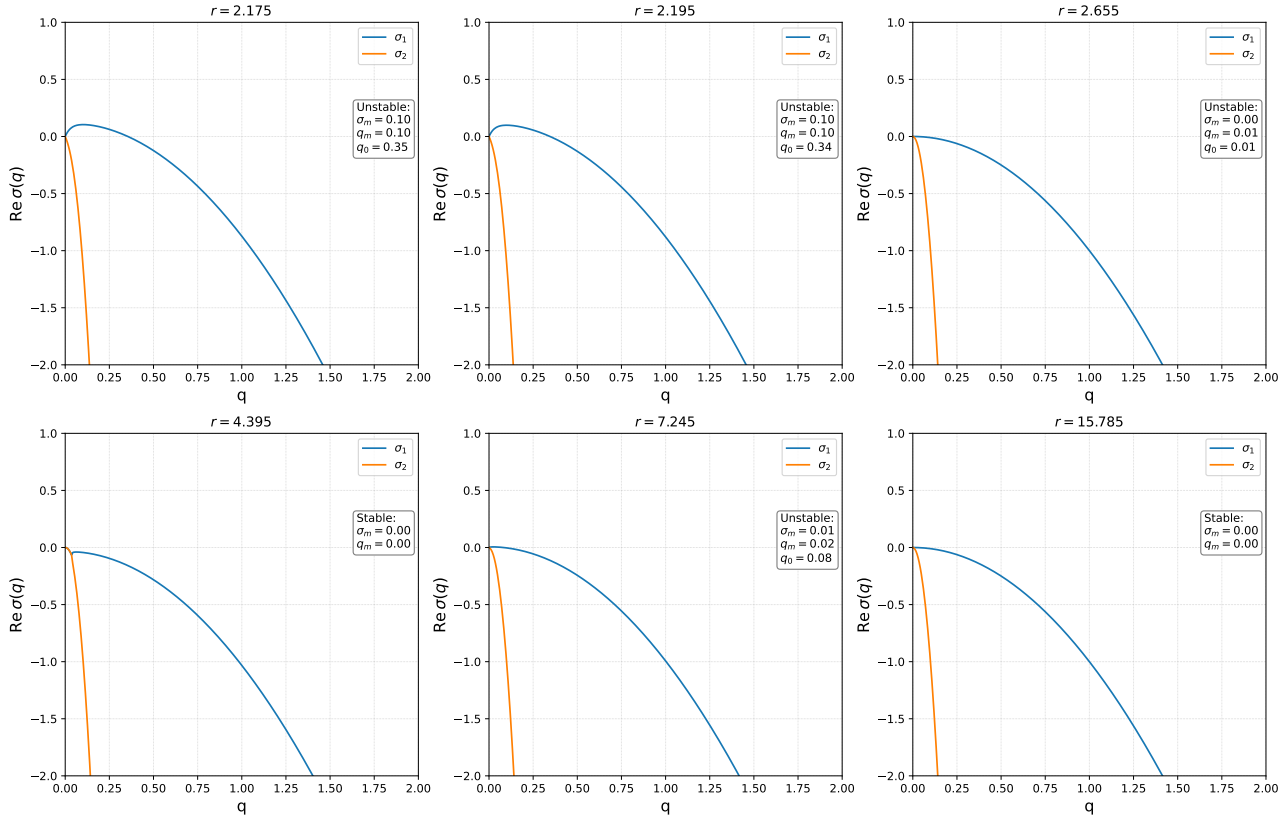

Figure 4.2: Real part of the growth rates of the system (Eq. (3.51)) as a function of the wavenumber q. Only the real part is shown, since complex-conjugate eigenvalue pairs can occur only when their real part is negative, corresponding to stable modes. Unlike Fig. 3.11, where $\partial_r Tr_r\big|_{r=r_0}$ and A were treated as free, independent parameters, here both quantities are evaluated numerically from the one-dimensional stationary profiles $\rho_{r_0}(x)$, such that each curve corresponds to a physical growth rate associated with the branch of half-width r_0.

4.2 Simulations

All that remains is to test the semi-analytical predictions using two-dimensional simulations performed in *COMSOL Multiphysics*.

We solve the full time-dependent three-component system for the fields $m(x, y, t)$, $c_a(x, y, t)$, $c_i(x, y, t)$ on a square domain of side $L = 100$, the same domain size used for the one-dimensional stationary profiles, with no-flux boundary conditions on all four sides. All kinetic and transport parameters are fixed at the values used throughout this thesis, $D_c = 100$, $D_m = 1$, $\gamma_1 = 1$, $\gamma_2 = 1$, $\alpha_0 = 1$, $\lambda = 35$; the only parameter varied across the simulations is a, which sets the total mass $\bar{\rho}$ and, correspondingly, the half-width r_0 of the relaxed stationary branch.

The system is implemented in *COMSOL Multiphysics* using the *General Form PDE* interface (*Mathematics module*), with the three fields as dependent variables $\mathbf{u} = [m, c_a, c_i]^T$. In the general form

$$e_a\, \partial_t^2 \mathbf{u} + d_a\, \partial_t \mathbf{u} + \nabla \cdot \mathbf{\Gamma} = \mathbf{f}, \tag{4.3}$$

the mass coefficient e_a is set to zero, since the model contains no second-order time derivatives; the damping coefficient d_a is set to the identity, recovering the first-order time derivative $\partial_t \mathbf{u}$ of each field; the diffusive terms are recovered through the conservative flux $\mathbf{\Gamma} = -D\nabla\mathbf{u}$, with $D = \mathrm{diag}(D_m, D_c, D_c)$, so that $\nabla \cdot \mathbf{\Gamma} = -D\nabla^2\mathbf{u}$; and the reaction terms enter through the source term $\mathbf{f} = [R_1,\, R_2,\, -R_1 - R_2]^T$. The no-flux condition on all four sides of the domain is directly enforced by requiring that $\mathbf{\Gamma} \cdot \mathbf{n} = 0$.

The problem is solved with a *Time Dependent Study*, requesting solution output at exponentially spaced times, $t = 10^k$ for $k = 0, 0.5, 1, \ldots, 6$. This choice allows a single simulation to resolve both the fast initial relaxation toward the stationary branch profile and the much slower pearling dynamics that follows, without oversampling the early, fast transient.

The domain is discretized with *COMSOL* default free triangular (*Delaunay*) mesh. The element size is chosen to be sufficient fine relative to the typical width of the branch interfaces to properly resolve the density gradients across the transition region. Crucially, this mesh geometry serves a physical purpose. Since the initial condition (introduced below) is exactly invariant under translations along y, nothing in the continuum problem breaks this symmetry, and the pearling instability can only develop from some seed of transverse noise. The triangular mesh breaks this symmetry explicitly, then the instability grows spontaneously from this numerical noise without requiring explicit perturbations. A structured, translationally invariant mesh (e.g. a regular square grid), by contrast, preserves the symmetry of the initial condition to much higher precision and correspondingly suppresses, or considerably delays, the onset of pearling instability.

In principle, the initial condition for the two-dimensional simulation should be given by the extrusion of the stationary one-dimensional profile along the y-direction. Indeed, initializing the system with an analytical guess profile $\rho_a(x, y)$ that differs from the stationary solution may introduce additional dynamics associated with the deviation $\delta\rho(x, y) = \rho_a(x, y) - \rho_{r_0}(x, y)$, which could potentially change the onset of the pearling instability.
However, as observed in Figs. 4.3 and 4.4, the dynamics exhibits a clear separation of time scales. The relaxation from the initial guess profile toward the stationary branch state occurs rapidly, whereas the pearling instability eventually develops on much larger time scale. Consequently, the system first converges close to the stationary profile before any significant transverse instability emerges. This observation justifies the use of the analytical guess profile (an extrusion of the one-dimensional guess from Eq. (3.5)) as the initial condition in the two-dimensional simulation.

Besides being justified by the time-scale separation, this approach greatly simplifies the implementation of the two-dimensional simulations, since it removes the need to generate or import an extruded stationary profile for each parameter set. As a result, the setup of large parameter sweeps becomes significantly more straightforward.

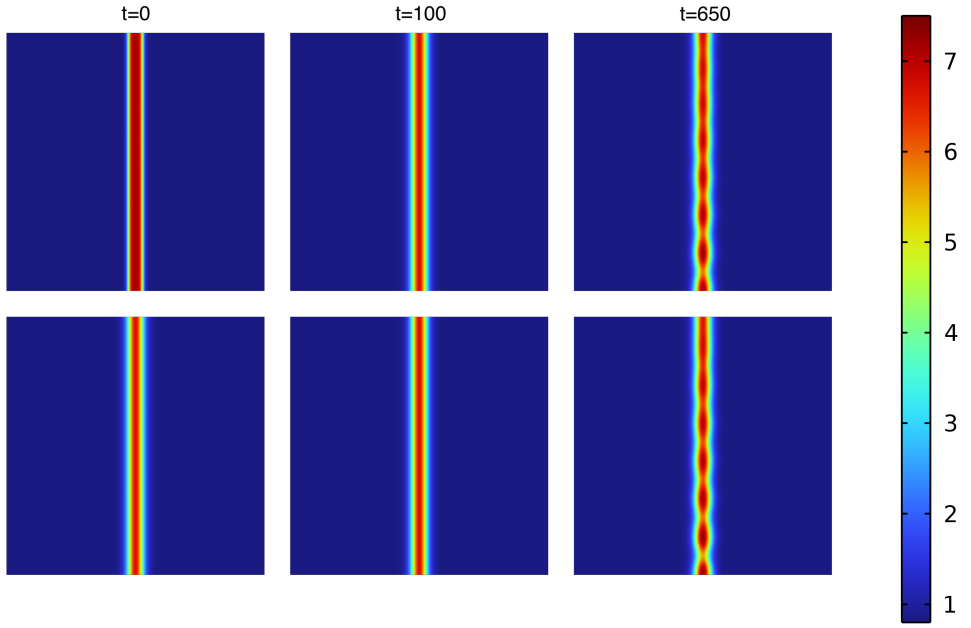

Figure 4.3: Comparison between simulations initialized with the analytical guess profile $\rho_a(x, y) = 4 - 3.2 \tanh(|x - L/2| - a)$ (upper row) and the extruded stationary profile (bottom row). In both cases $a = 2.793$, corresponding to a branch width for which $\partial_r T r_r\big|_{r=r_0}$ is positive and relatively large, resulting in one of the fastest instability growth considered. We can observe that at initial time ($t = 0$) the total densities are different, subsequently the guess profile converge fast to the steady branch state ($t = 100$) and finally they begin to develop instability in a similar manner and on comparable time scales ($t = 650$). Thus the initial relaxation does not significantly affect the instability dynamics.

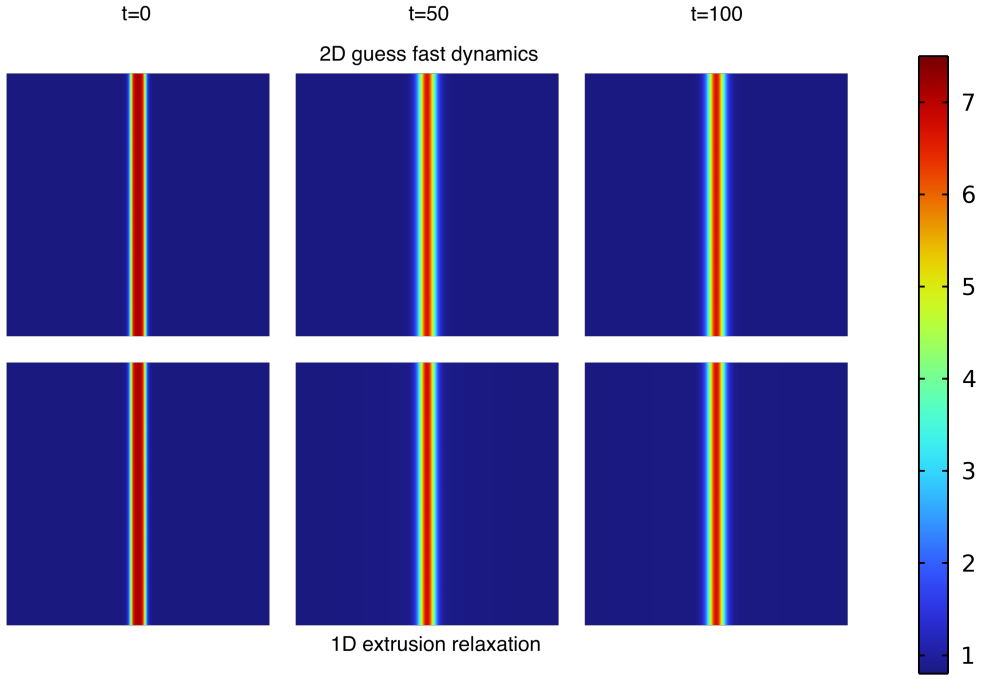

Figure 4.4: Comparison between the early-time evolution of the two-dimensional simulation initialized with the analytical guess profile (top row) and the relaxation dynamics of the corresponding one-dimensional simulation, extruded into 2D simply to facilitate comparison (bottom row). The qualitative agreement between the two evolutions indicates that, at short time scales, mass redistribution occurs predominantly along the x-direction. This confirms that the early dynamics of the two-dimensional system is essentially a relaxation toward the stationary branch profile, supporting the use of the analytical guess profile as an initial condition for the *COMSOL* simulations.

To assess the predictive power of the reactive turnover criterion, we present a set of representative two-dimensional *COMSOL* simulations spanning the different dynamical regimes observed in the system. For each case, four snapshots are shown corresponding to: **i)** the initial condition, **ii)** relaxation toward the stationary branch solution, **iii)** onset of the instability, and **iv)** the long-time dynamics. The purpose of these examples is not to characterize the late-stage evolution in detail, but rather to compare the observed onset of instability with the theoretical prediction based on the sign of $\partial_r Tr_r\big|_{r=r_0}$. Videos of the full time evolution of the simulations discussed in this section, beyond the four snapshots shown here, are available at the following YouTube-link.

First example is shown in Fig. 4.5, corresponding to a branch half-width r_0 located in the first region where $\partial_r Tr|_{r=r_0} > 0$ and the slope of the reactive turnover is relatively large. In this parameter regime, the maximum theoretical growth rate across the unstable band reaches higher values than in any other regime, leading to a rapid development of the pearling instability following the initial relaxation toward the stationary state. The branch first exhibits periodic transverse modulations and subsequently breaks into disconnected droplets. The later evolution is governed by droplet dynamics, and one can observe different behaviors such as spatial redistribution of dots, coarsening dynamics (Ostwald ripening), or mass redistribution and coexistence between dots of different sizes. Our perturbative theory, however, does not aim to describe these phenomena, but rather to predict the onset of pearling.

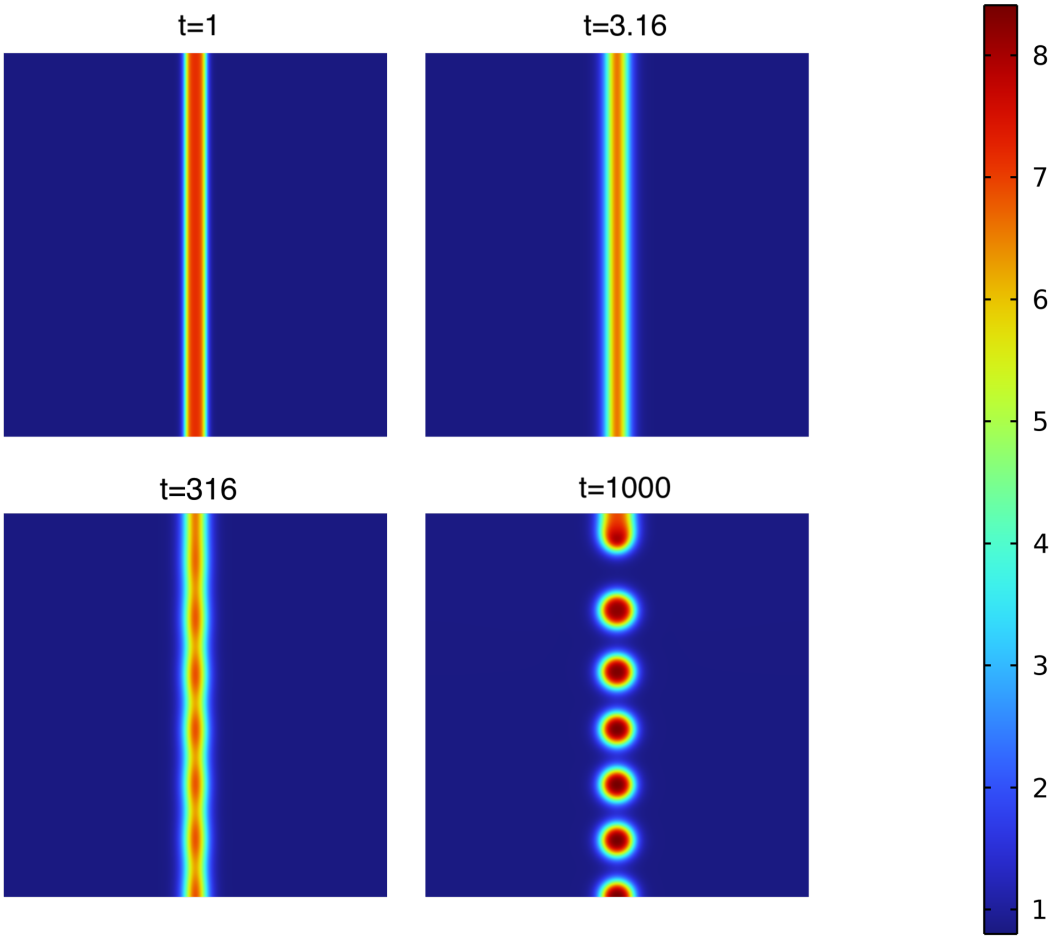

Figure 4.5: Example of rapid pearling instability for monotonic branch profile. The initial condition is given by $\rho_a(x) = 4 - 3.2\,\tanh(|x - L_x/2| - a)$, with $a = 2.683$, corresponding to a total mass $\bar{\rho} = 1.1437$. After a short relaxation toward the stationary branch solution ($r_0 = 2.305$), the branch develops transverse modulations which rapidly grow into a pearling instability. The instability is already visible at $t = 316$ and leads to the formation of disconnected droplets by $t \sim 10^3$.
The subsequent droplet dynamics lie beyond the scope of the present perturbative theory.

Figure 4.6 illustrates a different situation in which $\partial_r Tr|_{r=r_0}$ remains positive but its magnitude is considerably smaller. Importantly, this unstable region represents a second instability window, preceded at smaller branch half-widths r_0 by a stable domain where $\partial_r Tr|_{r=r_0} < 0$. This happens for large enough width for which the stationary branch usually presents non-monotonic interfaces. Consistent with theoretical predictions, the pearling instability still occurs, but on a much longer timescale due to the significantly reduced growth rate. The initial ripple formation is correctly predicted by the theory. However, as the branch pinches and develops regions of reduced width, these portions may locally enter the stable monotonic branch regime. Instability growth is thereby arrested before the branch can fully break up into isolated droplets, and the resulting configuration is a chain of coexisting branch segments and bubble-like structures. The subsequent evolution is governed by the interaction between these branches and dots: a slow coarsening process (Ostwald ripening) redistributes mass from smaller to larger dots, and, at very long times, the local mass accumulation triggers a distinct plateau-to-branch instability, known as the finger instability, through which new branch segments nucleate from the enlarged dots. This whole late-stage sequence lies outside the assumptions of the present perturbative description, which is limited to predicting the initial onset of the modulation.

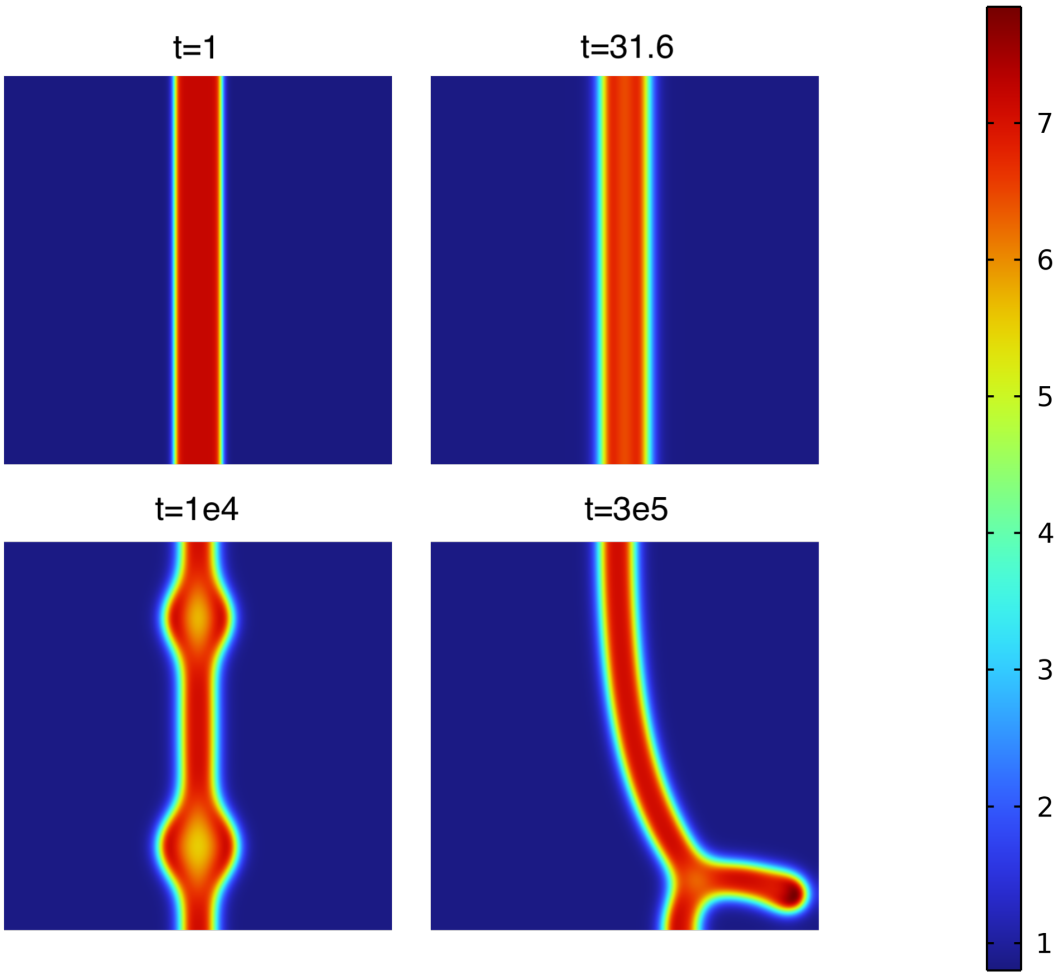

Figure 4.6: Example of weak pearling instability for non-monotonic interfaces profile. The initial guess profile corresponds to $a = 6.089$ ($\bar{\rho} = 1.5794$). In short time the profile relaxes toward a stationary non-monotonic branch with half-width $r_0 = 5.965$. Consistent with the small positive value of $\partial_r Tr_r|_{r=r_0}$, the instability develops only at very long times ($t \sim 10^4$) and after the first redistribution of mass a new stable monotonic branch appears in the middle between two bubbles. At this stage our perturbative theory is no longer able to describe the dynamics. In the final time-shot $t = 3 \times 10^5$, we observe an apparently unusual configuration consisting of three intersecting branches. The widths of these branches are smaller than the initial one, suggesting that they are likely in the linearly stable regime. The intersection appears to originate from a plateau-to-branch instability developing in the bubble regions.

Finally, Fig. 4.7 presents a case for which $\partial_r Tr_r|_{r=r_0} < 0$. According to the reactive-turnover criterion, no pearling instability is expected, and indeed the branch does not develop the symmetric transverse modulations characteristic of pearling. Nevertheless, the branch is not stable because undergoes a different instability characterized by a gradual bending of the interface and the formation of an S-shaped configuration, which we refer as bending instability. This behavior lies outside the scope of the present analysis, which treats the branch as locally straight and does not include its curvature as a dynamical degree of freedom: only the response of the mass redistribution potential to a variation of the branch width has been considered, while a description of the bending instability would instead require characterizing the response of η to a variation of the local radius of curvature of the branch. A dedicated perturbative treatment along these lines would be needed to capture this regime.

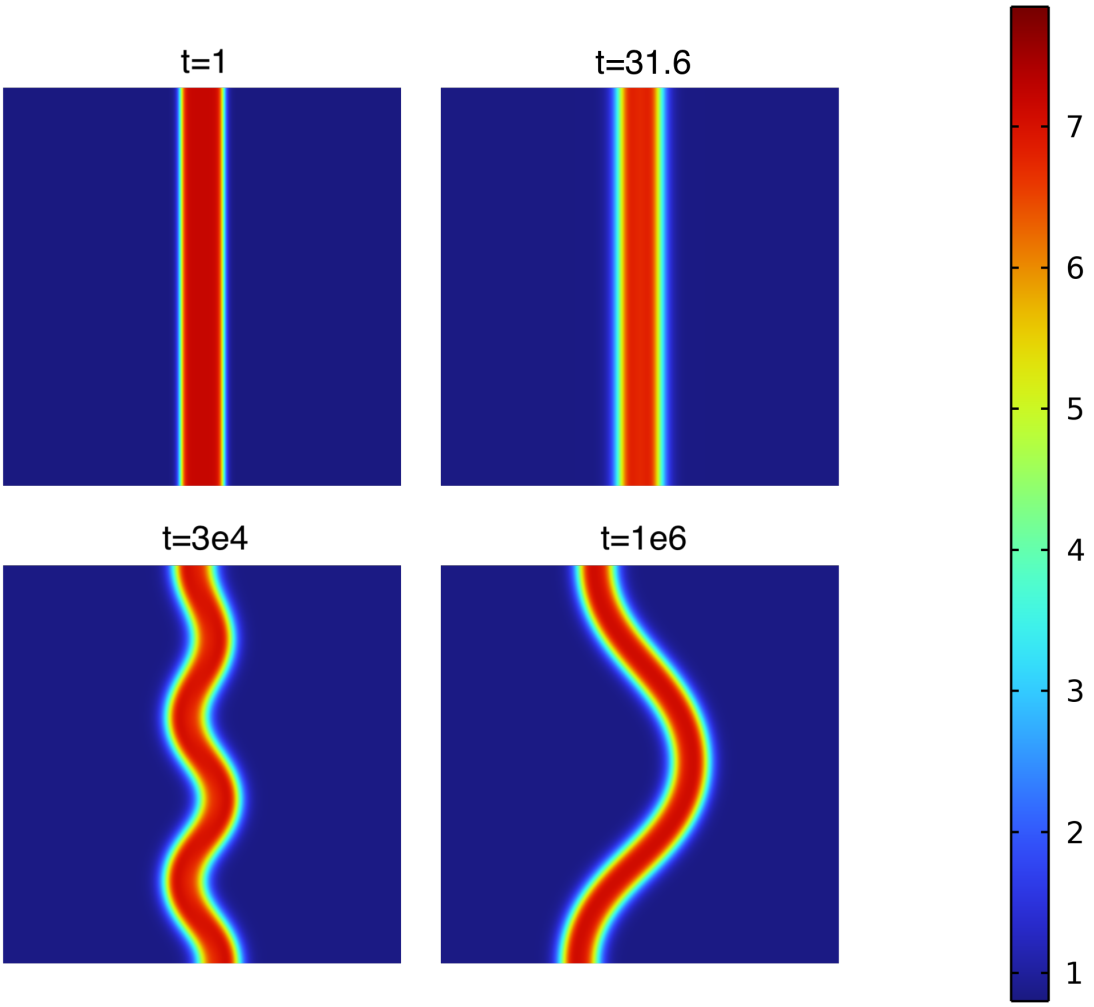

Figure 4.7: Example of bending instability. The initial guess profile corresponds to $a = 5.428$ ($\bar{\rho} = 1.4948$), which relaxes to a stationary branch with half-width $r_0 = 5.125$. This parameter regime is located near the global minimum of the reactive turnover (see Fig. 4.1), where the derivative $\partial_r Tr_r|_{r=r_0}$ is negative; therefore no pearling instability is expected. Indeed, the branch does not develop the symmetric transverse modulations characteristic of pearling. Instead, an antisymmetric deformation gradually bends the branch into an S-shaped configuration. Since the present perturbative analysis neglects curvature effects, this instability cannot be captured by the theory and likely originates from a distinct curvature-dependent mechanism.

For all branches satisfying $\partial_r Tr_r|_{r=r_0} < 0$ away from the curvature-driven regime discussed above, the profiles are, as expected, linearly stable. The dynamics consists solely of a rapid initial relaxation toward the stationary state, with no appreciable evolution over the simulated time window. These stable cases are therefore omitted for brevity.

The comparison between simulations and theory is summarized in Fig. 4.8. Branches undergoing pearling are consistently found in regions where $\partial_r Tr_r|_{r=r_0} > 0$, while branches remaining stable correspond to $\partial_r Tr_r|_{r=r_0} < 0$. The sign of $\partial_r Tr_r|_{r=r_0}$ correctly predicts the onset of the pearling instability across the explored parameter range, with two exceptions. First, small discrepancies appear in the immediate vicinity of the transition points, i.e. the maxima and minima of Tr_r where $\partial_r Tr_r|_{r=r_0}$ changes sign: there, corrections of order $\mathcal{O}(\epsilon^2)$, neglected by the present linear theory, may become non-negligible. Second, near the global minimum of Tr_{r_0} a bending instability develops despite the absence of pearling.

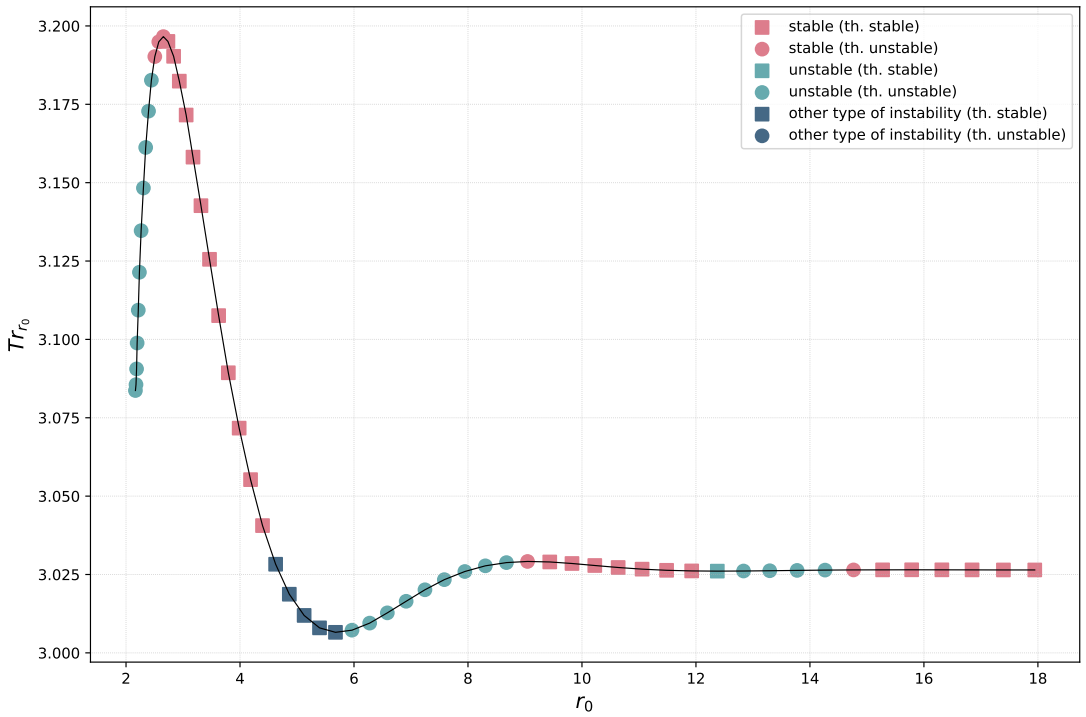

Figure 4.8: Reactive turnover Tr_{r_0} as a function of the numerical branch half-width r_0. Numerical points are shown as circles when the slope is positive and squares when the slope is negative. Colors correspond to two-dimensional *COMSOL* simulations: unstable branches undergoing pearling are shown in pink, stable branches in green, and bending instability in blue.

4.3 Quantitative test

The previous section showed that the linear stability analysis correctly predicts the onset of the pearling instability. A more stringent test, however, is whether the dispersion relation also provides quantitative information connected to measurable properties of the system dynamics. To this end, we compare four independent numerical observables against the corresponding theoretical predictions extracted from the dispersion relation. Two of them probe the temporal development of the instability through the maximum growth rate, while the remaining two characterize its spatial structure through the critical and dominant wavelengths.

Three quantities can be directly extracted from the theoretical unstable branch of the dispersion relation, as illustrated in Fig. 4.9 for a representative case:

1. The maximum growth rate $\sigma_{\max} = \max_q \sigma_1(q)$, which represents the largest eigenvalue on the unstable branch. This quantity sets the e-folding time of the instability,

$$\tau_{\text{th}} = \frac{1}{\sigma_{\max}}, \tag{4.4}$$

providing a characteristic timescale for the exponential growth of the dominant mode.

2. The most unstable mode $q_{\max} = \operatorname{argmax}_q \sigma_1(q)$, corresponding to the mode with the maximum growth rate. Being the first mode to become unstable, it sets the spacing between neighboring pearls immediately after the onset of the instability,

$$\lambda_{\text{th}} = \frac{2\pi}{q_{\max}}. \tag{4.5}$$

3. The critical mode q_0, defined by $\sigma_1(q_0) = 0$. Instability can only occur if the system can accommodate perturbations with wavenumber smaller than q_0. Consequently, q_0 determines the critical system height

$$h_{\text{th}} = \frac{2\pi}{q_0}, \tag{4.6}$$

below which pearling cannot be observed, since the domain is too small to support the unstable long-wavelength perturbations.

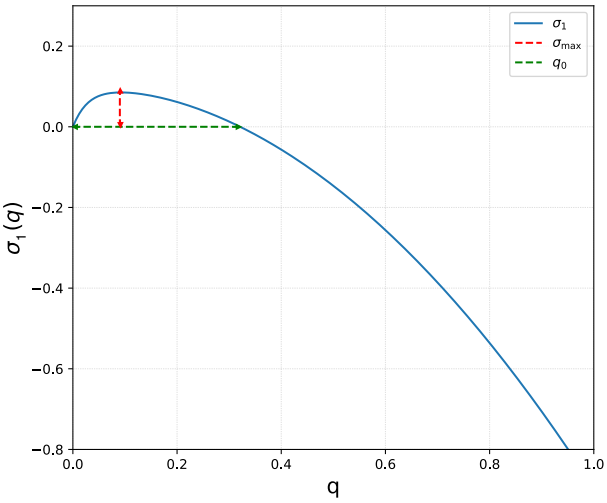

Figure 4.9: Unstable branch of the dispersion relation $\sigma_1(q)$ for the stationary branch of half-width $r_0 = 2.235$. The red arrow marks the maximum growth rate $\sigma_{\max}$, attained at the wavenumber $q_{\max}$; the green arrow marks the critical mode q_0, where the curve crosses zero. These three quantities, read directly off the curve, are the theoretical predictions tested against simulations in the remainder of this section.

The first two tests rely on a common onset criterion. The branch width is measured along $N_y = 50$ horizontal slices, homogeneously distributed across the numerical domain L_y. For each simulation snapshot, the inflection points of the total local mass profile $\rho(x, y)$ are detected on every slice, providing a local estimate of the branch width, $w_i \equiv 2r(y_i, t, L_y)$. Depending on the test under consideration, this spatial evaluation is performed either as a function of time t for a fixed system height L_y, yielding $w_i(t)$, or as a function of system height L_y at a fixed time t, yielding $w_i(L_y)$.
The corrugation of the branch is then quantified by the standard deviation of these widths across slices,

$$\sigma_w = \sqrt{\sum_{i=1}^{N_y} \frac{(w_i - \langle w \rangle)^2}{N_y - 1}}, \tag{4.7}$$

where $\sigma_w = \sigma(t)$ or $\sigma_w(L_y)$ depending on the variable parameter. To eliminate the dependence on the absolute branch size, the standard deviation is normalized by the stationary width $2r_0$ obtained from the corresponding one-dimensional steady-state solution.
The onset of pearling is then defined as the earliest configuration, in either time or system height, at which this normalized standard deviation exceeds a 10% threshold:

$$\tau_{\text{sim}} \ \ (\text{or } h_{\text{sim}}) = \min \left\{ t \ \ (\text{or } L_y) \ : \ \frac{\sigma_w(t) \ \ (\text{or } \sigma_w(L_y))}{2r_0} > 0.1 \right\}. \tag{4.8}$$

Since both time and system height are sampled on discrete grids, the resulting measurements carry a finite-resolution uncertainty. As a first-order estimate, the uncertainties on τ_{sim} and h_{sim} are taken to be the corresponding sampling intervals, Δt and Δh.

The first, and most direct, test consists of measuring the earliest time at which the criterion of Eq. (4.8) is satisfied, in a domain sufficiently large that the instability is not suppressed by finite-size effects. This defines the numerical characteristic time τ_{sim}, to be compared with the theoretical prediction $\tau_{\mathrm{th}} = 1/\sigma_{\max}$ of Eq. (4.4), as shown in Fig. 4.10.

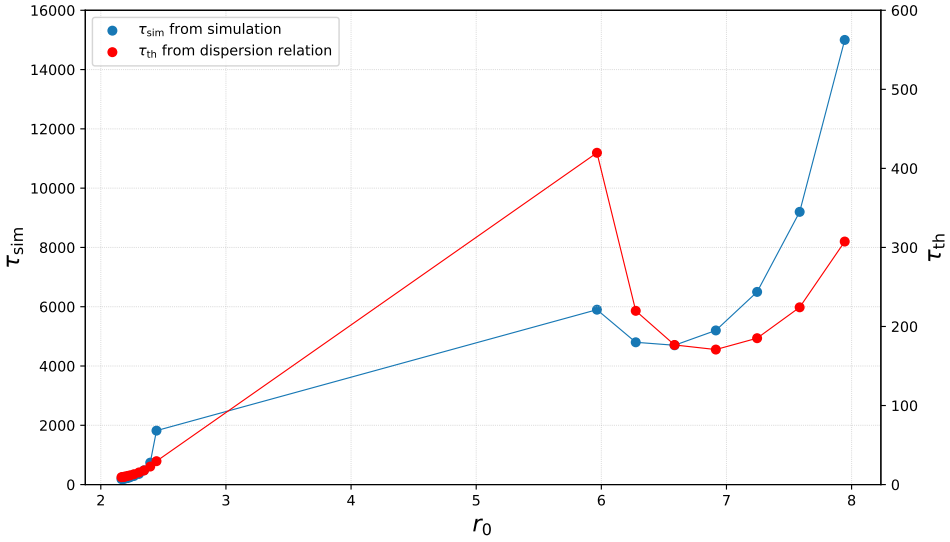

Figure 4.10: Numerical onset time τ_{sim} (blue), obtained from the criterion in Eq. (4.8), compared with the theoretical e-folding time $\tau_{\mathrm{th}} = 1/\sigma_{\max}$, as a function of the stationary branch half-width r_0. The theoretical and numerical curves differ by more than an order of magnitude; nevertheless, the two curves exhibit the same qualitative behavior as a function of r_0. Because the 10% threshold requires a substantial amount of corrugation to accumulate before being triggered, this test is expected to systematically overestimate the theoretical e-folding time.

The same onset criterion can be used also for critical height: for a fixed, sufficiently large observation time, it identifies the minimum system height at which pearling develops, i.e. the numerical critical height h_{sim}, to be compared with the theoretical prediction $h_{\mathrm{th}} = 2\pi/q_0$ of Eq. (4.6). Results are shown in Fig. 4.12. Figure 4.11 illustrates this dependence qualitatively: simulations sharing the same stationary branch profile (in practice, it is sufficient to initialize the same branch-like profile, rather than the full extruded one-dimensional solution, as discussed in Sec. 4.2) but performed in domains of different height exhibit qualitatively different long-time behavior, consistent with the existence of a critical height below which pearling is suppressed.

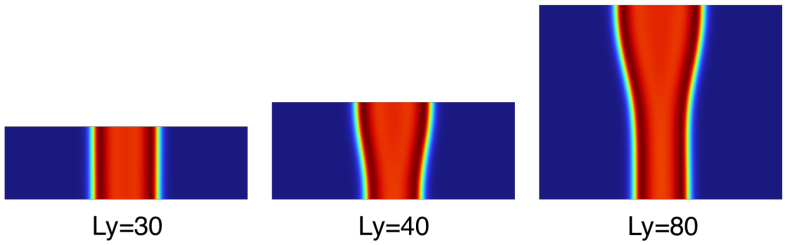

Figure 4.11: Dependence of the pearling instability on the system height L_y, for the stationary branch obtained from initial guess $a = 11.836$ ($\bar{\rho} = 2.315$), which relaxes to half-width $r_0 = 13.295$. For this branch, the dispersion relation predicts a critical wavenumber $q_0 = 6.01 \times 10^{-3}$ and a maximum growth rate $\sigma_{\max} = 8.37 \times 10^{-5}$. At sufficiently large time ($t = 5 \times 10^6 \gg 1/\sigma_{\max}$), the branch remains stable when $L_y < h_{\text{sim}}$ (left, $L_y = 30$), whereas pearling develops for larger system heights capable of supporting unstable long-wavelength perturbations (centered and right pictures, $L_y = 40$ and $L_y = 80$ respectively).

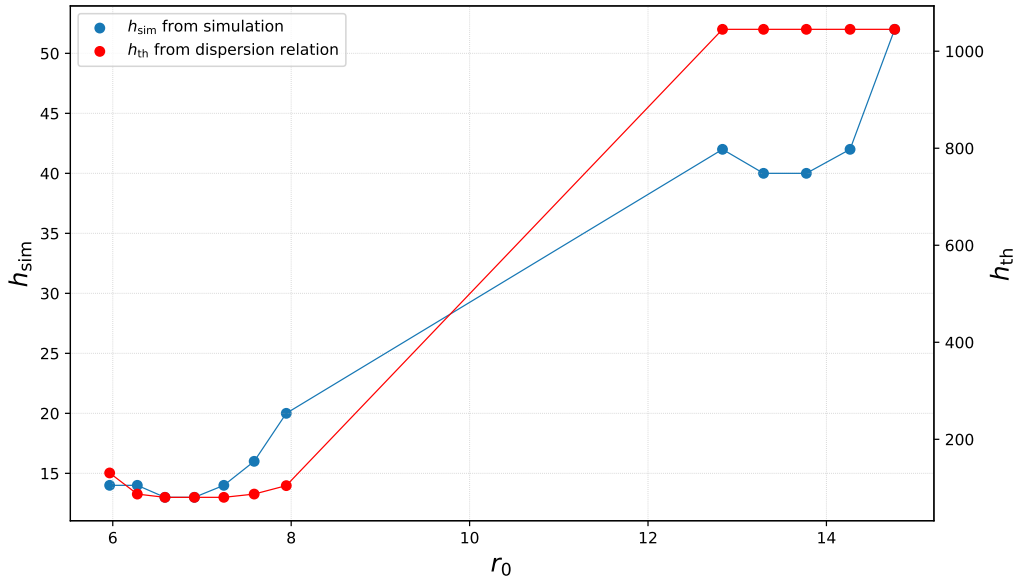

Figure 4.12: Numerical critical height h_{sim} (blue), obtained from the onset criterion of Eq. (4.8), compared with the theoretical prediction $h_{\text{th}} = 2\pi/q_0$, as a function of the stationary branch half-width r_0. The numerical values systematically underestimate the theoretical prediction, again by more than an order of magnitude, although the qualitative trend is preserved. This test is the least reliable of the four, since near the critical height the observed corrugation may correspond to a single peak–valley pair rather than to a genuine periodic pearling pattern.

A third test targets the characteristic wavelength directly. Using a finer spatial grid ($N_y = 150$), evaluated at the characteristic time τ_{sim} measured above, we again extract the branch width along each slice and locate its local maxima (peaks). The numerical wavelength λ_{sim} is estimated as the average distance between adjacent maxima of the branch width as explained in Fig. 4.13. The comparison with theoretical prediction $\lambda_{\text{th}} = 2\pi/q_{\max}$ of Eq. (4.5) is shown in Fig. 4.14.

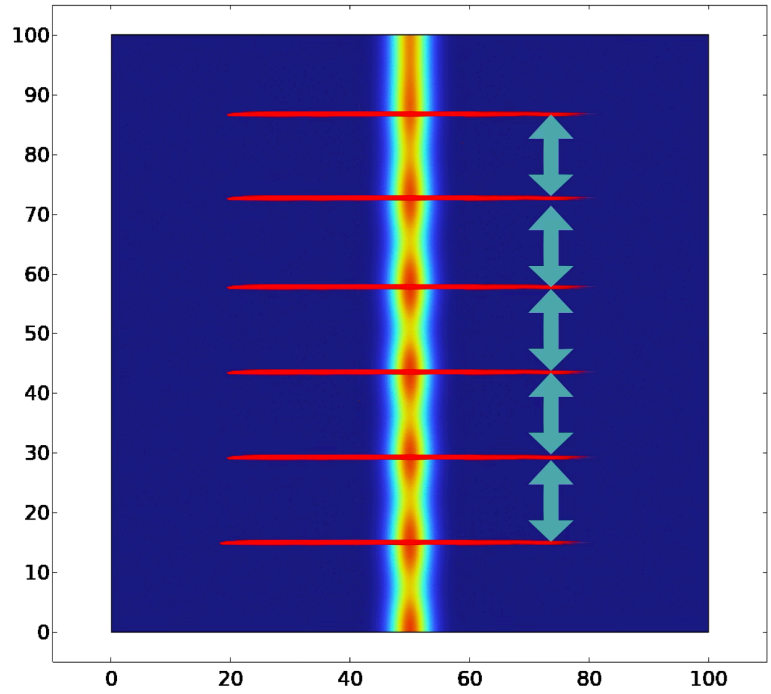

Figure 4.13: Onset of pearling instability for the stationary branch obtained from initial guess $a = 2.683$ ($\bar{\rho} = 1.1437$), which relaxes to half-width $r_0 = 2.305$. The numerical wavelength λ_{sim} is estimated as the average distance between adjacent maxima which is highlighted with the green arrows.

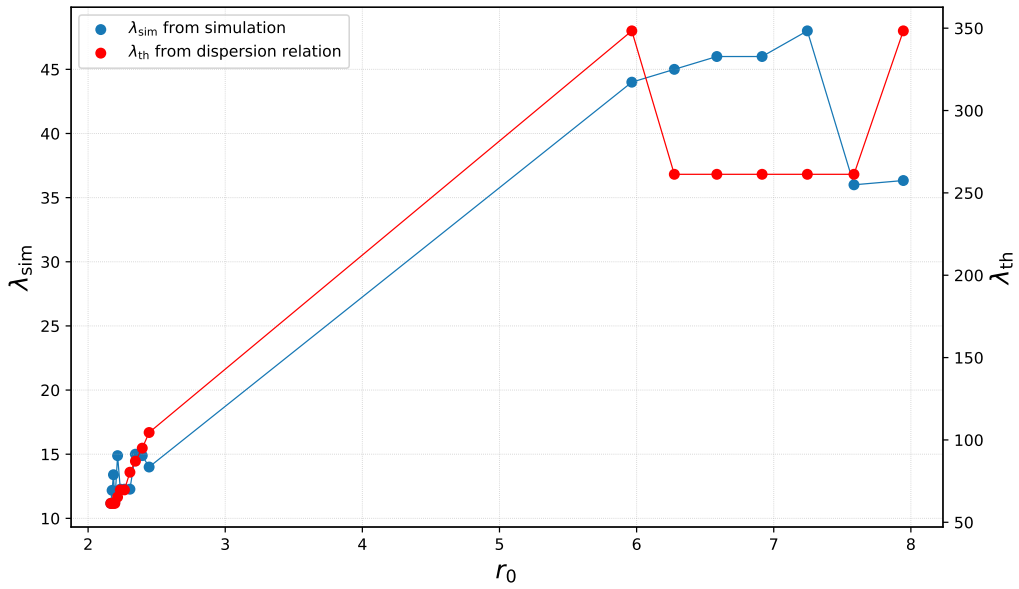

Figure 4.14: Numerical wavelength λ_{sim} (blue), obtained from the average spacing between adjacent corrugation peaks at $t = \tau_c$, compared with the theoretical prediction $\lambda_{\text{th}} = 2\pi/q_{\max}$, as a function of the stationary branch half-width r_0. The theoretical curve underestimates the theoretical prediction by close to an order of magnitude. As for the other tests, the scales differ but the qualitative trend with r_0 is reproduced.

Last, we test the maximum growth rate directly, by tracking the exponential growth of the perturbation in the early linear regime following the onset of the instability. In particular, starting from Eq (3.46), one can diagonalize the system using $P = [\mathbf{v}_1, \mathbf{v}_2]$, the matrix of eigenvectors.
In the new coordinates, each Fourier mode evolves exponentially,

$$\begin{cases} \partial_t \tilde{\epsilon}_1 = \sigma_1 \tilde{\epsilon}_1 & \rightarrow \quad \tilde{\epsilon}_1(t) = \tilde{\epsilon}_1(0)\, e^{\sigma_1 t} \\ \partial_t \tilde{\epsilon}_2 = \sigma_2 \tilde{\epsilon}_2 & \rightarrow \quad \tilde{\epsilon}_2(t) = \tilde{\epsilon}_2(0)\, e^{\sigma_2 t} \end{cases}, \tag{4.9}$$

where σ_1 and σ_2 are the eigenvalues of the linear stability matrix. Specifically, $\tilde{\epsilon}_1$ grows exponentially

for some mode $q \in [0, q_{\max}]$, while $\tilde{\epsilon}_2$ decays exponentially to zero for all wavenumbers. Transforming back to the original coordinates, where ϵ_1 is the width perturbation, and taking the long-time limit in which the contribution of the decaying mode σ_2 has vanished, while remaining within the linear regime, gives

$$\epsilon_1(t) = a\,\tilde{\epsilon}_1(0)\,e^{\sigma_1 t} + \cancel{b\,\tilde{\epsilon}_2(0)\,e^{\sigma_2 t}} \propto e^{\sigma_{\max} t}, \tag{4.10}$$

where a and b are determined by the matrix element of P.

Using the peaks identified in the previous test, we track the branch width at the peak locations as a function of time (Fig. 4.15). We then select the exponential growth regime and perform a linear fit of $\log(2r_{\max})$ against time (Fig. 4.16), from which the slope directly yields $\sigma^{\text{fit}}_{\max}$. For direct comparison with the first test, this is converted into the e-folding time, $\tau^{\text{fit}}_{\text{sim}} = 1/\sigma^{\text{fit}}_{\max}$, shown in Fig. 4.17.

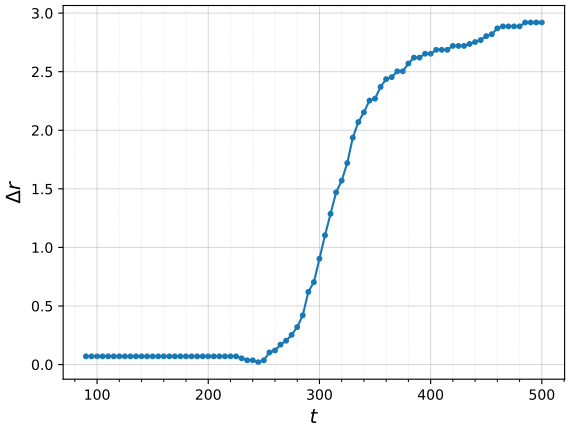

Figure 4.15: Average half-branch width at the peak positions as a function of time, for the stationary branch with $a = 2.634$, after subtracting the unperturbed width $2r_0$, meaning $\Delta r(t) = \langle 2r_{\max}(t)\rangle - 2r_0$. Three regimes are visible: an initial plateau near zero, during which the perturbation is below the detection level; an intermediate exponential growth phase, consistent with the linear regime of Eq. (4.10); and a final saturation phase.

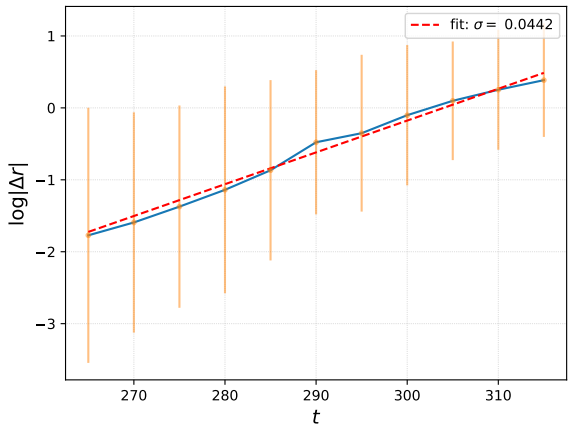

Figure 4.16: Linear fit of $\log(\langle 2r_{\max}\rangle - 2r_0)$ against time, for the same branch as in Fig. 4.15. The exponential growth regime is selected as $t \in [265, 315]$, based on the plateau-to-saturation transition identified there. The resulting fit gives $\sigma^{\text{fit}}_{\max} = 0.0442$ for this branch.

A closer look at the two characteristic time estimates shows that, both methods overestimate the theoretical characteristic time but the threshold-based estimate does so much more severely. This is due to a systematic bias in the threshold criterion itself: the 10% threshold in Eq. (4.8) requires a substantial amount of corrugation to build up before being triggered, which delays the measured onset relative to the true instability. Lowering the threshold would reduce this bias, but at the cost of an increased risk of spurious detections, since a sufficiently small threshold can be exceeded by statistical fluctuations of σ_w around its unperturbed, near-zero baseline, rather than by a real instability. In contrast, the exponential-fit estimate directly measures the perturbation growth in the linear regime, avoids the threshold bias and is generally more reliable. However, it is quite sensitive to the selected linear fitting range and still systematically overestimates the theoretical value, even under an ideal fit.

Overall, the four quantitative tests consistently indicate that the dispersion relation captures the correct physical mechanisms underlying the pearling instability. The predicted dependence on the stationary branch width is reproduced in all observables: branches closer to the stability threshold destabilize more slowly, require larger domains to exhibit pearling, and develop perturbations with longer characteristic wavelengths. However, in each test, the numerical values differ from the theoretical prediction by approximately an order of magnitude. Therefore, the dispersion relation derived from linear theory cannot be regarded as quantitatively predictive of the full nonlinear dynamics, but rather only as qualitatively indicative of the trend.

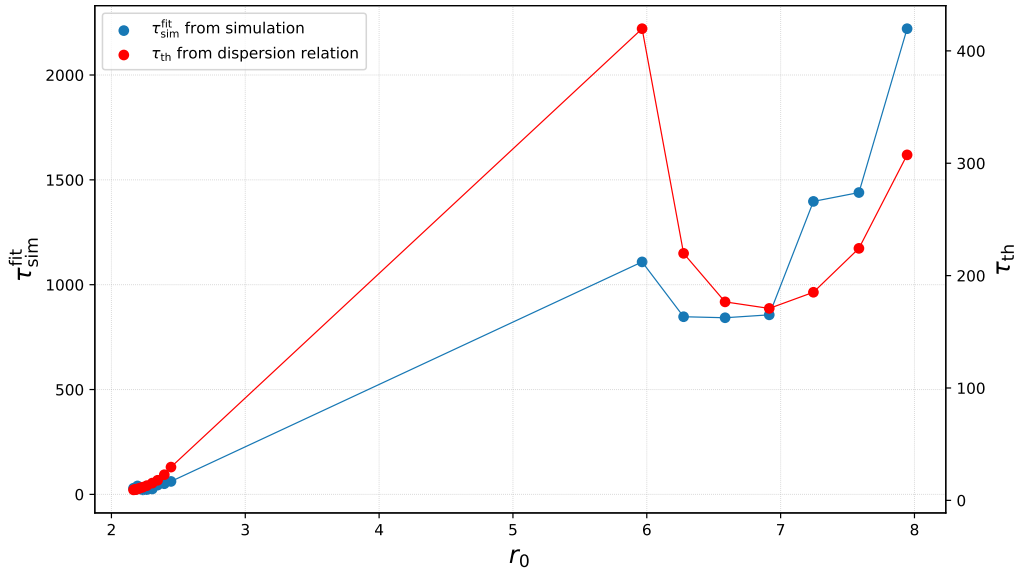

Figure 4.17: Characteristic time obtained from the exponential fit, $\tau^{\text{fit}}_{\text{sim}} = 1/\sigma^{\text{fit}}_{\text{max}}$ (blue), compared with the theoretical prediction $\tau_{\text{th}} = 1/\sigma_{\text{max}}$, as a function of the stationary branch half-width r_0. The theoretical and numerical curve still differ about an order of magnitude, but markedly closer to theory than the threshold-based estimate of the first test. This is consistent with the fit directly probing the physical exponential growth of the perturbation, rather than relying on an arbitrary corrugation-amplitude threshold.

Chapter 5

Connection between Tr_{r_0} and η_{r_0}

The perturbative theory developed in Sec. 3.4 treats the branch half-width and the mass redistribution potential as independent dynamical variables. This choice is required for a self-consistent description of the linear dynamics and correctly accounts for the different evolution equations governing the two fields $\rho_{r(y.t)}(x)$ and $\eta_{r(y,t)}$.

Nevertheless, the numerical results shown in Fig. 4.1 validate the physical intuition underlying the instability mechanism. As expected, the derivatives of the reactive turnover and the mass redistribution potential are strongly anti-correlated along the stationary branch family. In particular, the instability criterion $\partial_r Tr_r|_{r=r_0} > 0$ is almost equivalent to the condition

$$\partial_r \eta_r\big|_{r=r_0} < 0, \tag{5.1}$$

apart from a small shift in the locations of the extrema.

This suggests that the two quantities are not independent, even though no direct analytical relation between them is available within the two-amplitude formulation. The purpose of this section is therefore not to develop an alternative perturbative theory, but rather to explore whether a simplified one-parameter ansatz can provide additional insight into the connection between Tr_{r_0} and η_{r_0}. As will be shown below, this approach reproduces the qualitative instability criterion obtained previously and yields an approximate relation between the two quantities, although it is not mathematically self-consistent and therefore should be regarded only as an exploratory approximation.

Instead of introducing two independent perturbation amplitudes, we assume that the branch width is perturbed according to

$$r(y,t) = r_0 + \epsilon(t)\sin(qy), \tag{5.2}$$

while all remaining quantities, including η_r, are then obtained via a Taylor expansion around the unperturbed stationary branch half-width $r = r_0$.

Under this simplified ansatz, linearizing the dynamics yields two distinct evolution equations for the single perturbation amplitude $\epsilon(t)$:

$$\begin{aligned} \partial_t \epsilon(t) &= -\frac{2r_0\, D_c\, q^2\, \partial_r \eta_r\big|_{r=r_0}}{A}\, \epsilon(t) \\ \partial_t \epsilon(t) &= \frac{D_m q^2 A - 2r_0\,(D_c + D_m)\, q^2\, \partial_r \eta_r\big|_{r=r_0} - 2\,\partial_r Tr_r\big|_{r=r_0}}{2r_0\,\partial_r \eta_r\big|_{r=r_0}}\, \epsilon(t) \end{aligned}, \tag{5.3}$$

where the first equation derives from the linearization of Eq. (3.23), which describes the dynamics of the total mass within branch ϕ_r, while the second arises from Eq. (3.34), which governs the evolution of the mass redistribution potential η_r.

The first equation immediately recovers the stability criterion of Eq. (5.1). Thus, despite its simplicity, the one-parameter ansatz already reproduces the same instability threshold suggested by the physical interpretation of the mass redistribution potential (Sec. 3.3).

A fundamental inconsistency, however, immediately appears. Since both equations govern the evolution of the same perturbation amplitude $\epsilon(t)$, they ought to predict an identical growth rate. Figure 5.1 shows that this is generally not the case: the two expressions produce distinct dispersion relations, often with opposite curvature, demonstrating that, the one-parameter ansatz over-constrains the dynamics. In other words, the η potential and the branch width cannot be forced to evolve through a single perturbation amplitude without losing part of the dynamics. This observation provides additional justification for the introduction of two independent perturbation amplitudes in Sec. 3.4.

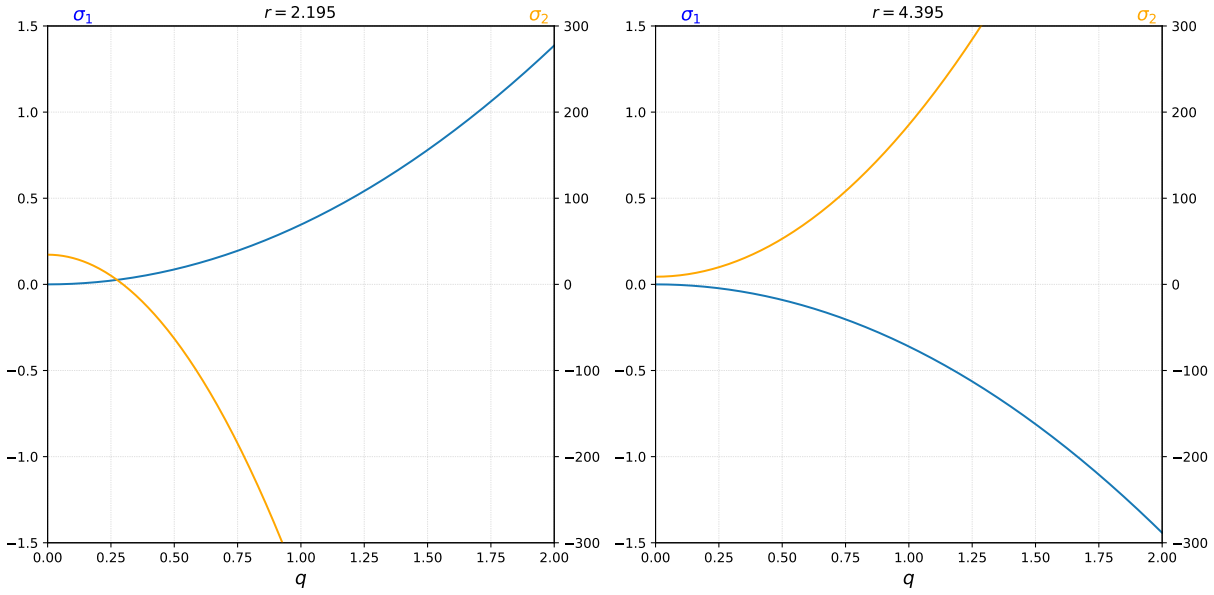

Figure 5.1: Growth rates obtained from the two evolution equations in Eq. (5.3) for different stationary branch half-widths r_0. The first expression, $\sigma_1 = -2r_0\, D_c\, q^2\, \partial_r \eta_r|_{r=r_0}/A$ (in blue), correctly predicts the instability onset as a consequence of the sign anti-correlation between $\partial_r \eta_r|_{r=r_0}$ and $\partial_r Tr_r|_{r=r_0}$, up to a small shift in the locations of their extrema. Nevertheless, the two growth rates do not coincide, demonstrating the internal inconsistency of the one-parameter ansatz. Furthermore, neither dispersion relation is physically consistent: whenever an unstable band is present, the growth rate diverges as $q \to \infty$, whereas a physically meaningful conserved system must recover negative growth rates at sufficiently large wavenumbers.

Although the one-parameter ansatz is not self-consistent as a dynamical theory, it can still be used as an exploratory approximation. In particular, by exploiting the separation of timescales between the fast relaxation of η and the slower dynamics of the total mass, it is possible to derive an approximate relation between $\partial_r \eta_r|_{r=r_0}$ and $\partial_r Tr_r|_{r=r_0}$.

Specifically, since the dynamics of η operates on a much faster timescale than total mass redistribution via diffusion, we perform an adiabatic (quasi-stationary) approximation by setting $\partial_t \eta_r = 0$ in the second equation of Eq. (5.3):

$$0 = \frac{D_m q^2 A - 2r_0\,(D_c + D_m)\, q^2\, \partial_r \eta_r\big|_{r=r_0} - 2\,\partial_r Tr_r\big|_{r=r_0}}{2r_0\,\partial_r \eta_r\big|_{r=r_0}}\,\epsilon(t). \tag{5.4}$$

Moreover, since cytosolic diffusion is substantially faster than membrane diffusion, we introduce

$$d_m \equiv \frac{D_m}{D_c} \ll 1 \tag{5.5}$$

and expand to leading order in d_m.

This yields

$$\partial_r \eta_r\big|_{r=r_0} = -k(q)\,\partial_r Tr_r\big|_{r=r_0} + d_m \frac{A}{r_0}, \tag{5.6}$$

with $k(q) \equiv 1/(D_c\, r_0\, q^2) > 0$.

Equation (5.6) provides an explicit analytical explanation for the anti-correlation observed numerically between $\partial_r \eta_r|_{r=r_0}$ and $\partial_r Tr_r|_{r=r_0}$.

The primary term $-k(q)\,\partial_r Tr_r|_{r=r_0}$ dictates that the two derivatives carry opposite signs across most of the domain. Crucially, the small positive shift $d_m \frac{A}{r_0}$ explains the spatial displacement between their respective extrema observed in Fig. 4.1:

- Near a maximum of Tr_{r_0} (where $\partial_r Tr_r|_{r=r_0}$ decreases toward zero from positive values), $\partial_r \eta_r|_{r=r_0}$ vanishes when $\partial_r Tr_r|_{r=r_0} = d_m\, A/(r_0\, \kappa(q)) > 0$. Thus, the minimum of η_{r_0} occurs at a smaller value of r_0 relative to the maximum of Tr_{r_0}.
- Conversely, near a minimum of Tr_{r_0} (where $\partial_r Tr_r|_{r=r_0}$ increases toward zero from negative values), $\partial_r \eta_r|_{r=r_0}$ vanishes after $\partial_r Tr_r|_{r=r_0}$ has already crossed into positive values. Consequently, the maximum of η_{r_0} is shifted toward a larger value of r_0 relative to the minimum of Tr_{r_0}.

It should be noted that Eq. (5.6) cannot be interpreted as a exact relation. Since Tr_{r_0} and η_{r_0} are intrinsic static properties of the stationary branch, they cannot genuinely depend on the perturbation wavenumber q. The presence of $k(q)$ indicates that this relation is solely a byproduct of the quasi-stationary reduction.

Finally, substituting Eq.(5.6) into the first equation of Eq. (5.3) gives

$$\partial_t \epsilon(t) = \left(\frac{2}{A} \partial_r Tr_r\big|_{r=r_0} - 2 D_m q^2 \right) \epsilon(t), \tag{5.7}$$

which corresponds to a Type-III dispersion relation. The instability threshold is again determined solely by the sign of $\partial_r Tr_r|_{r=r_0}$, in agreement with the full two-parameter perturbative theory. However, this dispersion relation violates global mass conservation, as it fails to satisfy $\sigma(q=0) = 0$.
Figure 5.2 compares this outcome with the exact result from the two-parameter theory for representative stable and unstable stationary branches.

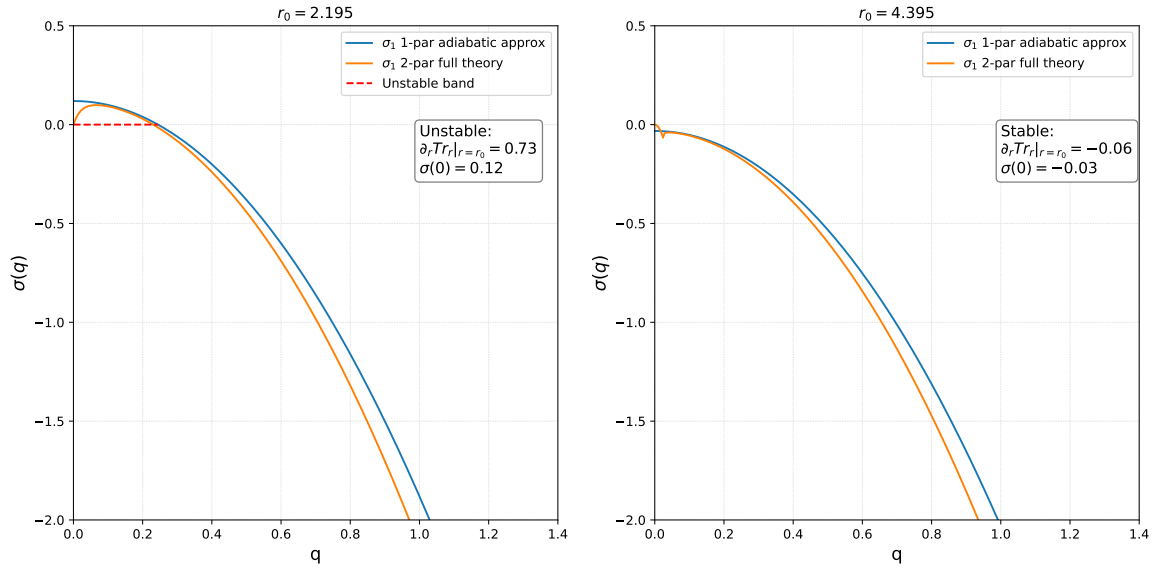

Figure 5.2: Dispersion relation obtained from the quasi-stationary reduction of the one-parameter ansatz (blue) compared with the exact one from the two-parameter theory (orange). The right panel shows a stable branch with $\partial_r Tr_r|_{r=r_0} < 0$, while the left panel shows an unstable branch with $\partial_r Tr_r|_{r=r_0} > 0$. Although the resulting Type-III instability is incompatible with the conservation law, the correct instability threshold is nevertheless recovered.

In conclusion, the one-parameter ansatz does not provide a self-consistent description of the branch dynamics and therefore cannot replace the two-parameter perturbative theory. By constraining the branch width and the mass redistribution potential to evolve through a single degree of freedom, it over-constrains the dynamics and fails to reproduce the correct dispersion relation of the conserved system. Nevertheless, it provides a useful exploratory framework: it independently recovers the instability criterion, offers an analytical explanation for the observed anti-correlation between $\partial_r Tr_r|_{r=r_0}$ and $\partial_r \eta_r|_{r=r_0}$, and clarifies why both quantities carry essentially the same information about the onset of the pearling instability.

Chapter 6

From McRD to active field theories

The previous chapters approached driven self-organization from a bottom-up, reaction-diffusion perspective, in which pattern formation emerges from the explicit chemical kinetics coupling membrane-bound and cytosolic species. The remainder of the work develops a complementary, top-down perspective, provided by active field theories for conserved scalar order parameters, in which non-equilibrium effects are introduced directly at the coarse-grained level, without reference to any underlying microscopic reaction network.

The two perspectives are not independent. The central result of this chapter is that the late-time dynamics of the three-component McRD model studied so far can be reduced, by successive elimination of the fast internal degrees of freedom, to an effective active scalar field theory [14]. This reduction provides a direct, constructive bridge between McRD systems and active field theories, showing that non-equilibrium terms usually postulated on symmetry grounds can instead emerge from a concrete microscopic mechanism. In doing so, it introduces Active Model B$^-$ (AMB$^-$) as a specific new model that interpolates continuously between several well-known models. This last point is the reason AMB$^-$ is a natural framework in which to revisit, in the final part of this thesis, the pearling instability already characterized for the three-component McRD model.

6.1 Passive and Active Model B

Among active field theories [2], Active Model B (AMB) [19] represents the simplest non-equilibrium extension of Model B, namely the Cahn-Hilliard theory, which is the canonical field theory for diffusive scale separation of a conserved scalar field ϕ in the absence of momentum conservation.
Before turning to its active generalization, it is useful to first recall the passive dynamics, governed by a Landau ϕ^4 free energy with conserved dynamics that follows continuity equation:

$$\begin{aligned} \partial_t \phi &= -\nabla \cdot \mathbf{J}, \\ \mathbf{J} &= -M \nabla \mu, \\ \mu = \frac{\delta F[\phi]}{\delta \phi} &= a(T)\phi + b\phi^3 - \kappa \nabla^2 \phi, \end{aligned} \tag{6.1}$$

where M is the mobility and $\mathcal{F}[\phi] = \int d\mathbf{x}\, \frac{a(T)}{2}\phi^2 + \frac{b}{4}\phi^4 + \frac{\kappa}{2}(\nabla\phi)^2$ is the Landau ϕ^4 free-energy functional.

The structure of passive field theories is strongly constrained by the time-reversal symmetry (TRS) of the underlying microscopic dynamics. As a consequence, the deterministic evolution can be derived from a free-energy functional, the steady state is characterized by a unique Boltzmann distribution, and detailed balance is satisfied.
Active systems, by contrast, continuously consume and dissipate energy at the microscopic scale, thereby breaking time-reversal symmetry. As a result, their coarse-grained dynamics generally cannot be derived from a free-energy functional, and neither detailed balance nor Boltzmann statistics hold at steady state.

The simplest way to construct an active field theory is therefore to add explicit TRS-breaking contributions to the chemical potential, so that the field dynamics no longer has to arise from a free energy. For example, AMB is obtained by adding a non-equilibrium term to the Cahn-Hilliard dynamics:

$$\begin{aligned} \partial_t \phi &= -\nabla \cdot \mathbf{J}, \\ \mathbf{J} &= -M \nabla \mu, \\ \mu = \frac{\delta F[\phi]}{\delta \phi} + \mu_A &= a(T)\phi + b\phi^3 - \kappa \nabla^2 \phi + \nu \left(\nabla \phi\right)^2, \end{aligned} \tag{6.2}$$

where $\mu_A \equiv \nu(\nabla\phi)^2$ is the active contribution and ν is the activity parameter.

The non-equilibrium character of this term becomes explicit when one considers the most general local free-energy functional containing a field-dependent stiffness coefficient $\kappa(\phi)$,

$$\mathcal{F}[\phi] = \int d\mathbf{x} \left[f(\phi) + \frac{\kappa(\phi)}{2} \left(\nabla \phi\right)^2 \right], \tag{6.3}$$

whose variational derivative is

$$\frac{\delta \mathcal{F}[\phi]}{\delta \phi} = \frac{\partial f}{\partial \phi} - \kappa(\phi)\nabla^2 \phi - \frac{\kappa'(\phi)}{2} (\nabla \phi)^2. \tag{6.4}$$

Any free-energy-derivable model therefore has its $(\nabla\phi)^2$ coefficient locked to the derivative of the Laplacian coefficient. When κ is constant, the AMB contribution $\nu(\nabla\phi)^2$ cannot be generated from any free-energy functional, since $2\nu \neq \kappa'(\phi) = 0$ for $\nu \neq 0$. Thus it is, by construction, an explicit violation of time-reversal symmetry.

Despite this non-equilibrium contribution, AMB typically undergoes bulk phase separation and displays phenomenology that remains qualitatively close to that of passive Model B, apart from anomalous phase coexistence. The active term contributes predominantly at interfaces, where $|\nabla\phi| > 0$, whereas the bulk phases are characterized by $|\nabla\phi| \simeq 0$ and therefore resemble the canonical Cahn-Hilliard description.

Active terms such as μ_A are usually introduced phenomenologically, constrained only by symmetry. The connection between active field theories and McRD systems developed below is instead constructive: active contributions to the chemical potential emerge from the elimination of internal degrees of freedom of the reaction network, rather than being postulated a priori. In the remainder of this chapter, we show that the late-time dynamics of the three-component McRD model studied in the previous chapters can be reduced to an effective scalar conserved field theory.

6.2 Late time reduction

We now derive the effective scalar description starting from the evolution equations for the total local density ρ and the mass redistribution potential η in Eq. (2.13). For the derivation we keep a generic form of the reactive term R, meaning

$$R = (1 - d_m) R_1(m, c_a, c_i) = (1 - d_m) \left[\gamma(m) c_a - \alpha(m)\right]. \tag{6.5}$$

Using the definitions of η, Eq. (2.10), and ρ, Eq. (2.9), the membrane and active cytosolic concentrations can be expressed as

$$m = \frac{\rho - \eta}{1 - d_m}, \qquad c_a = \frac{\eta - d_m \rho}{1 - d_m} - c_i. \tag{6.6}$$

Substituting these relations into the η equation yields

$$\partial_t \eta = D_c(1 + d_m)\nabla^2 \eta - D_m \nabla^2 \rho - (1 - d_m) \left[\gamma\left(m\right) \frac{\eta - d_m \rho}{1 - d_m} - \gamma\left(m\right) c_i - \alpha\left(m\right) \right], \tag{6.7}$$

where m is intended as $m(\rho, \eta)$.

The first simplification consists in a quasi-stationary elimination of η since its dynamics is controlled by the reaction timescale, which is much shorter than the timescale associated with mass redistribution. Moreover, at late times, near equilibration, $\eta(\mathbf{x})$ becomes nearly spatially uniform, so that its diffusive contribution can be neglected setting $\nabla\eta \simeq 0$:

$$\eta = -\frac{D_m}{\gamma\left(m(\rho,\eta)\right)}\nabla^2\rho + d_m\rho + (1-d_m)\left[c_i + \frac{\alpha\left(m(\rho,\eta)\right)}{\gamma\left(m(\rho,\eta)\right)}\right]. \tag{6.8}$$

A second quasi-stationary approximation, motivated by the same separation of timescales, can be applied to the inactive species c_i, yielding

$$c_i = \left(\lambda - D_c\nabla^2\right)^{-1}\alpha\left(m(\rho,\eta)\right). \tag{6.9}$$

For large wavelengths compared with the screening length $\ell \equiv \sqrt{D_c/\lambda}$ (i.e. $q\ell \ll 1$), we can Taylor expand the inverse operator to obtain

$$c_i = \lambda^{-1}\left(1 + \ell^2\nabla^2 + \ell^4\nabla^4\right)\alpha\left(m(\rho,\eta)\right). \tag{6.10}$$

To derive a closed equation for the conserved total density ρ alone, we approximate the membrane density by the total density, $m \to \rho$. More details can be found in [14].
This approximation gives

$$\eta = -\frac{D_m}{\gamma(\rho)}\nabla^2\rho + d_m\rho + (1-d_m)\left[\lambda^{-1}\left(1 + \ell^2\nabla^2 + \ell^4\nabla^4\right)\alpha(\rho) + \frac{\alpha(\rho)}{\gamma(\rho)}\right]. \tag{6.11}$$

Finally, substituting this expression into the conservation law and expanding to leading order in $d_m \ll 1$ leads to an effective scalar conserved field theory, which reads

$$\begin{aligned}\partial_t\rho =& D_c\nabla^2\left[d_m\rho + \left(\frac{1}{\lambda} + \frac{1}{\gamma(\rho)}\right)\alpha(\rho)\right.\\ &\left. + \left(\frac{D_c}{\lambda^2}\alpha'(\rho) - \frac{D_m}{\gamma(\rho)}\right)\nabla^2\rho + \frac{D_c}{\lambda^2}\alpha''(\rho)\left(\nabla\rho\right)^2 + \frac{D_c^2}{\lambda^3}\nabla^4\alpha(\rho)\right].\end{aligned} \tag{6.12}$$

Equation (6.12) already displays the characteristic ingredients of an active scalar field theory. In particular, the term proportional to $\alpha''(\rho)(\nabla\rho)^2$ constitutes an explicit non-equilibrium contribution, directly analogous to the active chemical potential μ_A of AMB, while the higher-order gradient term proportional to $\nabla^4\alpha(\rho)$ is responsible for the finite-wavelength instability characteristic of AMB$^-$. Crucially, both terms arise here from the reaction kinetics $\alpha(\rho)$ alone, with no free-energy input assumed. This is precisely the constructive, microscopic origin of activity announced above.

6.3 The general AMB$^-$

Equation (6.12) is a special case of a more general active scalar field theory,

$$\partial_t\phi = M\nabla^2\left[\eta^*(\phi) - \kappa(\phi)\nabla^2\phi + \nu(\phi)(\nabla\phi)^2 + \nabla^4\chi(\phi)\right], \tag{6.13}$$

which we identify as the general form of AMB$^-$. The name derives from the fact that the effective surface tension can change sign, consequently triggering pattern formation through a localized negative stiffness.
Equation (6.13) is deliberately written to expose its generality: for suitable choices of $\eta^*(\phi)$, $\kappa(\phi)$, $\nu(\phi)$, and $\chi(\phi)$ it reduces not only to the late-time reduction of the three-component McRD, but also to the long-time limit of the two-component McRD model [17], to standard AMB [19], and to the conserved Swift-Hohenberg model (also known as Phase-Field Crystal model) [3, 12]. Table 6.1 summarizes these limits and the connections between them.

A clarification regarding notation is in order. Throughout this thesis the McRD total local density is denoted by ρ, whereas the order parameter of a generic active conserved scalar field theory is conventionally denoted by ϕ; Eq. (6.13) is written in the latter, generic notation, since it is meant to hold for the whole family of models discussed below. When specializing to the McRD reductions, ϕ is to be identified with the physical density ρ, and we keep the results of Sec. 6.2 expressed in ρ rather than translating them into ϕ. For standard AMB and PFC, which are not derived from any underlying reaction network, we retain the conventional field notation ϕ.

AMB⁻	**3-comp McRD**	**2-comp McRD**	**AMB**	**PFC**
$\eta^*(\phi)$	$d_m\rho + \left(\frac{1}{\lambda} + \frac{1}{\gamma(\rho)}\right)\alpha_0\rho$	$d_m\rho + \frac{\alpha_0\rho}{\gamma(\rho)}$	$-\phi + \phi^3$	$-\phi + \phi^3$
$\kappa(\phi)$	$\frac{D_m}{\gamma(\rho)} + \frac{D_c\alpha_0}{\lambda}$	$\frac{D_m}{\gamma(\rho)}$	$\kappa > 0$	$\kappa < 0$
$\chi(\phi)$	$\frac{D_c^2}{\lambda^3}\alpha_0\rho$	0	0	$K\phi,\ K > 0$
$\nu(\phi)$	0	0	ν	0

Table 6.1: Explicit forms of $\eta^*(\phi)$, $\kappa(\phi)$, $\chi(\phi)$, and $\nu(\phi)$ appearing in the general AMB⁻ functional, Eq. (6.13), for the limiting cases discussed in the text: the late-time reduction of the three- and two-component McRD models (with $\alpha(\rho) = \alpha_0\rho$), standard Active Model B, and the conserved Swift-Hohenberg (PFC) model.

Three features of Table 6.1 are worth stressing. The two-component McRD limit is recovered from the three-component one for $\lambda \to \infty$, consistent with the physical intuition that, as reactivation becomes instantaneous, the model collapses onto a description with no independent inactive pool. In this limit, the resulting model is a conserved scalar theory with no active contribution ($\chi = 0 = \nu$), and can indeed be written as the gradient flow of a free-energy functional, meaning it corresponds to passive Model B. The three-component reduction, by contrast, has $\chi \neq 0$ while $\nu = 0$: its non-equilibrium character is therefore not of the same form as in standard AMB, where activity enters through the second-order term $\nu(\nabla\phi)^2$, but it is instead carried entirely by the fourth-order term $\nabla^4\chi(\phi)$. Finally, the same fourth-order structure that generates $\chi \neq 0$ for the McRD reduction is exactly the ingredient that also defines the conserved PFC model. It differs from the three-component reduction essentially in the sign of κ. The McRD reduction can therefore be seen as a natural non-equilibrium generalization of PFC.

AMB⁻ sits halfway between AMB and PFC. Like AMB, it is a genuinely active model of Model B; whereas like PFC, and unlike standard AMB, it supports finite-wavelength pattern selection. This combination allows AMB⁻ to display phenomenology as rich as that of Active Model B⁺ (AMB⁺) [13], while retaining a purely gradient current, $\mathbf{J} = -M\nabla\mu$ for a well-defined scalar $\mu = \eta^*(\phi) - \kappa(\phi)\nabla^2\phi + \nu(\phi)(\nabla\phi)^2 + \nabla^4\chi(\phi)$, thereby avoiding the circulating, non-potential currents characteristic of AMB⁺.

This unification is the main motivation for the remainder of this work. The three-component McRD model was shown in the previous chapters to support a pearling instability driven by the interplay between reaction kinetics and diffusive mass redistribution. Equation (6.12) shows that this same interplay, once the fast internal degrees of freedom are eliminated, is encoded in the density dependence of $\kappa(\phi)$ and $\chi(\phi)$ appearing in the general AMB⁻ functional, Eq. (6.13). In the following chapters we therefore repeat, directly within AMB⁻, the procedure developed for the three-component McRD model to characterize the pearling instability, asking whether it survives in this reduced, purely scalar description: if so, this would establish pearling as a generic property of the active scalar field theory itself, rather than a peculiarity of the full three-component reaction network from which it was originally derived.

Chapter 7

Active Model B$^-$

7.1 Model and LSA

Motivated by the classification summarized in Tab. 6.1, we consider the following minimal model, obtained by choosing $\eta^*(\phi) = -\phi + \phi^3$ and $\kappa(\phi) = \tanh(\phi_0 - \phi)$:

$$\partial_t \phi = M\nabla^2 \underbrace{\left[-\phi + \phi^3 - \tanh(\phi_0 - \phi)\nabla^2\phi + K\nabla^4\phi\right]}_{\equiv \eta[\phi]}, \tag{7.1}$$

where $\eta[\phi]$ plays the role of mass redistribution potential. Unlike the three-component McRD model, here η does not possess its own dynamics, being a functional of ϕ.
Equation (7.1) combines three main ingredients. The bulk term $-\phi + \phi^3$ is the functional derivative of the standard Landau ϕ^4 free energy, familiar from classical phenomenological field theories. The stiffness coefficient $\kappa(\phi) = \tanh(\phi_0 - \phi)$, which changes sign depending on the value of the field relative to the reference density ϕ_0, is the distinguishing feature of the AMB$^-$ construction. Similar to the three-component McRD reduction, no active $(\nabla\phi)^2$ term is present here; stability at large wavenumber is instead ensured by the fourth-order term $K\nabla^4\phi$, characteristic of models exhibiting finite-wavelength pattern selection.

We proceed with a linear stability analysis (LSA) around a homogeneous steady state. Throughout this chapter we fix $M = 10$ and $K = 0.055$, treating the offset ϕ_0 and the average total density $\bar{\phi}$ (directly associated with $M_{\text{tot}} = \bar{\phi}\,\mathcal{V}$ since the volume of the system is constant) as free control parameters.

Since every spatial derivative of a constant field vanishes, any constant solution $\bar{\phi} \in \mathbb{R}$ is trivially a steady state of Eq. (7.1). Perturbing this state as

$$\phi(\mathbf{x}, t) = \bar{\phi} + \delta\phi(\mathbf{x}, t), \tag{7.2}$$

and retaining only linear terms in $\delta\phi$, we obtain

$$\partial_t\, \delta\phi = M\nabla^2 \left[(-1 + 3\bar{\phi}^2)\, \delta\phi - \tanh\big(\phi_0 - \bar{\phi}\big)\, \nabla^2\delta\phi + K\nabla^4\delta\phi\right]. \tag{7.3}$$

Passing to Fourier space and assuming $\delta\phi(q, t) \sim e^{\sigma(q)t}$ yields the dispersion relation

$$\sigma(q) = M\left[(1 - 3\bar{\phi}^2)q^2 - \tanh\big(\phi_0 - \bar{\phi}\big)q^4 - Kq^6\right]. \tag{7.4}$$

Since $M > 0$ only rescales the growth rate without affecting its sign, the linear stability of $\bar{\phi}$ is entirely controlled by the sign of the function $f(q) = aq^2 + bq^4 - Kq^6$, with $a \equiv 1 - 3\bar{\phi}^2$ and $b \equiv -\tanh\big(\phi_0 - \bar{\phi}\big)$. In particular, the type of dispersion relation can be characterized through the roots of the auxiliary parabola $f(y) = -Ky^2 + by + a$ (with $y = q^2$): their number and location depend only on the sign of a and on the relative magnitude of b, reproducing the same three-regime classification already found for the three-component McRD system.

When $a > 0$, or when $a = 0$ and $b > 0$, the $q = 0$ mode is only marginally stable and the growth rate is positive on a finite interval $q \in [0, q_{\max}]$: this defines a Type II instability (see Fig. 7.1). When instead $a < 0$, long-wavelength modes are stable, but if the destabilizing q^4 contribution is strong enough, $b \geq 2\sqrt{|a|K}$, a finite band of intermediate wavenumbers becomes unstable while both $q \to 0$ and $q \to \infty$ remain damped: this is the conserved Type I instability (see Fig. 7.2). Finally, the homogeneous state is linearly stable whenever $a < 0$ and $b < 2\sqrt{|a|K}$, or whenever $a = 0$ and $b \leq 0$.

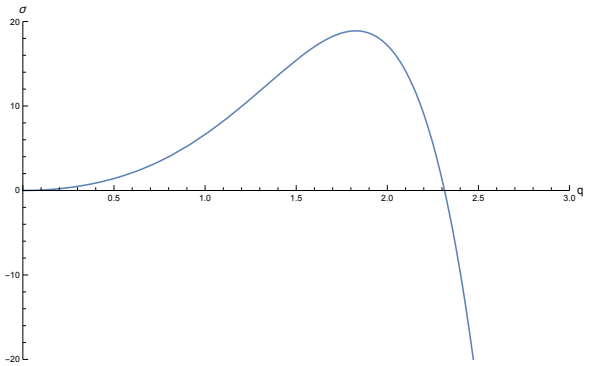

Figure 7.1: Type II instability. Parameters: $K = 0.55$, $M = 10$, $\bar{\phi} = 0.4$, $\phi_0 = 0.2$.

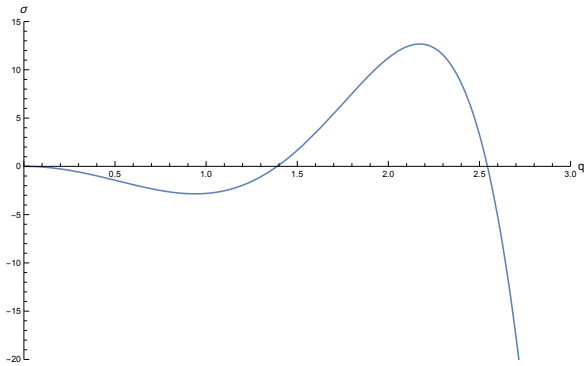

Figure 7.2: Conserved Type I instability. Parameters: $K = 0.55$, $M = 10$, $\bar{\phi} = 0.75$, $\phi_0 = 0.25$.

The boundaries separating these three regimes can be written explicitly in the $(\bar{\phi}, \phi_0)$ control-parameter plane. The condition $a = 0$ is independent of ϕ_0 and simply yields the two vertical lines $\bar{\phi} = \pm 1/\sqrt{3}$, separating the central Type II region ($|\bar{\phi}| < 1/\sqrt{3}$) from the outer region where $a < 0$. Within the latter, the Type I/stable boundary follows from $b = 2\sqrt{|a|K}$, which can be inverted for ϕ_0:

$$\phi_0 = \bar{\phi} - \operatorname{arctanh}\left(2\sqrt{K\left(3\bar{\phi}^2 - 1\right)}\right), \qquad |\bar{\phi}| > \frac{1}{\sqrt{3}}, \tag{7.5}$$

provided that the argument of arctanh() remains below unity. Beyond this range the Type I instability is no longer accessible for any ϕ_0, and the homogeneous state is unconditionally stable. Figure 7.3 presents the resulting linear stability diagram in the $(\bar{\phi}, \phi_0)$ plane.

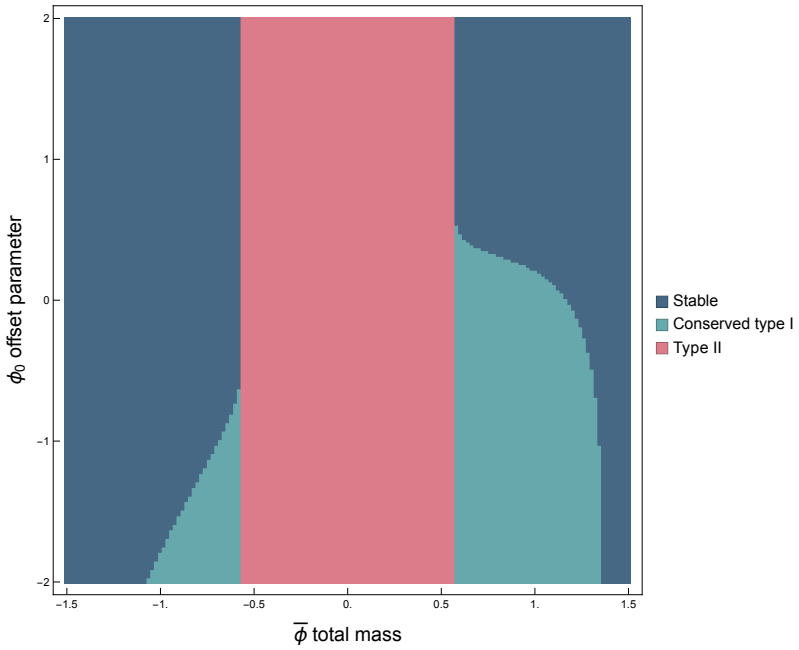

Figure 7.3: Linear stability diagram. The total density $\bar{\phi}$ and the offset ϕ_0 are the control parameters, while $M = 10$ and $K = 0.055$ are kept fixed. Three different behaviors are observed: in blue the stable homogeneous regime, in green the conserved Type I instability, and in pink the Type II instability.

7.2 Pearling instability

In this section we revisit, the asymptotic matching analysis of the pearling instability already developed for the three-component McRD model, adapting it to the Active Model B$^-$. The physical mechanism and the overall structure of the calculation remain the same: given an unperturbed stationary branch of half-width r_0, the interface is perturbed with a harmonic modulation along the transverse direction y, and the analysis is conducted on the branch slices by integrating the equation of the dynamics in the attachment zone.

7.2.1 One-dimensional stationary profile

The starting point is the one-dimensional stationary profile $\phi_{r_0}(x)$, solution of

$$0 = M\partial_x^2 \underbrace{\left[-\phi_{r_0} + \phi_{r_0}^3 - \tanh(\phi_0 - \phi_{r_0})\,\partial_x^2\phi_{r_0} + K\,\partial_x^4\phi_{r_0}\right]}_{\equiv \eta_{r_0}}. \tag{7.6}$$

With no-flux boundary conditions, the profile is stationary if and only if the mass redistribution potential η_{r_0} is constant in space, and the density is determined by

$$\eta_{r_0} = -\phi_{r_0} + \phi_{r_0}^3 - \tanh(\phi_0 - \phi_{r_0})\,\partial_x^2\phi_{r_0} + K\,\partial_x^4\phi_{r_0}. \tag{7.7}$$

Since this equation cannot be solved analytically, the profile is determined numerically in *COMSOL*, which is preferred to *Mathematica* because the equation to be solved has derivatives up to sixth-order. To solve the problem, two auxiliary variables are introduced, allowing the equation to be implemented in the General Form PDE interface. The computational domain is again fixed to $x \in [0, L]$, with $L = 100$. No-flux boundary conditions are imposed through $\Gamma \cdot \mathbf{n} = 0$, which correspond

$$\begin{aligned} \partial_x\eta[\phi]\big|_{x=0} &= 0 = \partial_x\eta[\phi]\big|_{x=L}, \\ \partial_x\phi(x,t)\big|_{x=0} &= 0 = \partial_x\phi(x,t)\big|_{x=L}, \\ \partial_x^3\phi(x,t)\big|_{x=0} &= 0 = \partial_x^3\phi(x,t)\big|_{x=L}. \end{aligned} \tag{7.8}$$

The initial condition adopts the same functional form as the analytical guess used for the three-component McRD system of Eq. (3.5):

$$\phi_a(x) = -0.11 - 1.01\,\tanh\left(\left|x - \frac{L}{2}\right| - a\right), \tag{7.9}$$

where the parameter a controls the conserved total mass $\bar{\phi}$ of the system. In this case the parameters b and c from Eq. (3.5) are no longer constrained to positive values, as the field ϕ does not necessarily represent a strictly positive physical mass. In particular, we fix $b = -0.11$ and $c = 1.01$, as this choice provides fast relaxation and minimal deviation from the initial guess width within the investigated parameter regime.

This choice of b and c is particularly suitable for $\phi_0 = 0.6$, a value that remains fixed throughout the rest of this work. We restrict our analysis to this value in order to isolate the pearling instability from a competing plateau-to-branch (or "finger") instability. For smaller values of ϕ_0, the branch is unstable over a substantial portion of the explored range of a, but the resulting perturbations predominantly develop into thinner branches rather than into pearls. Figure 7.4 shows an example, for $\phi_0 = 0.5$, of the finger-dominated dynamics that we seek to avoid.
Since our interest here is the competition between pearling and the linearly stable branch, we restrict the parameter range to $\phi_0 = 0.6$, where pearling provides the relevant transverse instability.

Starting from initial condition $\phi_a(x)$ of Eq. (7.9), the numerical dynamics relaxes toward a stationary branch profile $\phi_{r_0}(x)$. Similarly to what we described in Sec. 3.1, a profile is accepted as stationary only if the redistribution potential becomes spatially uniform and satisfies Eq. (3.7).

Examples of the resulting stationary profiles are shown in Figs. 7.5 and 7.6.

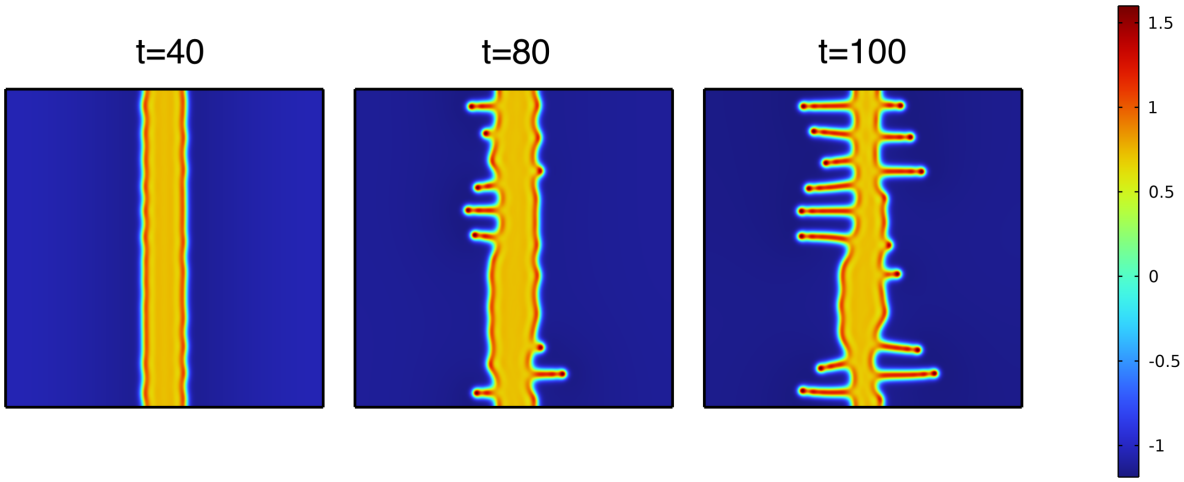

Figure 7.4: Plateau-to-branch instability for $\phi_0 = 0.5$, $M = 10$, $K = 0.55$, and a comparatively large total mass $\bar{\phi}$. Already at early times ($t = 40$) the branch is destabilized; however, the perturbations do not develop into dots (pearls) but instead give rise to new, thinner branches growing orthogonally to the original one. By $t = 80$ this process has intensified, and by $t = 100$ numerous new horizontal branches have sprouted from the original vertical branch. This is the finger instability that motivates our choice to set $\phi_0 = 0.6$, for which pearling becomes the dominant instability instead.

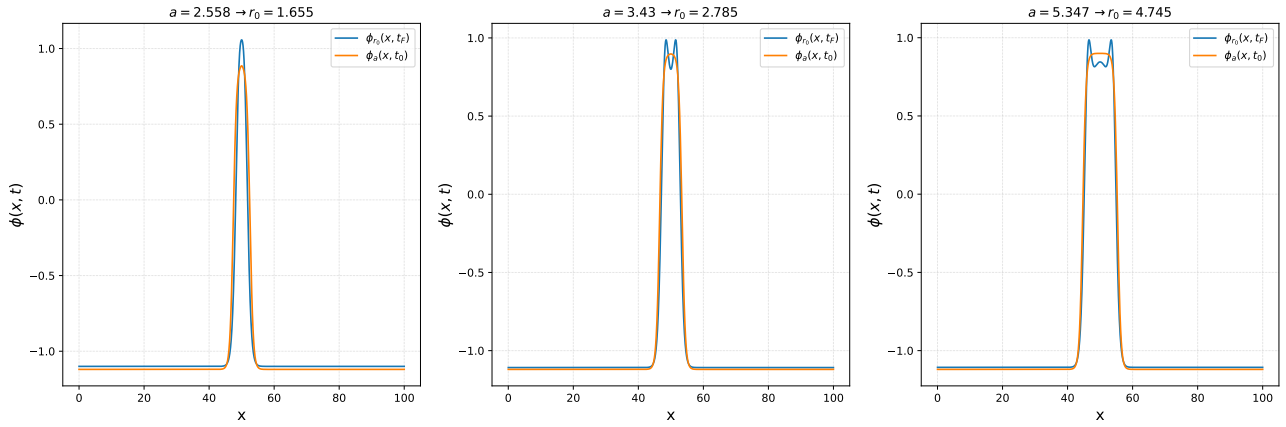

Figure 7.5: Comparison between the analytical guess profiles, Eq. (7.9) (orange), and the corresponding stationary branch profiles (blue), obtained numerically with *COMSOL*. In general, we can observe a one-dimensional stationary profile similar to those of the three-component McRD of Fig. 3.2, with the main difference being that the plateau value of the detachment zone is negative.

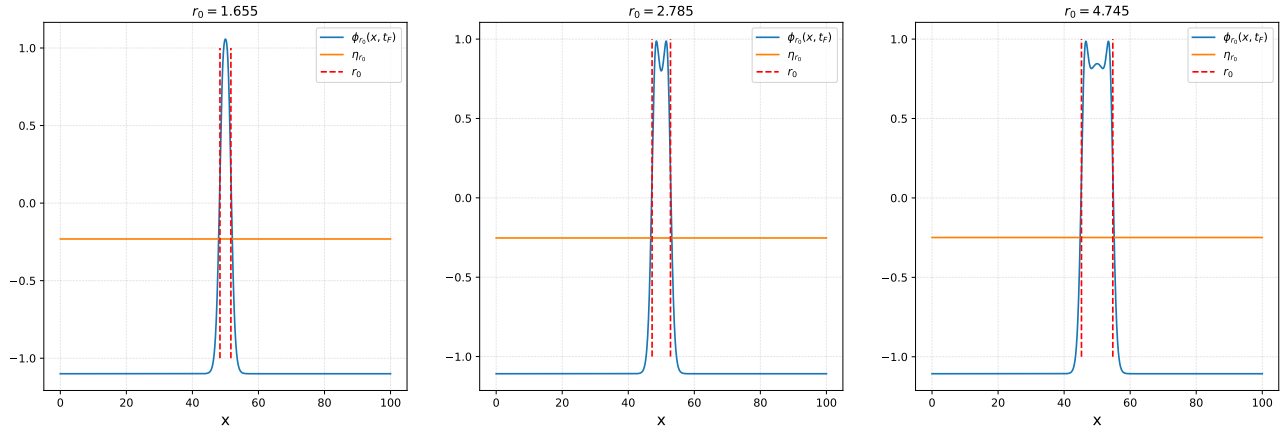

Figure 7.6: Stationary profiles for different values of the branch half-width r_0. For each stationary branch we report the constant mass redistribution potential (orange), and the "main" inflection points delimiting the attachment zone (red). It should be noted that, unlike the McRD, AMB$^-$ does not contain any reaction term.

7.2.2 Derivation of the dispersion relation

For the analytical derivation we adopt the same scheme already used in Secs. 3.2 and 3.4 for the three-component McRD model:

- Adiabatic approximation along x: we consider each transverse slice of the branch as a locally relaxed one-dimensional stationary profile parametrized by $r(y,t)$;
- Space divided in two parts: we consider the detachment (outer) region as a quasi-stationary reservoir and we perturb only the attachment (inner) region, meaning

$$\phi_{\text{att}}(x,y,t) \approx \phi_{r(y,t)}(x), \qquad \phi_{\text{det}}(x,y,t) \approx \phi_{r_0}(x); \tag{7.10}$$

- Harmonic perturbation: we linearize the system using a single sinusoidal perturbation amplitude,

$$r(y,t) = r_0 + \epsilon(t)\,\sin(qy), \qquad \epsilon(t) \sim e^{\sigma(q)t}. \tag{7.11}$$

  Unlike the three-component McRD model, AMB⁻ involves a single conserved field, so that the perturbation is fully parametrized by the branch half-width $r(y,t)$.

We now integrate the equation of the dynamics, Eq. (7.1), over the attachment zone,

$$\int_{-r}^{+r} dx\; \partial_t \phi_r(x) = M \int_{-r}^{+r} dx\; \nabla^2 \eta(x,y,t), \tag{7.12}$$

where we denote $r = r(y,t)$, and explicitly indicate the case $r = r_0$ only when needed.
The left-hand side is treated as in Eq. (3.20), using Leibniz's rule for differentiation under the integral sign with moving boundaries:

$$\int_{-r}^{+r} dx\; \partial_t \phi_r(x) = \frac{d}{dt}\int_{-r}^{+r} dx\; \phi_r(x) - 2\,\phi_r(x)\big|_{x=r}\,\partial_t r = \partial_t \Phi_r - 2\,\phi_r(x)\big|_{x=r}\,\partial_t r, \tag{7.13}$$

where we define the total mass inside the attachment zone as $\Phi_r \equiv \int_{-r}^{+r} dx\; \phi_r(x)$, similarly to what was done in Eq. (3.22). At leading order, using the harmonic ansatz of Eq. (7.11), we get

$$\partial_t \epsilon \left(\partial_r \Phi_r\big|_{r=r_0} - 2\phi_{r_0}(x)\big|_{x=r_0} \right) \sin(qy) = A\,\partial_t \epsilon\,\sin(qy), \tag{7.14}$$

where $A \equiv \partial_r \Phi_r|_{r=r_0} - 2\phi_{r_0}(x)|_{x=r_0}$ is a positive constant for fixed r_0. Figure 7.7 shows the numerical evidence for the stationary profiles considered.

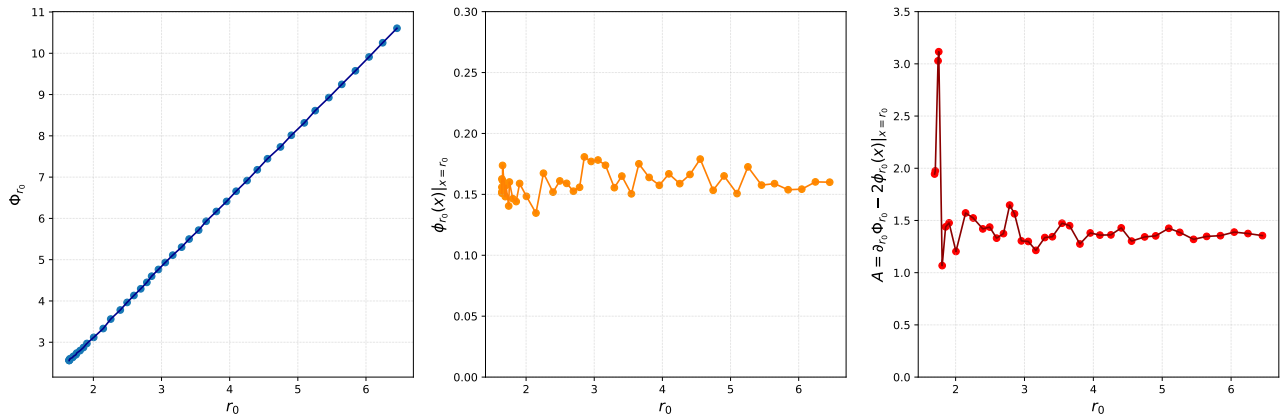

Figure 7.7: Numerical evidence for the positivity of A, obtained from 45 stationary profiles. **i)** Φ_{r_0} grows approximately linearly with the unperturbed branch half-width r_0. **ii)** The interface value $\phi_{r_0}(x)|_{x=r_0}$ remains approximately constant as r_0 varies. **iii)** The resulting quantity $A = \partial_{r_0}\Phi_{r_0} - 2\,\phi_{r_0}(x)|_{x=r_0}$ is strictly positive for all profiles considered.

Turning to the right-hand side, unlike in the McRD case, η is not an independent field and it is therefore not correct, in general, to treat the mass redistribution potential as constant along x within the attachment zone. To make this x-dependence explicit, we use the exact identity

$$\eta(x,y,t) = \underbrace{\eta^*(\phi_r) - \kappa(\phi_r)\,\partial_x^2\phi_r + K\,\partial_x^4\phi_r}_{\equiv\,\eta_r\ \text{(independent of } x)} + \underbrace{-\kappa(\phi_r)\,\partial_y^2\phi_r + 2K\,\partial_x^2\partial_y^2\phi_r + K\,\partial_y^4\phi_r}_{\equiv\,\delta\eta_r(x)}. \tag{7.15}$$

The first block is, by construction, exactly the combination appearing in the one-dimensional stationary condition, Eq. (7.7), and is therefore independent of x. The entire x-dependence of η is carried by $\delta\eta_r(x)$, which vanishes identically on the unperturbed branch $\phi_{r_0}(x)$.

Since $\nabla^2\eta_r = \partial_y^2\eta_r$, the right-hand side splits into three contributions:

$$\begin{aligned} M\int_{-r}^{+r} dx\ \nabla^2\eta(x,y,t) &= M\int_{-r}^{+r} dx\ \left[\partial_y^2\eta_r + \partial_x^2\delta\eta_r(x) + \partial_y^2\delta\eta_r(x)\right] \\ &= M\left[\underbrace{2r\,\partial_y^2\eta_r}_{\text{(i)}} + \underbrace{\partial_x\delta\eta_r(x)\big|_{-r}^{+r}}_{\text{(ii)}} + \underbrace{\int_{-r}^{+r} dx\,\partial_y^2\delta\eta_r(x)}_{\text{(iii)}}\right], \end{aligned} \tag{7.16}$$

each evaluated, to leading order in ϵ, on the unperturbed profile $\phi_{r_0}(x)$ using the linearization rule

$$\partial_y^k\phi_r = \partial_r\phi_r\big|_{r=r_0}\,\partial_y^k r + \mathcal{O}(\epsilon^2), \qquad k = 1,2,3,\dots \tag{7.17}$$

Since $\phi_r(x)$ depends on y only through the slowly varying branch parameter $r(y,t)$, repeated derivatives with respect to y can be expanded using the chain rule. At linear order, every term containing two or more factors of $\partial_y^j r$ is of order $\mathcal{O}(\epsilon^2)$ and can therefore be neglected. For example, at $k=2$,

$$\partial_y^2\phi_r = \underbrace{\partial_r^2\phi_r\,(\partial_y r)^2}_{\mathcal{O}(\epsilon^2)} + \underbrace{\partial_r\phi_r\,\partial_y^2 r}_{\mathcal{O}(\epsilon)}. \tag{7.18}$$

The same argument applies to higher derivatives, yielding to the rule in Eq. (7.17) where evaluating $\partial_r\phi_r$ at $r=r_0$ is also sufficient at linear order. Indeed, Taylor-expanding around $r=r_0$, we get

$$\partial_r\phi_r = \partial_r\phi_r\big|_{r=r_0} + \partial_r^2\phi_r\big|_{r=r_0}(r-r_0) + \cdots = \partial_r\phi_r\big|_{r=r_0} + \mathcal{O}(\epsilon), \tag{7.19}$$

because $r - r_0 = \epsilon\sin(qy)$ is itself $\mathcal{O}(\epsilon)$. The corrections to zeroth-order term are multiplied by $\partial_y^k r = \mathcal{O}(\epsilon)$, giving only $\mathcal{O}(\epsilon^2)$ contributions, and can likewise be dropped. At leading order, only $\partial_r\phi_r|_{r=r_0}\,\partial_y^k r$ term remains and Eq. (7.17) therefore provides the required relation.

(i) x-independent term:
Since η_r depends on y only through $r(y,t)$, the chain rule gives directly

$$2r\,\partial_y^2\eta_r = 2r_0\,\partial_r\eta_r\big|_{r=r_0}\,\partial_y^2 r + \mathcal{O}(\epsilon^2) \implies -q^2\,2r_0\,\partial_r\eta_r\big|_{r=r_0}\,\epsilon\sin(qy). \tag{7.20}$$

(ii) Boundary terms:
The next step is to determine the x-derivative of $\delta\eta_r(x)$ at leading order:

$$\begin{aligned} \partial_x\,\delta\eta_r(x) &= \partial_x\left[-\kappa(\phi_r)\partial_y^2\phi_r + 2K\partial_x^2\partial_y^2\phi_r + K\partial_y^4\phi_r\right] \\ &= \partial_x[-\kappa(\phi_{r_0})\,\partial_r\phi_r\big|_{r=r_0}\,\partial_y^2 r + 2K\partial_r\partial_x^2\phi_r\big|_{r=r_0}\,\partial_y^2 r + K\partial_r\phi_r\big|_{r=r_0}\,\partial_y^4 r + \mathcal{O}(\epsilon^2)] \\ &= \left[-\partial_x\kappa(\phi_{r_0})\,\partial_{r_0}\phi_{r_0} - \kappa(\phi_{r_0})\partial_{r_0}\partial_x\phi_{r_0} + 2K\partial_{r_0}\partial_x^3\phi_{r_0}\right]\partial_y^2 r + K\partial_{r_0}\partial_x\phi_{r_0}\,\partial_y^4 r + \mathcal{O}(\epsilon^2). \end{aligned} \tag{7.21}$$

Evaluating the expression at the two boundaries and retaining only the leading-order contribution allows us to replace the perturbed boundaries $x = \pm r(y,t)$ by $x = \pm r_0$. We therefore obtain

$$\partial_x\delta\eta_r(x)\big|_{-r}^{+r} \doteq \left[-\partial_x\kappa(\phi_{r_0})\,\partial_{r_0}\phi_{r_0} - \kappa(\phi_{r_0})\partial_{r_0}\partial_x\phi_{r_0} + 2K\partial_{r_0}\partial_x^3\phi_{r_0}\right]_{-r_0}^{+r_0}\,\partial_y^2 r + \left[K\partial_{r_0}\partial_x\phi_{r_0}\right]_{-r_0}^{+r_0}\,\partial_y^4 r. \tag{7.22}$$

Since the stationary branch profile is assumed to be symmetric, $\phi_{r_0}(x)|_{x=-r_0} = \phi_{r_0}(x)|_{x=r_0}$, and differentiation with respect to r_0 preserves the parity, it follows that

$$\partial_{r_0}\partial_x^k\phi_{r_0}\big|_{x=-r_0} = (-1)^k\,\partial_{r_0}\partial_x^k\phi_{r_0}\big|_{x=r_0}, \qquad k=0,1,2,\dots\,. \tag{7.23}$$

Moreover, using the chain rule, the first term can be rewritten as

$$\partial_x\kappa(\phi_{r_0}) = \kappa'(\phi_{r_0})\,\partial_x\phi_{r_0}, \tag{7.24}$$

which is odd under $x \to -x$.
Consequently, each term inside the boundary contribution is odd, so that the jump across the interval can be written as twice the value evaluated at the right boundary $x = r_0$.

For notation simplicity, we introduce two quantities which are constant for fixed r_0:

$$\begin{aligned} B &\equiv \left[2\,\kappa'(\phi_{r_0})\,\partial_x\phi_{r_0}\,\partial_{r_0}\phi_{r_0} + 2\,\kappa(\phi_{r_0})\,\partial_{r_0}\partial_x\phi_{r_0} - 4K\,\partial_{r_0}\partial_x^3\phi_{r_0}\right]_{x=r_0}, \\ C &\equiv 2K\,\partial_{r_0}\partial_x\phi_{r_0}\Big|_{x=r_0}. \end{aligned} \tag{7.25}$$

With these definitions, contribution (ii) becomes

$$\partial_x\delta\eta_r(x)\big|_{-r}^{+r} = -B\,\partial_y^2 r + C\,\partial_y^4 r + \mathcal{O}(\epsilon^2) \implies q^2\left[B + C\,q^2\right]\epsilon\sin(qy) \tag{7.26}$$

(iii) Integral term:
Substituting the definition of $\delta\eta_r(x)$, Eq. (7.15), and linearizing each term with the rule (7.17) yields

$$\begin{aligned} \partial_y^2\,\delta\eta_r(x) &= \partial_y^2\left[-\kappa(\phi_r)\partial_y^2\phi_r + 2K\partial_x^2\partial_y^2\phi_r + K\partial_y^4\phi_r\right] \\ &= \partial_y^2[-\kappa(\phi_{r_0})\,\partial_r\phi_r\big|_{r=r_0}\,\partial_y^2 r + 2K\partial_r\partial_x^2\phi_r\big|_{r=r_0}\,\partial_y^2 r + K\partial_r\phi_r\big|_{r=r_0}\,\partial_y^4 r + \mathcal{O}(\epsilon^2)] \\ &= -\kappa(\phi_{r_0})\,\partial_{r_0}\phi_{r_0}\,\partial_y^4 r + 2K\partial_{r_0}\partial_x^2\phi_{r_0}\,\partial_y^4 r + K\partial_{r_0}\phi_{_0}r\,\partial_y^6 r + \mathcal{O}(\epsilon^2), \end{aligned} \tag{7.27}$$

where in the second step $\kappa(\phi_r)$ is evaluated at $r = r_0$ because any further correction of the Taylor expansion would only contribute at $\mathcal{O}(\epsilon^2)$ and in the third step ∂_y^2 acts only on $\partial_y^2 r$ and $\partial_y^4 r$, raising each power by two.

Integrating over the attachment zone, the integration limits can also be replaced by r_0 because the integrand is already $\mathcal{O}(\epsilon)$, so extending or shrinking the domain by $r - r_0 = \mathcal{O}(\epsilon)$ changes the result only at $\mathcal{O}(\epsilon^2)$. Therefore, at leading order the integral reads

$$\int_{-r}^{+r} dx\;\partial_y^2\delta\eta_r(x) \doteq \partial_y^4 r\int_{-r_0}^{+r_0} dx\left[-\kappa(\phi_{r_0})\partial_{r_0}\phi_{r_0} + 2K\partial_{r_0}\partial_x^2\phi_{r_0}\right] + K\,\partial_y^6 r\int_{-r_0}^{+r_0} dx\;\partial_{r_0}\phi_{r_0}. \tag{7.28}$$

The last integral is, by Leibniz's rule, exactly the quantity A already defined in Eq. (7.14). For the remaining integral, the piece $\int_{-r_0}^{+r_0} dx\;2K\partial_{r_0}\partial_x^2\phi_{r_0} = 4K\,\partial_{r_0}\partial_x\phi_{r_0}|_{x=r_0} = 2C$ is precisely related to the boundary contribution introduced in (ii), while the other part is an irreducible integral, which we define as

$$I \equiv \int_{-r_0}^{+r_0} dx\;\;-\kappa(\phi_{r_0})\,\partial_{r_0}\phi_{r_0}. \tag{7.29}$$

The quantity I therefore represents a bulk contribution associated with the dependence of the curvature-dependent coefficient $\kappa(\phi_{r_0})$ on the stationary profile. We keep I in integral form, since applying the exact identity $\kappa(\phi_{r_0})\,\partial_{r_0}\phi_{r_0} = \tanh(\phi_0 - \phi_{r_0})\,\partial_{r_0}\phi_{r_0} = -\partial_{r_0}\ln\cosh(\phi_0 - \phi_{r_0})$ and Leibniz's rule once more would only replace the integral by additional boundary terms without providing a useful further simplification.
With this definition, contribution (iii) reads

$$\int_{-r}^{+r} dx\;\partial_y^2\delta\eta_r(x) = (I+2C)\;\partial_y^4 r + KA\,\partial_y^6 r + \mathcal{O}(\epsilon^2) \implies q^4\left[(I+2C) - q^2\,KA\right]\epsilon\sin(qy) \tag{7.30}$$

Collecting Eqs. (7.20), (7.26) and (7.30) we get the linearized right-hand side of Eq. (7.12):

$$M\int_{-r}^{+r} dx\;\nabla^2\eta(x,y,t) \doteq M\left[\left(-2r_0\partial_r\eta_r\big|_{r=r_0} + B\right)\,q^2 + (I+3C)\,q^4 - KA\,q^6\right]\epsilon\sin(qy). \tag{7.31}$$

Dispersion relation. Combining the results for the left and right hand side, respectively Eq. (7.14) and (7.31), yields

$$A\,\partial_t\epsilon = M\left[\left(-2r_0\,\partial_r\eta_r\big|_{r=r_0} + B\right)\,q^2 + (I+3C)\,q^4 - KA\,q^6\right]\epsilon, \tag{7.32}$$

thus the dispersion relation reads

$$\sigma(q) = \frac{M}{A}C_2\,q^2 + \frac{M}{A}C_4\,q^4 - MK\,q^6, \tag{7.33}$$

where $C_2 \equiv -2r_0\partial_r\eta_r|_{r=r_0} + B$, and $C_4 \equiv I + 3C$.

Since M and K are positive constants, the leading term at large q, i.e. $-MK\,q^6$, is always negative. Therefore Eq. (7.33) represents a physically acceptable growth rate for every value of the control parameters with $\sigma(q \to \infty) \to -\infty$. This property follows directly from the structure of the dispersion relation and does not require any further evaluation of the stationary profiles.

We now analyze the remaining coefficients, starting from the q^4 contribution and proceeding towards the long-wavelength q^2 term. Where possible, we first use the properties of the stationary profiles to identify the dominant contributions and then compare these predictions with the numerical evaluation over the full set of one-dimensional stationary solutions.

The coefficient $C_4 = I + 3C$ is found to be negative for all branches considered. To understand its origin, we first note that increasing r_0 primarily shifts the interface outwards, so that $\partial_{r_0}\phi_{r_0}(x)$ develops a maximum around the interface at $x = \pm r_0$. Consequently, $\partial_x\partial_{r_0}\phi_{r_0}|_{x=r_0} \simeq 0$ which makes the boundary contribution C negligible. The q^4 coefficient is therefore expected to be dominated by the integral contribution I.

The numerical evaluation in Fig. 7.8 confirms this expectation and moreover shows that I remains negative for all stationary branches, consequently yielding $C_4 = I + 3C \simeq I < 0$.
The q^4 contribution is thus always stabilizing and the dispersion relation of Eq. (7.33) does not support a conserved Type-I instability. Indeed, in this case, a positive q^4 coefficient would provide the leading destabilizing contribution when the q^2 coefficient is negative. The only possible instability is therefore of Type II, occurring when the coefficient C_2 is positive.

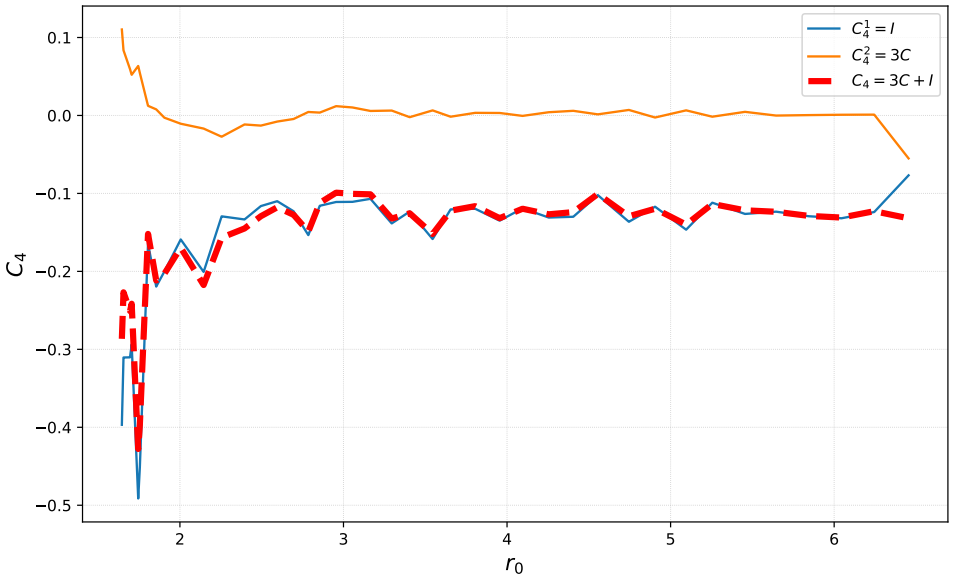

Figure 7.8: Contributions to $C_4 = I + 3C$ as a function of the branch half-width r_0: the irreducible integral I (blue) defined in Eq. (7.29), the boundary term $3C = 6K\partial_{r_0}\partial_x\phi_{r_0}|_{x=r_0}$ (orange) defined in Eq. (7.25), together with the total C_4 (dashed red). The integral I dominates and remains negative for all stationary solutions, so the q^4 term in Eq. (7.33) is always negative and therefore the dispersion relation never supports a conserved Type I instability.

We next turn to the boundary contribution B, which enters the coefficient of the q^2 term. Its structure can again be analyzed by considering the properties of the stationary profiles. The contribution $-\kappa(\phi_{r_0})\partial_{r_0}\phi_{r_0}|_{x=r_0}$ is negligible because it contains the derivative $\partial_x\partial_{r_0}\phi_{r_0}|_{x=r_0} \simeq 0$. Then we find numerically that $4K\,\partial_{r_0}\partial_x^3\phi_{r_0}|_{x=r_0}$ is small compared with the dominant contribution associated with the interface displacement term, $2\,\kappa'(\phi_{r_0})\,\partial_x\phi_{r_0}\,\partial_{r_0}\phi_{r_0}$. The sign of this dominant contribution can be understood from the numerical observation that the value of the stationary profile at the interface remains approximately constant as r_0 varies, as shown in Fig.7.7, panel ii). Taking the total derivative of this quantity with respect to r_0 therefore gives

$$\frac{d}{dr_0}\phi_{r_0}(x=r_0) = \partial_{r_0}\phi_{r_0}\big|_{x=r_0} + \partial_x\phi_{r_0}\big|_{x=r_0} \simeq 0 \implies \partial_{r_0}\phi_{r_0}\big|_{x=r_0} \simeq -\partial_x\phi_{r_0}\big|_{x=r_0}. \tag{7.34}$$

Consequently, the dominant contribution to B becomes

$$\left[2\,\kappa'(\phi_{r_0})\,\partial_x\phi_{r_0}\,\partial_{r_0}\phi_{r_0}\right]_{x=r_0} \simeq \left[-2\,\kappa'(\phi_{r_0})\,\left[\partial_x\phi_{r_0}\right]^2\right]_{x=r_0} = 2\,\mathrm{sech}^2\left(\phi_0 - \phi_{r_0}(r_0)\right)\left[\partial_x\phi_{r_0}(r_0)\right]^2 \geq 0. \tag{7.35}$$

Thus, the dominant interface contribution to B is positive for every stationary branch considered. The decomposition of the different contributions to B is illustrated in Fig. 7.9.

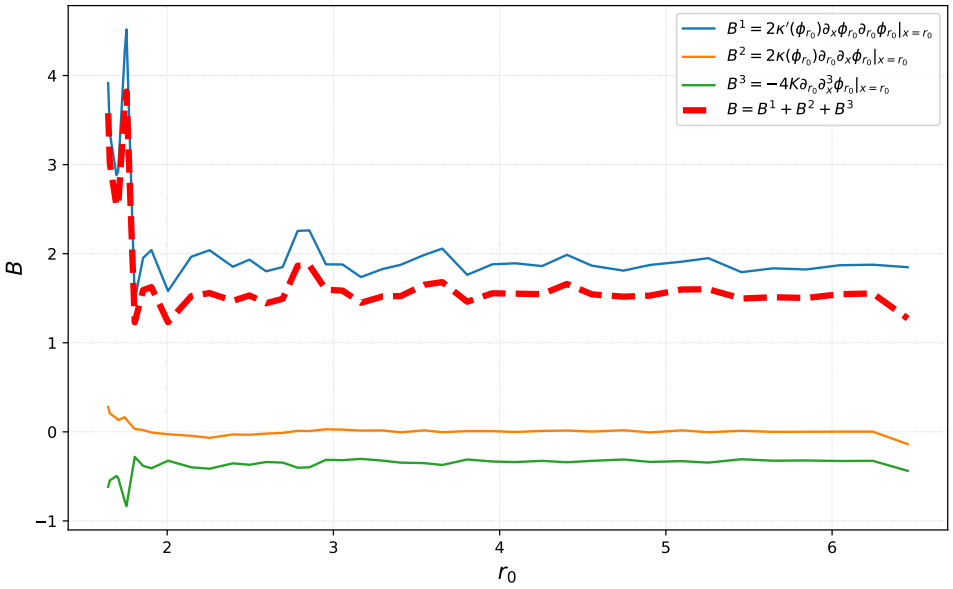

Figure 7.9: Contributions to B defined in Eq. (7.25) as functions of the branch half-width r_0: the interface dominant term $B^1 = 2\kappa'(\phi_{r_0})\partial_x\phi_{r_0}\partial_{r_0}\phi_{r_0}|_{x=r_0}$ (blue), and the two small mixed-derivative terms $B^2 = 2\kappa(\phi_{r_0})\partial_{r_0}\partial_x\phi_{r_0}|_{x=r_0}$ (orange) and $B^3 = -4K\partial_{r_0}\partial_x^3\phi_{r_0}|_{x=r_0}$ (green), together with their sum B (dashed red). The positive boundary term B^1 dominates, hence B is positive for all branch considered.

The above analysis fixes the sign of the higher-order terms and shows that the q^4 contribution is always stabilizing, while the boundary correction B gives a positive contribution to the long-wavelength coefficient. We can therefore examine numerically the complete coefficient $C_2 = -2r_0\,\partial_r\eta_r|_{r=r_0} + B$ which ultimately determines the onset of the long-wavelength instability.

At this point, however, the analyses reveals a qualitative discrepancy with the numerical dynamics. In fact, C_2 is found to be positive for all stationary profiles considered because the boundary contribution B dominates over the first term, as shown in Fig. 7.10.

The resulting prediction would imply $\sigma(q \to 0^+) > 0$ for all branches, meaning that all stationary branches are unstable (Type II instability) to a long-wavelength pearling perturbation. This is in qualitative disagreement with the two-dimensional simulations, where pearling is observed only within a finite range of r_0, while branches outside this range remain stable.

By contrast, neglecting the boundary contribution B gives a stability criterion controlled by the sign of $\partial_r\eta_r|_{r=r_0}$, which is consistent with the numerical onset of the instability (see Fig 7.14).

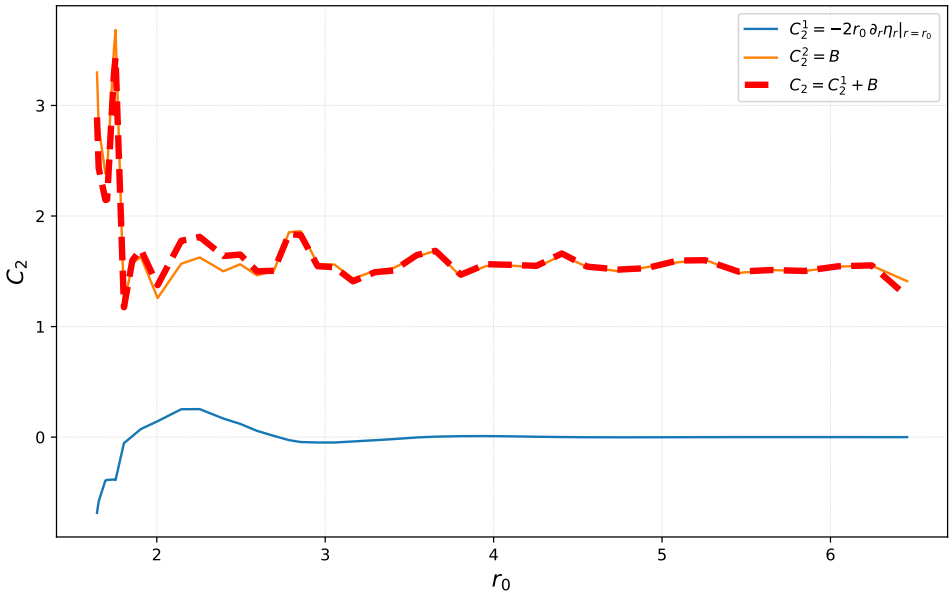

Figure 7.10: Comparison between the corrected coefficient $C_2 = -2r_0\partial_r\eta_r|_{r=r_0} + B$ (dashed red), together with the coefficient $-2r_0\,\partial_r\eta_r|_{r=r_0}$ (blue) and B (orange) alone , as functions of r_0. Only the naive coefficient changes sign over the range of r_0 explored, consistently with the two-dimensional simulations; the corrected C_2 remains positive throughout, reflecting the always-positive, dominant correction B identified above.

We interpret this discrepancy between theoretical result and numerical data as a consequence of the simplified assumption we made in considering the detachment zone as frozen to the unperturbed profile, $\phi_{\rm det}(x,y,t) \approx \phi_{r_0}(x)$. All boundary terms, particularly B, arise from $\int_{-r}^{+r} dx\,\partial_x^2\delta\eta_r(x) = [\partial_x\delta\eta_r(x)]_{-r}^{+r}$, which represents the net flux of the mass redistribution potential across the interface. By freezing the detachment region, the present ansatz does not allow the outer solution to respond to this flux, which is therefore likely overestimated.
As already mentioned in Sec. 3.2, a more consistent treatment would allow the detachment region to respond to the perturbation while maintaining the smooth matching of the field across the attachment–detachment interface,

$$\phi_{\rm det}(x,y,t) \approx \phi_{r_0}(x) + \delta\phi(x,y,t). \tag{7.36}$$

Such a correction would modify the flux across the interface and introduce additional boundary contributions when the equation of motion is integrated over the attachment region. We therefore expect the coefficient B obtained with the frozen-detachment ansatz to be modified, and potentially reduced, once the response of the outer region is taken into account. However, determining their magnitude and whether they cancel B completely would require solving the perturbed detachment region explicitly, which is left for future work.

This observation motivates a simplified calculation in which we neglect the x-dependence of the mass redistribution potential. The aim is to isolate the contribution associated with the variation of the one-dimensional stationary branch and to assess whether it reproduces the long-wavelength instability criterion observed in the simulations.

7.2.3 Simplified derivation

Motivated by the discussion above, we consider the approximation

$$\eta(x, y, t) \approx \eta_{r(y,t)}. \tag{7.37}$$

This assumption is not justified a priori, since in AMB$^-$ the redistribution potential is a functional of ϕ and its spatial derivatives rather than an independent field. It is therefore introduced here as an effective approximation that isolates the contribution of the stationary branch variation.

Under this assumption only contribution i) of Eq. (7.16) survives. The integrated equation therefore gives

$$A\,\partial_t \epsilon = -2Mr_0\,\partial_r \eta_r\big|_{r=r_0}\, q^2\,\epsilon, \tag{7.38}$$

and hence

$$\sigma_{\text{approx}}(q) = -\frac{M}{A}\,2r_0\,\partial_r \eta_r\big|_{r=r_0}\, q^2. \tag{7.39}$$

The main result of Eq. (7.39) lies in the sign of the leading long-wavelength contribution, in particular,

$$\partial_r \eta_r\big|_{r=r_0} < 0 \quad \Longrightarrow \quad \sigma(q \to 0^+) > 0. \tag{7.40}$$

This criterion agrees well with the onset observed in the two-dimensional simulations and provides the same physical interpretation as obtained for the McRD: a locally wider region with lower redistribution potential attracts mass from neighboring regions, thereby amplifying the initial perturbation.
The simplified relation should nevertheless be regarded as an effective long-wavelength description rather than a complete dispersion relation. In particular, it contains no short-wavelength regularization and therefore cannot determine the selected wavelength or maximum growth rate. These quantities depend on the higher-order terms neglected by the approximation and require a treatment of the transverse response of the detachment region.

7.2.4 Numerical results and comparison

Two-dimensional simulations were performed in *COMSOL Multiphysics* to test the theoretical predictions of the previous section. As already done for the McRD model, for computational simplicity the initial condition of each two-dimensional run is set to a straight branch obtained by extruding the analytical guess profile $\phi_a(x)$, Eq. (7.9), rather than the numerically relaxed one-dimensional stationary profile $\phi_{r_0}(x)$. In principle, this approach relies on a timescale separation between the fast one-dimensional relaxation toward the unperturbed branch profile and the slower onset of the pearling instability.
However, as shown in Figs. 7.11 and 7.12, this timescale separation is not as large as that observed in the McRD model: pearling modulations develop before the profile has fully relaxed to its exact stationary shape. Despite this, the two initialization strategies are found to produce comparable outcomes regarding both the pearling onset and the subsequent two-dimensional long-time dynamics (Fig. 7.11). Since our primary goal for AMB$^-$ is to map out the instability boundaries rather than to perform quantitative measurements of physical rates or characteristic times, adopting the analytical guess provides a suitable and computationally efficient simplification.

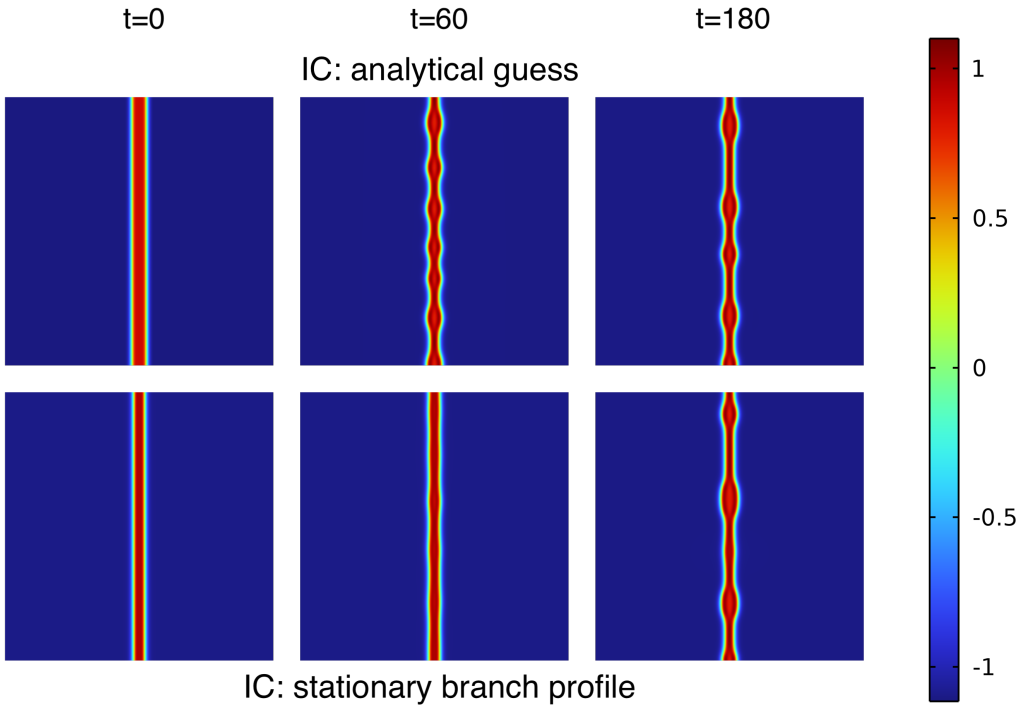

Figure 7.11: Comparison between spatial-temporal dynamics of the AMB$^-$ initialized with analytic guess profile (upper row) and unperturbed stationary branch (bottom row). Although pearling sets in before the guess profile fully relaxes, both initialization protocols yield identical long-time spatial structures and comparable onset behavior. Since our focus for AMB$^-$ is to verify the occurrence of the instability rather than extract precise kinetic timescales, using the analytical guess serves as a reliable and computationally convenient approximation.

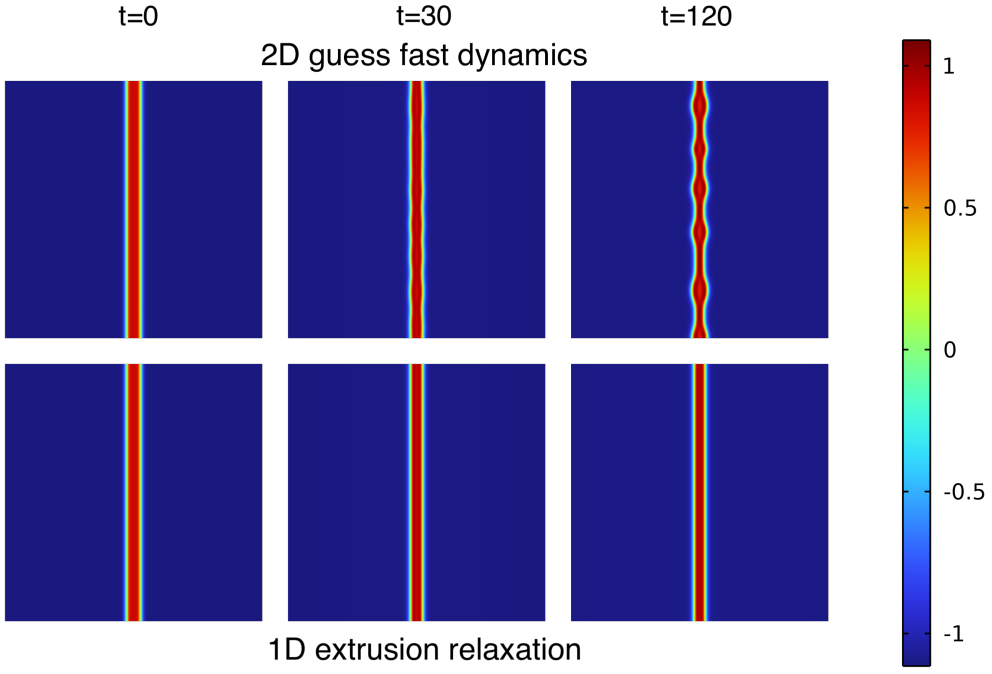

Figure 7.12: Early-time relaxation dynamics of the two-dimensional simulation initialized with the analytical guess profile (top row) compared with the corresponding one-dimensional simulation, extruded into 2D (bottom row). While mass redistribution for $t < 30$ occurs predominantly along x-direction, the timescale separation between 1D relaxation and the onset of the pearling instability is not fully complete. As a result, transverse modulations set in at $t \approx 30$ before the profile has fully relaxed to the exact 1D stationary shape (attained at $t = 120$ in the bottom row). Despite this partial overlap in timescales, the long-time 2D dynamics remain closely comparable, justifying the use of the analytical guess for numerical convenience.

Unlike the McRD case, in the AMB$^-$ no pearling event is observed to terminate in a fully developed sequence of separated dots, since the smallest accessible branch width always falls within the linearly stable interval. What is instead observed is the analogue of Fig 4.6 in the McRD chapter: the instability sets in and proceeds until the local branch width, decreasing as mass is transferred into the growing pearls, enters the stable interval; at that point the pearling mechanism stalls, and the subsequent dynamics is governed by the interaction between the residual branch and the dots already formed. With our parameter choice, the observed evolution is a coarsening process, whereby smaller dots are progressively absorbed by larger ones until, at long times, a single dot remains. An example of this dynamics is shown in Fig. 7.13. In the whole space of stationary solutions we observe only stable branches or this instability mechanism just described.

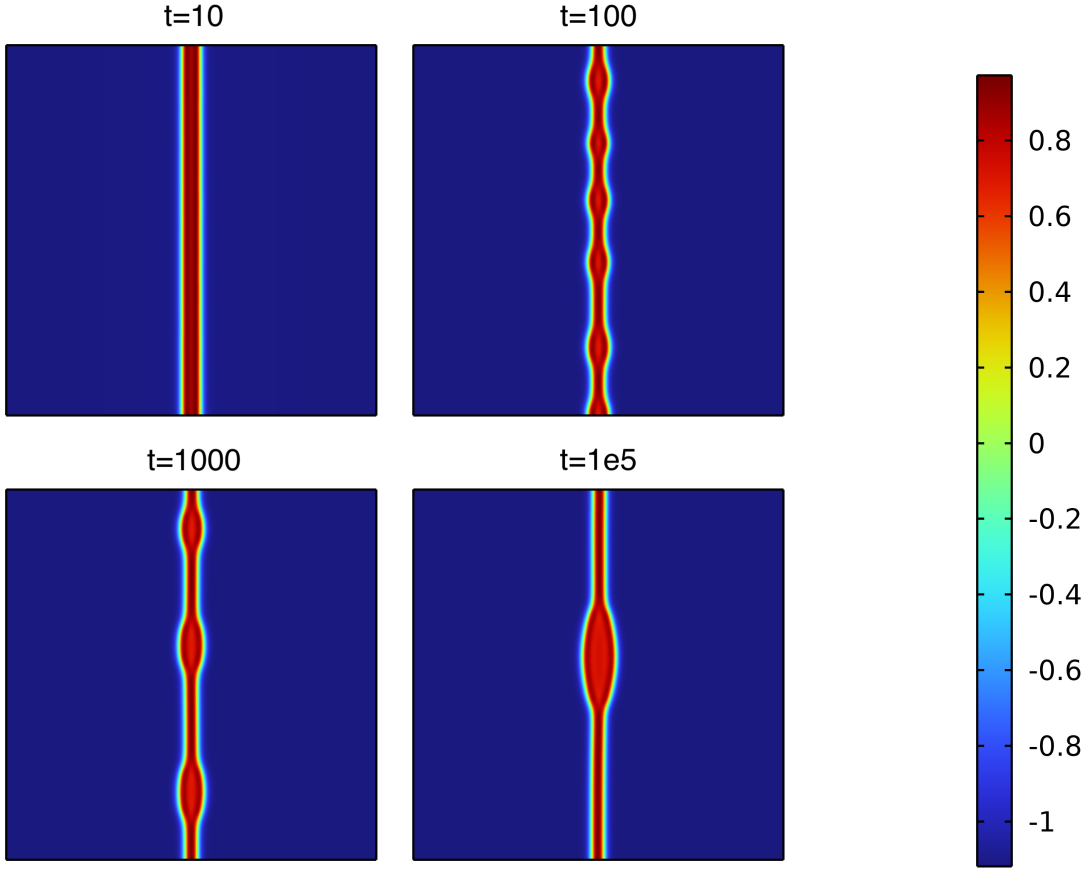

Figure 7.13: Example of pearling instability in the AMB$^-$. The initial guess profile corresponds to $a = 2.893$ ($\bar{\phi} = -1.00$). On short timescales the profile relaxes almost to a non-monotonic stationary branch of half-width $r_0 = 2.145$. Before relaxing completely, the pearling instability begins already at early times ($t \approx 50$) and after the first mass redistribution event a new monotonic branch appears midway between two dots ($t = 100$). Beyond this point, perturbation theory is no longer able to describe the dynamics which appears to be coarsening. In the final snapshots, $t = 10^3$ and $t = 10^5$, smaller points are absorbed by larger ones until only a single point survives coexisting with the thinner branch of stable width.

Finally, in Fig. 7.14 is summarized the comparison between simulations and the simplified theory.

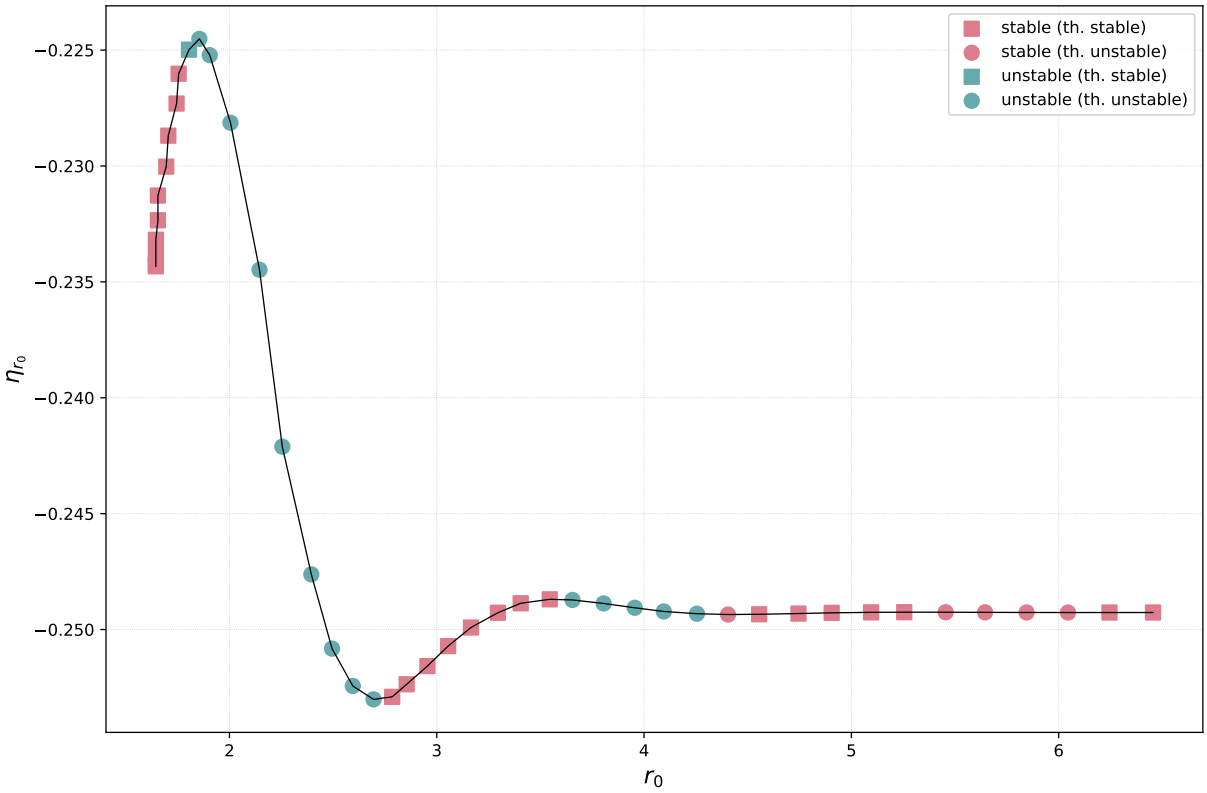

Figure 7.14: Stationary mass redistribution potential η_{r_0} as a function of the numerical branch half-width r_0. Numerical points are shown as circles when the slope is positive and as squares when it is negative. Colors correspond to two-dimensional *COMSOL* simulations: unstable branches undergoing pearling are shown in pink, stable branches in green. The agreement between the sign of the slope and the outcome of the simulations suggests the validity of the analytical criterion based on the sign of $\partial_r \eta_r|_{r=r_0}$.

Thus, the asymptotic analysis provides two complementary results. The full calculation exposes the higher-order structure of the AMB$^-$ dispersion relation and identifies the boundary flux generated by the frozen-detachment approximation as the source of the discrepancy with the numerical stability diagram. The simplified calculation, while not sufficient to determine the full finite-q dispersion relation, isolates the long-wavelength contribution proportional to $\partial_r \eta_r|_{r=r_0}$ and reproduces the observed stability criterion. A complete quantitative description of the growth rate would require extending the asymptotic ansatz to the detachment region and accounting for its response to the interfacial flux.

Chapter 8

Conclusions

In this thesis, we studied the pearling instability, a general mechanism through which a straight branch pattern loses stability and breaks up into a sequence of aligned dots. Our results provide evidence that pearling is not specific to the three-component mass-conserving reaction-diffusion model considered (minimal coarse-grained model inspired by the MinD cycle of the Min system), but also occurs in other mass-conserving field theories, such as Active Model B^-. This suggests that pearling represents a general mechanism underlying the destabilization of extended structures in mass-conserving pattern-forming systems.

To describe this instability, we developed a semi-analytical approach based on the one-dimensional structure of the unperturbed stationary branch and on the separation of space into attachment and detachment regions. By combining this description with an asymptotic matching procedure, we obtained a dispersion relation that correctly predicts the onset of the pearling instability. The comparison with numerical simulations therefore demonstrates that for the three-component model the proposed framework captures the essential mechanism responsible for the loss of stability. At the same time, the discrepancies in the predicted characteristic time and length scales indicate that the present approximation is not sufficient for a fully quantitative description of the instability.

We then explored the applicability of this theoretical framework to Active Model B^-. While a simplified approximation is sufficient to identify the onset of the instability, it leads to an unphysical dispersion relation. The complete formulation, on the other hand, requires further correction, as it currently predicts an unstable regime throughout the parameter space. These findings indicate that while the core ideas of the method may extend to Active Model B^- and other mass-conserving field theories, additional theoretical corrections are required to achieve a consistent description.

Therefore, a natural extension for improving the present theory consists in introducing the perturbation also in the detachment region and imposing continuity of the fields at the interface. The resulting problem should take the form of a self-consistent transcendental eigenvalue problem, whose solution is expected to provide a consistent description of the instability spectrum and of its characteristic length and time scales. Applying the resulting framework to other mass-conserving field theories, such as the conserved Swift–Hohenberg model and Active Model H^-, would provide a further test of the generality of the proposed approach.

Beyond pearling, a broader direction is to develop a unified theoretical description of the pattern transitions observed in the three-component model of the Min system. In particular, understanding the mechanisms underlying transitions between dots, lines, and foams would provide a framework for describing the different morphological states and their transitions across the parameter space. Such a framework, eventually complemented by stochastic effects, could help connect the theoretical description of mass-conserving pattern formation with the rich phenomenology observed in biological systems.

Bibliography

[1] Fridtjof Brauns, Leila Iñigo de la Cruz, Werner K-G Daalman, Ilse de Bruin, Jacob Halatek, Liedewij Laan, and Erwin Frey. Redundancy and the role of protein copy numbers in the cell polarization machinery of budding yeast. *Nature Communications*, 14(1):6504, 2023.

[2] Michael E Cates. *Active field theories*. April, 2019.

[3] KR Elder and Martin Grant. Modeling elastic and plastic deformations in nonequilibrium processing using phase field crystals. *Physical Review E—Statistical, Nonlinear, and Soft Matter Physics*, 70(5):051605, 2004.

[4] Erwin Frey and Henrik Weyer. Pattern formation beyond turing: Physical principles of mass-conserving reaction–diffusion systems. *Annual Review of Biophysics*, 55, 2026.

[5] Philipp Glock, Beatrice Ramm, Tamara Heermann, Simon Kretschmer, Jakob Schweizer, Jonas Mücksch, Gökberk Alagöz, and Petra Schwille. Stationary patterns in a two-protein reaction-diffusion system. *ACS synthetic biology*, 8(1):148–157, 2018.

[6] Jacob Halatek and Erwin Frey. Highly canalized mind transfer and mine sequestration explain the origin of robust mincde-protein dynamics. *Cell reports*, 1(6):741–752, 2012.

[7] Zonglin Hu and Joe Lutkenhaus. Topological regulation of cell division in escherichia coli involves rapid pole to pole oscillation of the division inhibitor minc under the control of mind and mine. *Molecular microbiology*, 34(1):82–90, 1999.

[8] Pil Jung Kang, Anthony Sanson, Bongyong Lee, and Hay-Oak Park. A gdp/gtp exchange factor involved in linking a spatial landmark to cell polarity. *Science*, 292(5520):1376–1378, 2001.

[9] Martin Loose, Elisabeth Fischer-Friedrich, Jonas Ries, Karsten Kruse, and Petra Schwille. Spatial regulators for bacterial cell division self-organize into surface waves in vitro. *Science*, 320(5877):789–792, 2008.

[10] David M Raskin and Piet AJ de Boer. Minde-dependent pole-to-pole oscillation of division inhibitor minc in escherichia coli. *Journal of bacteriology*, 181(20):6419–6424, 1999.

[11] Ziyuan Ren, Henrik Weyer, Michael Sandler, Laeschkir Würthner, Haochen Fu, Chanin B. Tangtartharakul, Dongyang Li, Cindy Sou, Daniel Villarreal, Judy E. Kim, Erwin Frey, and Suckjoon Jun. Robust and resource-optimal dynamic pattern formation of min proteins in vivo. *Nature Physics*, 21(7):1160–1169, 2025.

[12] Uwe Thiele, Andrew J Archer, Mark J Robbins, Hector Gomez, and Edgar Knobloch. Localized states in the conserved swift-hohenberg equation with cubic nonlinearity. *Physical Review E—Statistical, Nonlinear, and Soft Matter Physics*, 87(4):042915, 2013.

[13] Elsen Tjhung, Cesare Nardini, and Michael E Cates. Cluster phases and bubbly phase separation in active fluids: Reversal of the ostwald process. *Physical Review X*, 8(3):031080, 2018.

[14] Davide Toffenetti, B Nettuno, H Weyer, and E Frey. Active model b^- from mass-conserving reaction-diffusion systems. *arXiv preprint arXiv:2605.15903*, 2026.

[15] Alan Mathison Turing. The chemical basis of morphogenesis. *Bulletin of mathematical biology*, 52(1):153–197, 1990.

[16] Henrik Weyer, Fridtjof Brauns, and Erwin Frey. Coarsening and wavelength selection far from equilibrium: A unifying framework based on singular perturbation theory. *Physical Review E*, 108(6):064202, 2023.

[17] Henrik Weyer, Tobias A Roth, and Erwin Frey. Protein pattern morphology and dynamics emerging from effective interfacial tension. *Nature Physics*, 22(1):94–102, 2026.

[18] Manon C Wigbers, Tzer Han Tan, Fridtjof Brauns, Jinghui Liu, S Zachary Swartz, Erwin Frey, and Nikta Fakhri. A hierarchy of protein patterns robustly decodes cell shape information. *Nature Physics*, 17(5):578–584, 2021.

[19] Raphael Wittkowski, Adriano Tiribocchi, Joakim Stenhammar, Rosalind J Allen, Davide Marenduzzo, and Michael E Cates. Scalar φ 4 field theory for active-particle phase separation. *Nature communications*, 5(1):4351, 2014.